R-10-52

Long-term alteration of bentonite in the presence of metallic iron

Sirpa Kumpulainen, Leena Kiviranta, B+Tech Oy
Torbjörn Carlsson, Arto Muurinen, VTT
Daniel Svensson, Svensk Kärnbränslehantering AB
Hiroshi Sasamoto, Mikatzu Yui, JAEA
Paul Wersin, Dominic Rosch, Gruner Ltd

May 2010

Svensk Kärnbränslehantering AB
Swedish Nuclear Fuel
and Waste Management Co

Box 250, SE-101 24 Stockholm
Phone +46 8 459 84 00

ISSN 1402-3091
SKB R-10-52

Long-term alteration of bentonite in the presence of metallic iron

Sirpa Kumpulainen, Leena Kiviranta, B+Tech Oy
Torbjörn Carlsson, Arto Muurinen, VTT
Daniel Svensson, Svensk Kärnbränslehantering AB
Hiroshi Sasamoto, Mikatzu Yui, JAEA
Paul Wersin, Dominic Rosch, Gruner Ltd

May 2010

Keywords: Iron-bentonite interaction, Iron corrosion, Copper corrosion.

Abstract

According to the KBS-3H concept, each copper canister containing spent nuclear fuel will be surrounded by a bentonite buffer and a perforated steel cylinder. Since steel is unstable in wet bentonite, it will corrode and the corrosion products will interact with the surrounding bentonite in ways that are not fully understood. Such interaction may seriously impair the bentonite's functioning as a buffer material, e.g. by lowering its CEC or decreasing its swelling capacity. This report presents results from two iron-bentonite experiments carried out under quite different conditions at VTT (Finland) and JAEA (Japan). Both studies focused on long-term iron-bentonite interactions under anaerobic conditions.

The study at VTT comprised eight years long experiments focused on diffusive based interactions between solid cast-iron and compacted MX-80 bentonite (dry density 1.5–1.6 g/cm^3) in contact with an aqueous 0.5 M NaCl solution. The study at JAEA comprised ten years long batch experiments, each involving a mixture of metallic iron powder (25 g), an industrially refined Na bentonite, Kunipia F, which contains more than 99% montmorillonite (25 g), and an aqueous solution (250 mL). Samples were sent to B+Tech in airtight steel vessels filled with N_2 and subsequently analyzed at various laboratories in Finland and Sweden. The JAEA samples differed with regard to the initial solution chemistry, which was either distilled water, 0.3 M NaCl, 0.6 M NaCl, 0.1 M $NaHCO_3$, or 0.05 M Na_2SO_4.

The analyses of the MX-80 bentonite samples were carried out on samples containing a cast iron cylinder and also on corresponding background samples with no cast iron. In addition, the external solution and gas phase in contact with the bentonite were analyzed. Briefly, the gas contained H_2, most possibly caused by corrosion of the cast iron, and CO_2, mainly as a result of carbonate dissolution. The eight years old external solution exhibited, inter alia, reducing conditions, a pH of around eight, and measurable amounts of Mg^{2+}, Ca^{2+}, and SO_4^{2-}. The bentonite was carefully divided into subsamples, which were studied with XRD, FTIR, SEM, ICP-AES, TEM-EDS, XANES, Mössbauer spectroscopy, and wet-chemical methods. Briefly, bentonite samples containing cast iron cylinders contained higher amounts of iron than the reference samples. The corroded iron was predominantly in the divalent form, and its concentration was highest close to the cylinder and decreased strongly with increasing distance from its surface. The average corrosion rate estimated from Fe profiles in the Fe-reacted samples is about 1.7 µm/a. The results from the Mössbauer spectroscopy analyses suggest that no reduction of the octahedral Fe^{3+} in the montmorillonite layers had occurred. The swelling pressure and the hydraulic conductivity were measured in undisturbed subsamples of the MX-80. The iron-bentonite interaction seemed to slightly decrease the swelling pressure, while the hydraulic conductivity was unchanged.

The corrosion rate of the Cu vessel surface was estimated from the Cu analysis in the clay to be about 0.035 µm/a.

The JAEA samples were analyzed with regard to the conditions in the water and in the bentonite. The water exhibited pH values in the approximate range of 11 to 13, and clearly reducing conditions with Eh values between –260 and –580 mV. XRD and FTIR analyses of the bentonite material, showed that montmorillonite was completely transformed to a non-swelling 7 Å clay mineral, most likely to the serpentine mineral berthierine, in samples containing 0.3–0.6 M NaCl solutions, with the highest pH values. The transformation was incomplete in samples containing 0.1 M $NaHCO_3$ solution, and did not occur at all when the solution was either 0.05 M Na_2SO_4 or distilled water.

Nyckelord: Iron-bentonite interaction, iron corrosion, copper corrosion.

Contents

List of abbreviations

CEC	Cation exchange capacity
EC	Electric conductivity
EDS	Energy dispersive spectrometry
EELS	Electron energy loss spectrometry
EG	Ethylene glycol
FAAS	Flame atomic absorption spectrometry
FTIR	Fourier transform infrared spectroscopy
GFAAS	Graphite furnace atomic absorption spectrometry
IC	Ion chromatography
ICP-AES	Inductively coupled plasma atomic emission spectrometry
ICP-MS	Inductively coupled plasma mass spectrometry
JAEA	Japan Atomic Energy Agency
PE	Polyethylene
PMMA	Polymerized methyl metaacrylate
SEM	Scanning electron microscopy
TEM	Transmission electron microscopy
XRD	X-ray diffraction
TXRF	Total reflection X-ray fluorescence spectrometry
XANES	X-ray absorption near edge structure

Foreword

This report is the outcome of a joint study between B+Tech and VTT on iron-bentonite interactions.

The report presents results from iron-bentonite interaction studies made on MX-80 samples prepared at VTT (Finland) and on Kunipia-F samples provided by JAEA (Japan) as a matter of practical collaboration under agreement between POSIVA and JAEA.

The achievements in this study would not have been possible without the participation of the following persons (listed in alphabetical order):

T. Carlsson[1], L. Kiviranta[2], S. Kumpulainen[2], A. Muurinen[1], H. Sasamoto[3], M. Snellman[4], D. Svensson[5], P. Wersin and D. Rosch[6], and M. Yui[3].

The following personnel participated, assisted or advised in the analytical work:

Kirsti Helosuo, Markku Honkala, and Eeva-Liisa Kotilahti, VTT

Jari Martikainen, B+Tech Oy

Jussi Ikonen and Marja Siitari-Kauppi, HYRL

Mia Tiljander, Marja Lehtonen, and Bo Johansson, GTK

Ulf Nilsson and Torbjörn Sanden, Clay Technology Ab

Yanling Ge, TKK

Johan Lindén, Åbo Akademi

Eliisa Hatanpää and Minna Rantanen, Ramboll Analytics Oy.

Heini Laine and Päivikki Mäntylä (Saanio & Riekkola Oy) are gratefully acknowledged for the technical support in the final editing of the report.

[1] VTT, Espoo, Finland

[2] B+Tech Oy, Helsinki, Finland

[3] JAEA, Ibaraki, Japan

[4] Saanio & Riekkola Oy, Helsinki, Finland

[5] SKB, Figeholm, Sweden

[6] Gruner Ltd., Basel, Switzerland

1 Introduction

1.1 Background

An alternative design KBS-3H to the reference design KBS-3V has been developed in joint SKB/ Posiva studies. In KBS-3H canisters are emplaced horizontally along a deposition drift. Within the KBS-3H design, each canister, with a surrounding partly saturated layer of bentonite clay, is placed in a perforated steel cylinder prior to emplacement and the entire assembly is called the supercontainer (SKB 2001, Anttila et al. 2008).

The iron steel shell of the supercontainer is expected to corrode in the repository conditions (Smart et al. 2001). Interactions with dissolved Fe, hydrogen gas and other reaction products may lead to the alteration or destruction of bentonite minerals and change the thermo-hydro-mechanical and chemical (THMC) behaviour of the buffer and thus may impair the desired safety functions of the buffer bentonite. Possible mineralogical changes and their effects include:

- Development of Fe-rich, non-swelling clay minerals decreasing the swelling pressure and increasing the hydraulic conductivity of the buffer.
- Incorporation of Fe into the smectite structure, i.e. transformation into Fe-rich dioctahedral or trioctahedral smectites decreasing the chemical stability of the smectite.
- Reduction of octahedral Fe(III) in the smectite lattice increasing the layer charge and cation exchange capacity. Increasing layer stacking may cause decrease in surface area and swelling pressure (Lear and Stucki 1989, Stucki 1997).
- Replacement of Na by Fe in the cation exchange sites in the interlayer positions (Kamei et al. 1999) or specific adsorption of Fe to the octahedral edges may reduce the sorption sites for radionuclides. In contrast, precipitation of distinct Fe oxide minerals promotes adsorption or coprecipitation of radionuclides.
- Formation of secondary minerals as a result of Fe(II) release and precipitation, or due to release of silica as a consequence of transformation of clay minerals, which may affect the porosity and microstructure of the bentonite. Cement formation in the pore structures or in the smectite interlayers causes increase in hydraulic conductivity and decrease in plasticity.
- Formation of corrosion products, including hydrogen gas may alter physical properties of the buffer. Typical corrosion products include metastable transient phases $Fe(OH)_2$ and green rusts, as well as, magnetite (Fe_3O_4), a typical end product of Fe corrosion. If corrosion rate exceeds the diffusive transport rate of hydrogen gas, microfractures, i.e. preferential transport pathways, may form inside the buffer. Fe profiles in bentonite have been used to estimate the corrosion rates (Xia et al. 2005).

Furthermore, diffused Fe(II) may react with accessory iron oxides in the buffer, transforming them into magnetite, which has a larger crystal size and lower solubility than the initial iron oxide (Otake et al. 2007).

1.2 Previous studies

Previously, Fe-bentonite interactions have been evaluated using natural analogues in soil formations (Marcos 2003, 2004), and by conducting an anaerobic corrosion study with Fe coupons, wires and bentonite at elevated (30–50°C) temperatures (Carlson L et al. 2006, 2007). In the latter study, an increase in iron content of the bentonite, decreasing with the distance from source was found. On the surfaces of a Fe coupon, magnetite, hematite and goethite were identified. In the bentonite however, neoformed Fe clay minerals (e.g. Fe-rich smectite, berthierine) or secondary Fe oxides or hydroxides (e.g. magnetite) could not be identified. Decrease in cation exchange capacity and increase in hydraulic conductivity in low density samples was observed. Unfortunately, during this study, some experimental difficulties were encountered. Furthermore, composition of porewater and gas was not examined.

Wersin and Snellman (2007) summarized the status of R&D on the impacts of Fe to the performance of the barrier clay in waste disposal system based on the response to an enquiry on iron-clay studies at different organisations. Identified needs for further studies include e.g.; nature of corrosion products, uncertainty in thermodynamic and rate constants for clay minerals, identification of minor reaction products, effects of cementation especially in anaerobic conditions, effects of Fe on CEC, swelling pressure and hydraulic conductivity in general, and modelling.

Wersin et al. (2007) assessed the extent of Fe-bentonite interactions by means of simple mass balance calculations and reactive transport modelling. The mass balance calculations indicated that at maximum 10–30% of the montmorillonite may convert to the non-swelling Fe(II) rich clays. The more realistic reactive transport modelling indicated that the transformation should stay spatially limited. Wersin et al. (2007) recommended that further Fe-bentonite interaction studies should include measurements of physical properties (swelling pressure and hydraulic conductivity) in anoxic conditions, diffusion experiments with Fe(II), and potential effects of H_2 gas.

1.3 Objectives

The objective of this work was to give scientific support for KBS-3H that deals with the the performance of bentonite buffer in contact with the supercontainer shell material. The focus is on studies of long-term (8–10 y) mineralogical, chemical and physical changes in bentonite due to Fe-bentonite interactions at ambient temperature and nitrogen atmosphere. Two sets of samples were available for the work: 8 y old compacted Fe-bentonite diffusive based interaction samples from VTT and 10 y old batch Fe-bentonite interaction samples from JAEA.

2 Experimental

2.1 8 y old compacted Fe-bentonite interaction samples from VTT

In late 2000, VTT initiated a study on the interaction between cast iron and saturated MX-80 under anoxic conditions. For this purpose, a series of five small MX-80/cast iron samples were prepared and stored at ambient temperature (+25°C) in 0.5 M NaCl solutions inside PE-vessels, see Figure 2-1. No attempt was made to sterilize the porewater. The initial volume of the external solution was 100 mL. A sixth MX-80/cast iron sample was also prepared and stored in distilled water. In addition, six reference samples were made, which contained MX-80 but no cast iron. The dimensions of the samples are shown in Figure 2-2. The surface area of the cast iron cylinders were 14.1 cm^2. All twelve PE-vessels were initially stored in desiccators in a glovebox under N_2, but later the desiccators were replaced by smaller protective steel containers, which also were kept in a N_2-filled glovebox, see Figure 2-3. Initial calculated dry density of studied Fe-bentonite and reference samples were 1.69 g/cm^3 and 1.51 g/cm^3, respectively.

One pair of samples (i.e. one MX-80/cast iron sample plus its reference sample, which contained MX-80 but no cast iron) was opened and analysed nine months after starting the experiment (Aalto et al. 2002). This report presents results from analyses of two sample pairs which were opened 8.2 and 8.6 years from the start. These samples are in the following referred to as the 1st and 2nd sample pair, respectively, or, more generally, as the "8 y samples".

Interactions of bentonite with cast iron were a prime target of this study, but interactions with other materials present (e.g., the Cu vessel and the steel sinter) were also taken into account in profile sampling and analyses.

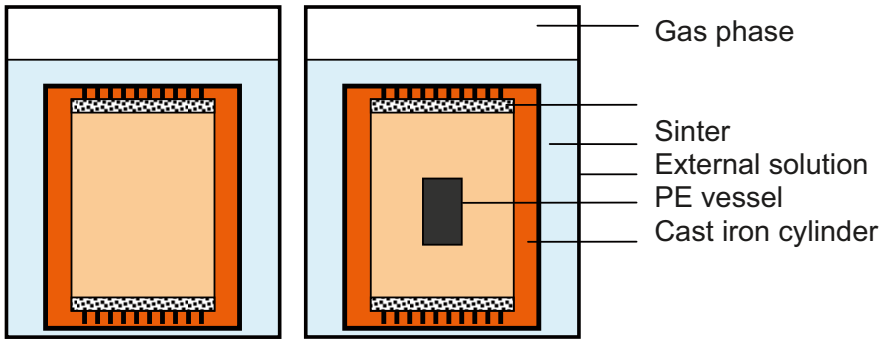

Figure 2-1. *MX-80 reference sample (left) and MX-80/cast iron sample (right) placed in a copper vessel kept in an external solution.*

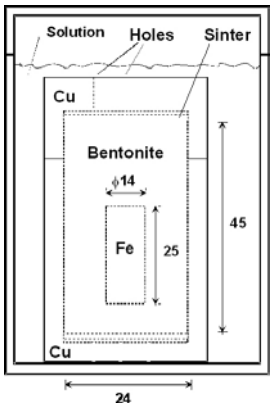

Figure 2-2. *Dimensions (in mm) of the Cu vessel, the MX-80 bentonite, and the cast iron cylinder (from Kumpulainen and Muurinen 2001).*

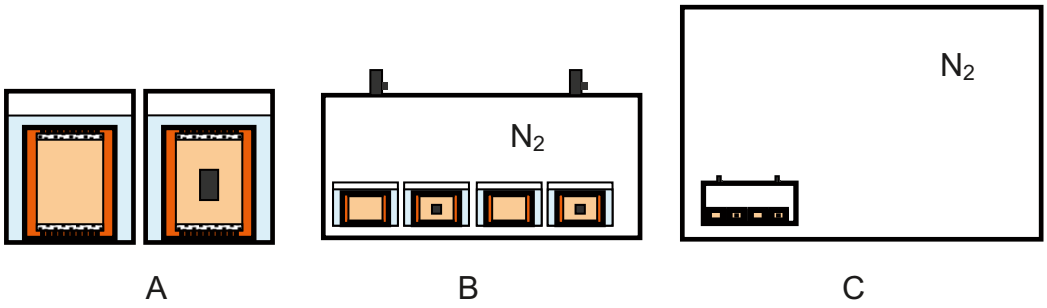

Figure 2-3. *Schematic description of the anaerobic (N_2) storage of samples in VTT's long-term MX-80/cast iron interaction experiment. A) Two PE-vessels containing an external solution and a Cu-vessel filled with either MX-80 (left) or MX-80 containing a cast iron cylinder (right). The MX-80 stays in contact with the external solution via sinters. B) Steel vessel containing several PE-vessels with MX-80/cast iron samples and their corresponding reference samples. C) Glovebox for long-term storage of the steel vessels. Not to scale.*

2.2 10 y old batch Fe-bentonite interaction samples from JAEA

Japan Atomic Energy Agency (JAEA) started a Fe-bentonite interaction batch experiment with industrially refined Kunipia F bentonite and iron powder 10 years ago. The samples have been kept in a glovebox under a nitrogen atmosphere (O_2 < 0.1 ppm) since the start of experiment. The experimental setting included 25 g of Kunipia F bentonite, 25 g of iron powder, and 250 mL of various solutions (distilled water (No 61), synthetic water with 0.3 M NaCl (No 62), 0.6 M NaCl (No 63), 0.1 M $NaHCO_3$ (No 65), or 0.05 M Na_2SO_4 (No 68)) that were mixed, shaken, and left to stay for 10 y in a PE bottle at room temperature. The bentonite consisted of 98–99% of smectite with minor (<1%) quartz and calcite. The iron powder used in the experiment had a purity of 99.9%, and a specific surface area of 0.33 m^2/g.

It was agreed that half the samples were to be analyzed by JAEA and the other half would be available for Posiva/SKB for analyses. For the transport, gas-tight steel autoclaves equipped with a Teflon insert were sent to Japan. Sample dismantling, packing and transfer back to Finland was taken care of by JAEA. Samples No 62, 63, 65 and 68 were delivered as slurries or pastes, but the sample 61 (in distilled water) was opened and partly analyzed earlier by JAEA, and therefore delivered as dry powder, where most of the metallic iron had already been removed. In addition, reference samples containing initial Kunipia F bentonite were delivered from Japan to Finland for comparison.

From JAEA's samples, in this analysis and reporting phase 1, results from mineralogical analyses using XRD and solution pH, Eh are presented. In addition, VTT has started analyses of chemical composition of solutions, but the results are not yet available.

A comparison between experimental set-ups for VTT's and JAEA's samples is shown in Table 2-1.

Table 2-1. Comparison of experimental set-up for VTT and JAEA long-term Fe-bentonite experiments.

	8 y old VTT's samples	10 y old JAEA's samples
Bentonite composition	Bulk MX-80	Purified (clay fraction) Kunipia-F
Clay to solution ratio	Compacted, 30 g solids with 100 mL of external water	Batches, 25 g solids with 250 mL of solution
Reactive surface area of iron to clay	One cast iron cylinder (surface area 14 cm^2)	Fine iron powder, 25 g (surface area 82,500 cm^2)
Initial solution composition	0.5 M NaCl -solution	Distilled water or synthetic water with 0.3 M NaCl, 0.6 M NaCl, 0.1 M $NaHCO_3$, or 0.05 M Na_2SO_4

3 Materials and methods

3.1 Gas sampling and analyses

Gas analyses were only performed on VTT's samples. Prior to opening the test cells, gas samples were taken from:

1) the space in the larger steel vessel (Figure 2-3B),

2) the space above the external solution in a reference sample (Figure 2-1),

3) the space above the external solution in the MX-80/cast iron sample (Figure 2-1).

The gas sampling from the large steel vessel was carried out in a straightforward manner by attaching a vacuum-pumped transport vessel (Figure 3-1) to the outlet valve on the steel vessel. The loss of gas in the latter was compensated for by adding N_2 flushed Milli-Q water via a second valve on the steel vessel.

The gas sampling from the PE-vessels (Figure 2-1) was made in a slightly different way. Briefly, a gas sample from each PE-vessel was taken by two syringes (one for gas sampling and one for replacing the volume of the sampled gas with an equivalent volume of water) that had been glued with Araldite on top of the PE-vessel. This was immediately sealed with Araldite once the syringes were removed.

The gas samples were subsequently transferred to three steel containers (Figure 3-1), transported to an analytical laboratory (Ramboll Oy), and analysed by gas chromatography (Hewlett-Packard HP6890) using a thermal conductivity detector (TCD). The bulk gas component (N_2) was analyzed with regards to its contents of O_2, CO_2, and H_2.

3.2 Solution chemistry

3.2.1 VTT's samples

External solution

The external solution chemistry was analysed in two 8 y sample pairs. The first one was opened and analysed after 8.2 years from the outset of the experiment, the second one after 8.6 years.

The first sample pair, which consisted of the reference sample 9 and the iron/bentonite sample 10, was handled straightforwardly; the PE-vessels were taken from the large storage steel vessel (Figure 2-3B) and opened (on 3.2.2009), the Cu-vessels were removed from the solutions, and the PE-vessels were

Figure 3-1. *Vessel used for transport of gas samples from VTT. With courtesy of Ramboll Oy.*

quickly re-closed and used for continued storage of the external solution. The Cu-vessels were thereafter opened and the solid bentonite samples were handled as described in Section 3.3. The external solution was subsequently analysed nine days later with regard to Eh and pH.

The pH measurements were performed by an Orion Ross combination electrode no. 81635C in open vessels with about 5 mL aliquots of external solution. The Eh measurements were made by Au- and Pt- electrodes against an LF-2 electrode as described elsewhere (e.g. Muurinen and Carlsson 2008). However, the redox-measurements in the first sample-pair indicated that the solution became oxidized during the nine-day storage in the glovebox and that, consequently, no relevant Eh-data could be obtained in this case. (The measured Eh values were in the range 260–470 mV.)

The second sample pair, which consisted of the reference sample 12 and the iron/bentonite sample 15, was taken from the storage steel vessel about four months after the first one. In order to minimize the risk of oxidising the external solution, the necessary amounts of solution (about 20 mL) were taken through the wall of each PE-vessel by using a syringe equipped with the electrodes described above, see Figure 3-2.

The Eh-measurements started inside the syringe directly after sampling. Care was taken to assure that no gas phase was present in the syringe, since that might have disturbed the distribution of, e.g., trace concentrations of oxygen between gas and liquid and thus impaired the quality of the Eh-measurements.

The pH measurements in the second sample pair were made by using a syringe for transferring external solution from the unopened PE-vessel into a closed bottle to which the above Orion Ross pH electrode was fixed. The connection between bottle and pH meter was sealed with strong tape. The syringe was used to fill the bottle completely, and thereafter started the pH measurements.

The alkalinity (Alk) was, just like pH and Eh, determined under N_2 atmosphere by acid titration. In case of the Fe^{2+}/Fe^{3+} analyses, only the sample preparation was made under N_2 atmosphere, while the analytical work was made outside the glovebox in normal air.

The external solution analyses also involved the use of the following techniques and elemental analyses (bold):

IC: **Cl**, **SO_4**, ICP: **Fe**, **Mg**, **Na**, **Ca** FAAS: **K**.

Porewater pH and Eh

The porewater pH and Eh in the reference sample 12 and the iron/bentonite sample 15 was studied by cutting a disc (height: 11–12 mm, diameter: 20 mm) from each sample and placing it in a squeezing cell equipped with measuring electrodes. All operations and measurements were performed under N_2. The measuring electrodes used were Pt- and Au-electrodes for redox-measurements and IrOx-electrodes for pH. The measurements were performed against an LF-2 reference electrode, which is a commercially available Ag/AgCl electrode. All results from redox-measurements in this study are expressed as Eh-values, meaning that the measured potentials refer to the SHE-scale.

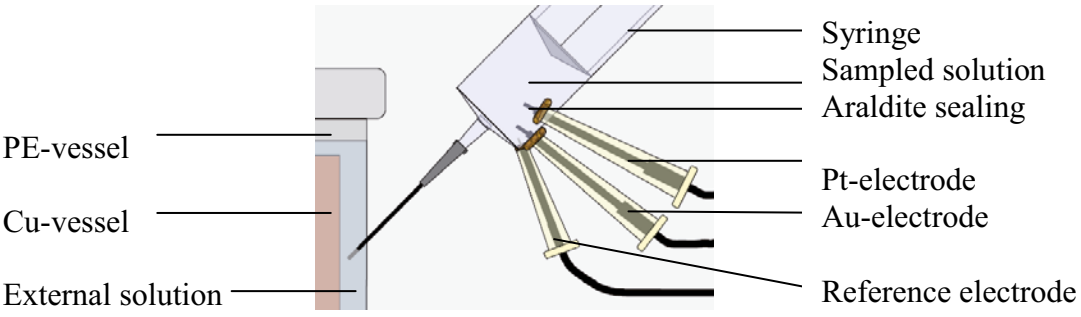

Figure 3-2. *Arrangement for making redox-measurements in external solutions. The syringe contained a small magnetic bar (not seen in the picture) for stirring.*

Details about the squeezing cell and the electrodes are found in Muurinen and Carlsson (2008). In case of the pH measurements, however, technical problems occurred and no data were collected.

3.2.2 JAEA's samples

The plans for the JAEA samples 62, 63, 65 and 68 involved analyses of the water phase by VTT. The samples were therefore brought (in sealed, N_2-filled transport vessels) from JAEA to VTT and opened in a glovebox under N_2. The water phase was then separated from the solid material in samples 62 and 63 by centrifugation. In case of the denser samples 65 and 68 it was necessary to use squeezing cells and approximately a week of hydraulic squeezing in order to achieve a few millilitres of squeezed solution.

The study of the water phase included potentiometric measurements of pH and Eh and the following elemental analyses:

IC: **Cl**, **SO_4,** ICP: **Fe**, **Si**, **Al**, **Mg**, **Na**, **Ca**, FAAS: **K**.

The high salinity of the solutions represented a minor problem; the concentrated solutions required dilution prior to the analyses, which raised the detection limits.

3.3 Dismantling of VTT's sample cells

Dismantling and sampling of 1st and 2nd sample cells were done on 3.2.2009 and on 1.7.2009, respectively, in an MB150B-G glovebox with N_2 atmosphere. The box had a small overpressure (~4 mbar), an O_2 content < 1 ppm and a H_2O content < 0.1 ppm. The locations of the subsamples and the planned analyses are shown in Figure 3-3.

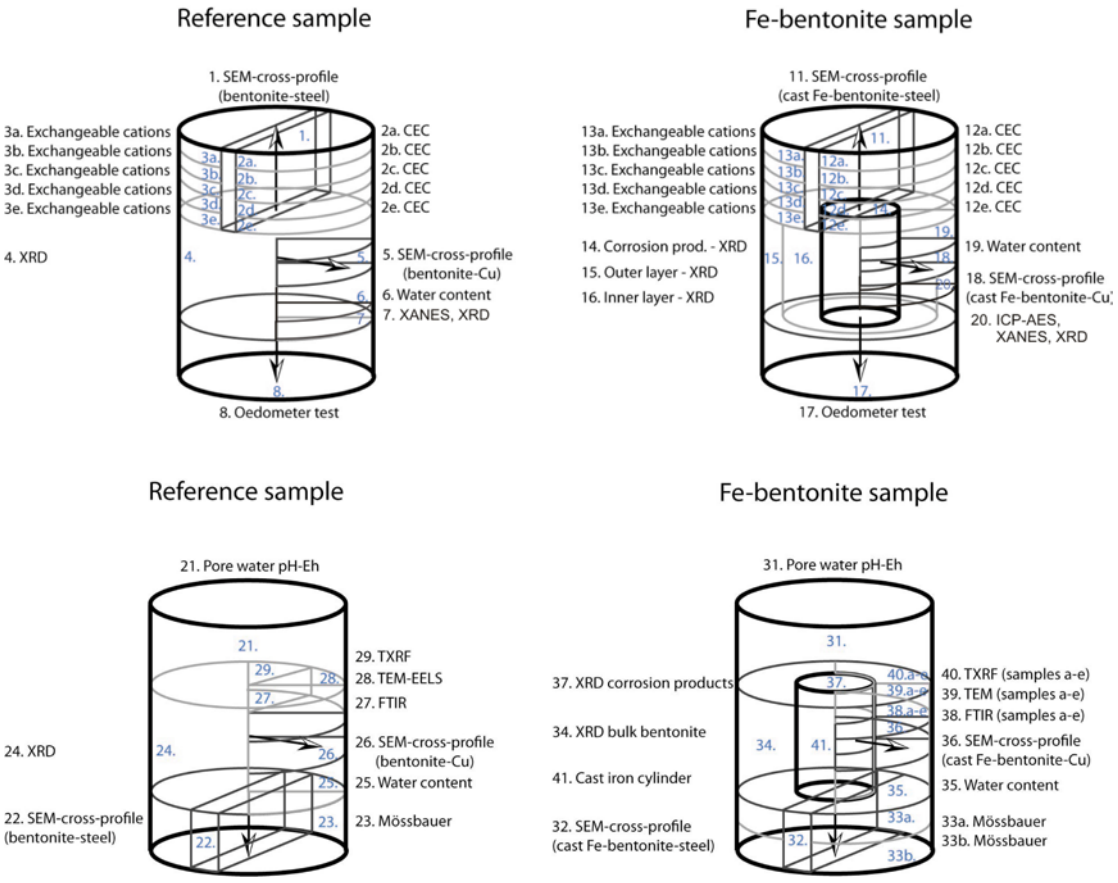

Figure 3-3. *Subsamples taken from the first and second pair of 8 y samples. Arrows indicate sampling of undisturbed profiles.*

Samples were pushed out from the Cu-vessel using a piston and cut to variable size and form by using a blade, a scraper or a scalpel. Corrosion products were scraped from the surface of the cast iron. Samples were taken from the 1st sample pair to determine CEC, exchangeable cations, chemical composition (SEM-EDS, ICP-AES), mineralogy (XRD (bulk and clay fractions), XANES), water content, swelling pressure and hydraulic conductivity. Samples were taken from the 2nd sample pair to determine porewater pH and Eh, chemical composition (SEM-EDS, TEM-EDS, TXRF), mineralogy (XRD (bulk and clay fractions), FTIR), water content, and the valence of iron (Mössbauer spectroscopy, TEM-EELS).

1st Sample pair = Reference sample 9 and Fe-bentonite sample 10.

2nd Sample pair = Reference sample 12 and Fe-bentonite sample 15.

The outer surfaces of the Cu-vessels were clear and shiny (Figure 3-4a), not showing any indication of oxidation. The inner surfaces of Cu vessels were also almost as clear and shiny.

The reference sample was easy to remove from the Cu-vessel and to cut into slices (Figure 3-4b). The removal of Fe-bentonite sample from Cu-vessel required more force, was harder to cut, and developed cracking features during cutting. Reacted bentonite was also stuck to the cast Fe, and therefore undisturbed sample profile slices taken for SEM were loosened from the zone of corrosion products, and not directly from the surface of cast Fe.

In the top part, a brownish diffusion front deriving from cast Fe extending to approximately 7 mm distance from the cast Fe was observed (Figure 3-4c). Corrosion products on the surface of cast Fe were greenish and greyish in colour (Figure 3-4d).

All solid and solution sample preparations, and analysis of solution pH, Eh and alkalinity, were made inside the glovebox (for more details, see method descriptions in sections 3.2–3.7).

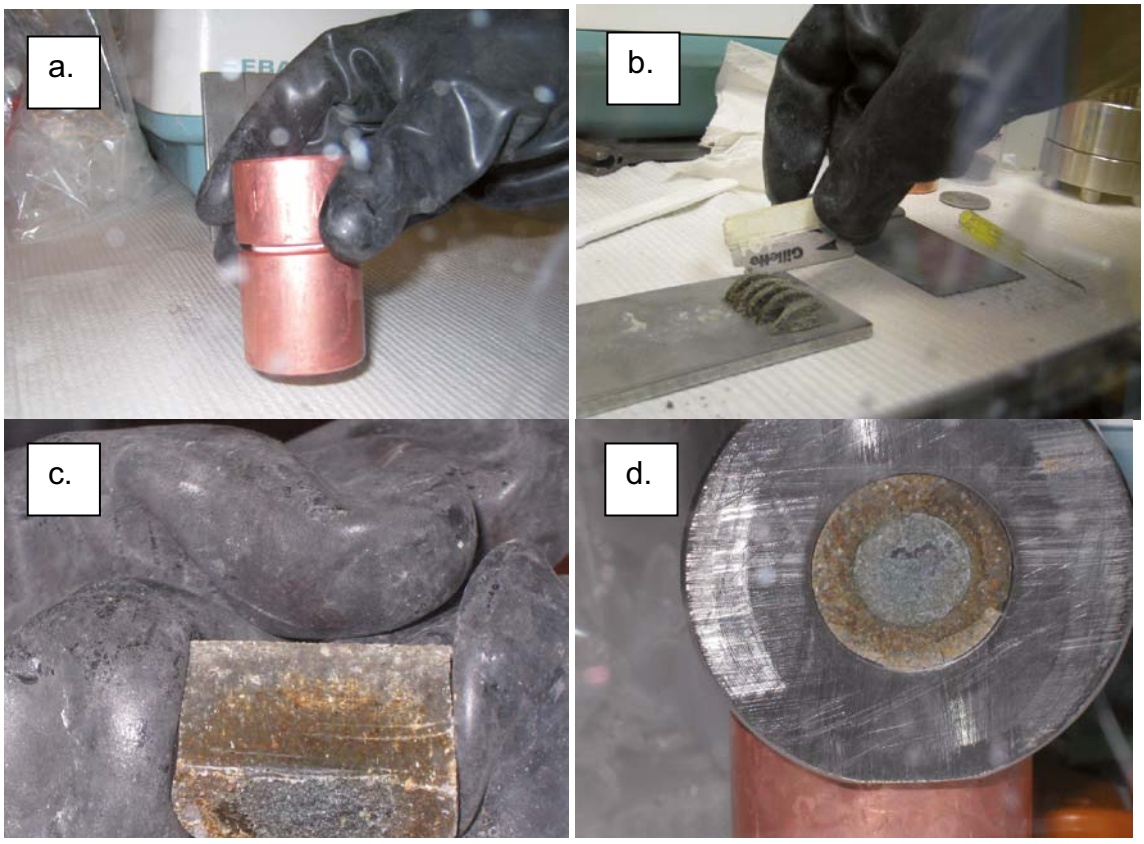

Figure 3-4. *Photos from the dismantling and sampling from VTT's sample cells.*

3.4 Opening of the JAEA samples

Samples 62 and 63 were liquid-like slurries while samples 65 and 68 were thick pastes. The colour of samples was dark-bluish green, grey and black (Figure 3-5).

3.5 Cation exchange capacity

3.5.1 VTT's samples

Five subsamples (slices) were taken from the MX-80/cast iron sample and from the corresponding reference sample as indicated in Figure 3-3. The CEC-analyses were performed in laboratory atmosphere although it is recognised that some oxidation of iron may take place. The CEC of each slice was then determined by the Cu(II)-triethylenetetramine method (Meier and Kahr 1999).

3.5.2 JAEA's samples

The JAEA samples, presented in detail in Appendix 1, contained equal amounts of iron and bentonite. The presence of iron made the CEC-determination slightly more complex and might disturb the results and make their interpretation difficult. For this reason, it was decided that the CEC-analysis described above should include also three subsamples. Briefly, two of these were made by separating each original JAEA sample (62, 63, 65, or 68) into a light fraction and a heavy fraction by centrifugation. The third subsample was produced by purifying the light fraction from iron impurities as described by Tributh and Lagaly (1986).

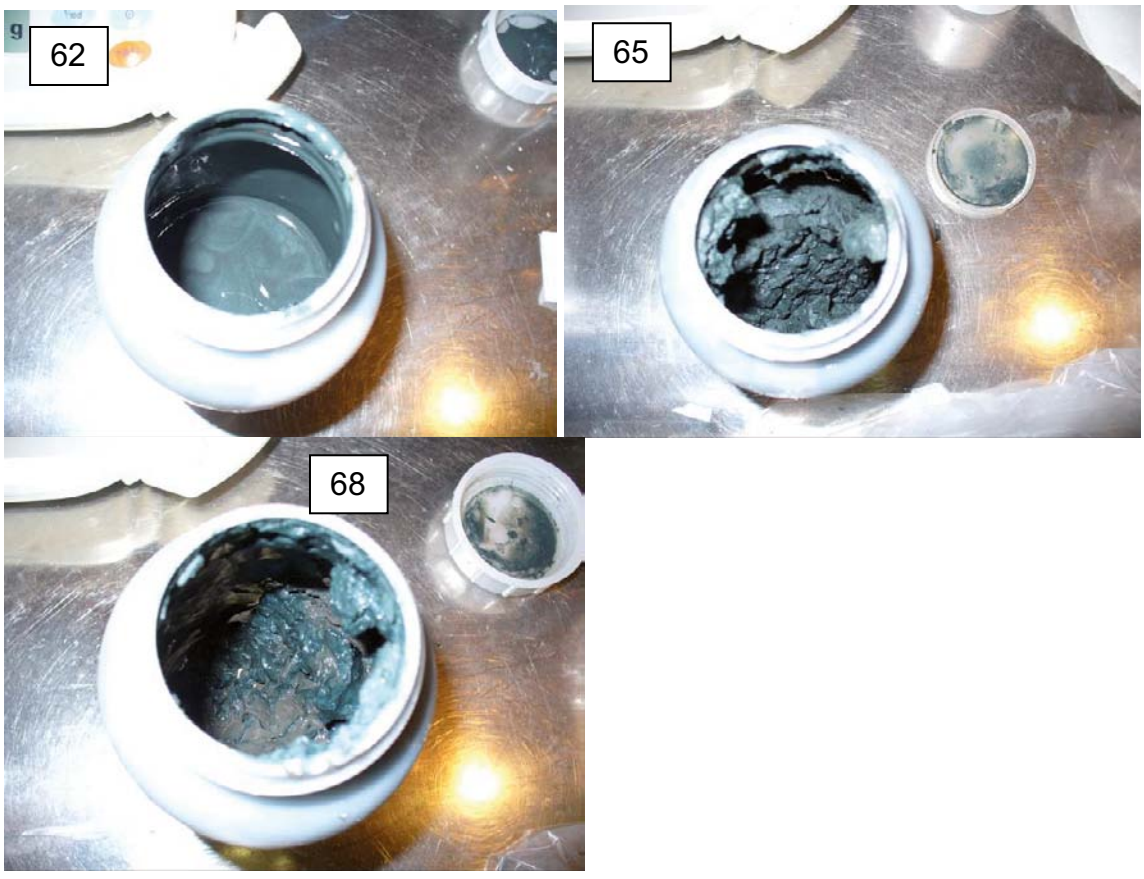

Figure 3-5. *Samples 62 (0.3 M NaCl), 65 (0.1 M $NaHCO_3$) and 68 (0.05 M Na_2SO_4) after opening. Photos were taken by JAEA.*

3.6 Mineralogy

3.6.1 XRD

XRD studies were done both at the Geological Survey of Finland and at MAX-lab in Lund, Sweden. Preparation of XRD-mounts was done in N_2-atmosphere in a glovebox. Samples from the 8y old Fe-bentonite experiment of VTT (samples 4, 14, 15, 16, 24, 34 and 37, Figure 3-3) were used as they were, but moist JAEA's samples were washed once with ethanol (purity grade 99.9%) to extract remaining porewater solution before XRD analyses. Washing with analytical grade ethanol is reported to slow down oxidation of green rust, a possible corrosion product of iron powder (Lewis 1997).

To analyse the mineralogical composition of bulk fraction, small amounts of material were dried in a glovebox and ground in agate mortar with a pestle to the particle size of < 10 μm. Ground material was placed on an amorphous silicon plate, a drop of acetone was added and the slurry spread. Dry sample mounts were kept in N_2-atmosphere until analysis. Bulk fractions were analysed using a rotating sample holder, Philips X'Pert MPD diffractometer, which was equipped with Cu anode tube and monochromator, using wavelength of $K\alpha_1 = 1.54060$, $K\alpha_2 = 1.54443$, and $K\beta = 1.39225$, voltage of 40 kV and current of 55 mA, from 2 to 70° 2θ with 0.02° counting steps and 1 s/step counting time at the Geological Survey of Finland.

Most of the Fe-powder that was present in moist JAEA samples (samples 62, 63, 65 and 68) was separated by dispersing the ethanol washed sample into deionized water and centrifugation repeatedly before separation of clay fraction.

For determination of clay minerals present, the clay fraction was separated with dispersing sample material into deionized water, adding 1 M NaCl, centrifuging, discarding the extract, and repeating addition of NaCl solution twice. Thereafter, slurry was washed three times with deionized water, and coarse fraction (> 2 μm) separated from clay fraction (< 2 μm) with centrifugation (approximately 10 s at 6,000 rpm). Na-exchanged clay suspension was converted to Mg-exchanged clay by adding 0.5 M $MgCl_2$-solution three times, and thereafter washing the clay sediment with deionized water three times. Some of the JAEA's samples (especially sample 63) resisted dispersion even after multiple NaCl exchanges and washing cycles, and therefore, separation of the clay fraction and mounting were not entirely successful.

Preparation of oriented clay film was done with smearing a thick clay paste on a silicon plate. Oriented mounts were analysed at 2–35° 2θ.

After analysis of N_2-air-dried mounts, a drop of ethylene glycol was added and the mounts were analysed at 2–22° 2θ to observe the presence of swelling minerals i.e. smectites.

X-ray powder diffraction data for samples 7 and 20 (Figure 3-3) was collected at the beam-line I911 at MAX-lab, Lund (Mammen et al. 2002, 2004), using a Mar system with a flat CCD detector (Mar 165, 2,048 x 2,048 pixels). The x-ray beam had a wavelength of 0.9084 Å and a size of 1 x 1 mm. The capillary was stationary during the measurements and kept in a stream of flowing nitrogen with adjustable temperature (Cryojet, Oxford Instruments). The integrated intensity, scattering angle and width of the recorded diffraction rings were evaluated using the software Fit2d (A. P. Hammersley, The European Synchrotron Radiation Facility). Calibration of the sample-detector distance was done using LaB_6 and/or silicon powder. The Mg-exchange was done by 3 x washing with 0.5 M $MgCl_2$, followed by 3 x washing with deionised water.

3.6.2 FTIR

Samples for FTIR (Figure 3-3) were dried inside the N_2-glovebox and kept in N_2-air until analysis. The clay fraction was used for analysis of JAEA's samples, but due to scarcity of material bulk bentonite was used for analysis of VTT's samples.

Approximately 2 mg of sample was ground together with 200 mg of KBr powder in a agate mortar with a pestle and pressed to a 13 mm diameter discs. KBr discs were dried at 150°C for 20 h to remove adsorbed water. Infrared spectrum was recorded using a transmission mode in a range from 4,000 to 200 cm^{-1} with Perkin Elmer Spectrum One FTIR spectrometer at the Department of Geology, University of Helsinki before and after drying in 150°C. Resolution of scans was 4 cm^{-1}.

3.6.3 Mössbauer spectroscopy

The subsamples (23, 33a and 37, Figure 3-3) were dried in N_2-atmosphere inside a glovebox and ground to a fine powder in agate mortar with a pestle. 50 mg of sample powder was mixed with epoxy glue in an Al-cup. The mixture was spread evenly on the bottom of Al-cup (area of ~3 cm^2), air bubbles (if present) were pierced with a needle and the samples were allowed to dry in a glovebox. Sample mounts were subsequently transported in a N_2-filled transport vessel to Åbo Akademi and stored in N_2-atmosphere inside a glovebox prior to measurements. The analyses were carried out by Johan Lindén, Åbo Akademi.

The three bentonite samples were measured by ^{57}Fe Mössbauer spectroscopy. Each sample was measured at 77 K in transmission mode using a sinusoidal velocity scale with a maximum Doppler velocity of 10.2 mm/s. The velocity was chosen to allow detection of the magnetic lines of Fe oxides and hydroxides. For paramagnetic samples this scale is a bit too large. But with no prior knowledge it was better to use a higher velocity scale. The geometry, i.e. source-to-detector distance, absorber area and collimation was the same for all samples, as well as the settings for the gamma-ray window. Data was collected for at least seven days for each sample, yielding a folded background level of ~$17 \cdot 10^6$ counts.

Sample cooling was achieved using an Oxford ITC-4 continuous-flow cryostat operated with liquid nitrogen. The 4.4-keV Mössbauer quanta were detected using a LND 4546 proportional counter with a beryllium window. A Fast ComTec MA-250 velocity transducer was used for moving the source. It was equipped with a Halder MR-351 drive unit. The data was gathered using a Fast ComTec MCA-3 multichannel-analyzer PCI card in an ordinary PC. The measurements were done in a multiscaling mode. The spectra were fitted using a home-made nonlinear least-squares fit program, utilizing spectral components corresponding to three paramagnetic doublets and one magnetic sextet. For the paramagnetic components, fit parameters were quadrupole splitting (Δ in mm/s), isomer shift (δ with respect to α-Fe in mm/s) and spectral intensities (I in %). For the magnetic component, the internal field (B in T) and its gaussian distribution (ΔB in T) were included as fit parameters as well. All components were constrained to have a common line width (Γ in mm/s).

3.6.4 XANES

The reference sample 7 and sample 20 (Figure 3-3) were mounted as wet pastes between sulfur free XRF tape in inert atmosphere in a glovebox. Bulk MX-80, Fe_2O_3, Fe_3O_4 and $FeCO_3$ were used as additional reference materials. The bulk MX-80 was mounted as a dry powder between two XRF tapes, while the other references were mounted on the surface of one XRF tape. The thickness of the sample holder was 1 mm. X-ray absorption data was recorded at beam line I811 at MAX-lab, Lund (Carlson S et al. 2006). Several consecutive scans were recorded in the range –100 to +500 eV using the Lytle detector (fluorescence mode). The Athena software was used for processing and evaluation of the data. Energy calibration was done using a metallic iron foil.

3.7 Chemical composition of bentonite

3.7.1 SEM-EDS

Slices from Fe-bentonite and reference samples for SEM from top and middle sections (Figure 3-3) were put into air-tight steel vessels inside a glovebox, and transported to the University of Helsinki, Department of Radiochemistry. Samples were moulded with acryl resin, freeze dried, and impregnated by methyl metaacrylate degassed resin, which was polymerized with radiation according to the method of Hellmuth et al. (1993, 1994). PMMA-mounted bentonite samples were cut open with a diamond blade.

Analysis of semiquantitative chemical composition of bentonite from the distance profiles was done at the Geological Survey of Finland using SEM-EDS. Before analysis, sample mounts were covered with carbon. Areas for analyses were selected from distance profiles to represent the bentonite matrix which does not contain visible large grains of accessory minerals. The results were reported as oxides, which were normalized to 100%.

3.7.2 Exchangeable cation extractions

Slices from Fe-bentonite and reference samples from five variable distances on the top part (Figure 3-3, Figure 3-4b) were dried in N_2-atmosphere, ground in an agate mortar, and 350 mg of dried bentonite weighted in centrifuge tubes. The remaining powder was collected for determination of water content. 0.5 M NH_4Cl-solution in 80% ethanol (with purity grade of 99.9%) was prepared by mixing deaerated ethanol and deionized water. 6 mL of NH_4Cl-solution was added to the centrifuge tubes, shaken for 30 min, and centrifuged at 6,000 rpm for 10 min. The extract was collected, and thereafter NH_4Cl-solution was added. The extraction procedure was repeated twice. The collected extracts were filtered through 0.45 µm pore size filter and taken out from the glovebox. The ethanol in solution was evaporated, and deionised water added to reach a volume of 25 mL. Suprapur HNO_3 was added to dissolve possible precipitates before analysis of Ca, Fe, Na, Mg and K with ICP-AES. Before adding the HNO_3, part of the extracts from Fe-bentonite sample showed a light yellow colour.

3.7.3 ICP-AES

The chemical composition of bentonite was determined from three variable distances between cast Fe and Cu-vessel from two different samples (samples 19 and 20 in Figure 3-3). The chemical composition of reference sample 6 (Figure 3-3) was determined in a similar way from three variable distances from the Cu-vessel. The samples were split into subsamples (a–c) according to Figure 3-6. In addition, chemical composition of sample 29b was determined. Sample 29b contained approximately 2 mm of material from the outer edge of sample 29 (Figure 3-3). The samples (0.2 g each) were digested using lithium metaborate fusion and nitric acid dissolution. Concentrations of dissolved elements were determined using ICP-AES.

3.7.4 TEM-EDS

Sample 39a (closest to the cast Fe, Figure 3-3) was studied with transmission electron microscopy (TEM). A small amount of the sample was dispersed in ethanol using ultrasonic bath for 2 minutes (40 kHz, 100 W). A drop of the prepared solution was placed on a Holey Carbon film on a 400 mesh Cu (25) grid (Agar Scientific). The sample was allowed to dry in air (~30 minutes). The sample was subsequently treated with plasma cleaner for 5 seconds (Model 1020 Plasma cleaner, Fischione instruments) in order to remove dust and loose particles, which were not attached properly to the carbon film.

The prepared sample was studied with a Tecnai F20 transmission electron microscope at the Department of Material Sciences, Helsinki University of Technology. Ten different particles/aggregates in the sample 39a were photographed. For some of them, electron diffraction patterns were recorded and the corresponding d-values were calculated using the equation $d=\lambda*L/R$, where λ is the wavelength, L is the calibrated camera length, and R is the distance of diffraction pattern (rings) from the origin (mm). The calculations were made using a value of 0.00251 nm for λ, while L, the calibrated camera length, was specific for each diffraction pattern (the nominal camera length was 200 mm). In addition a TEM-EDS-linescan was performed on 10 particles in the sample. On each linescan, 50 points on a length of 200–600 nm was analysed for 1 s.

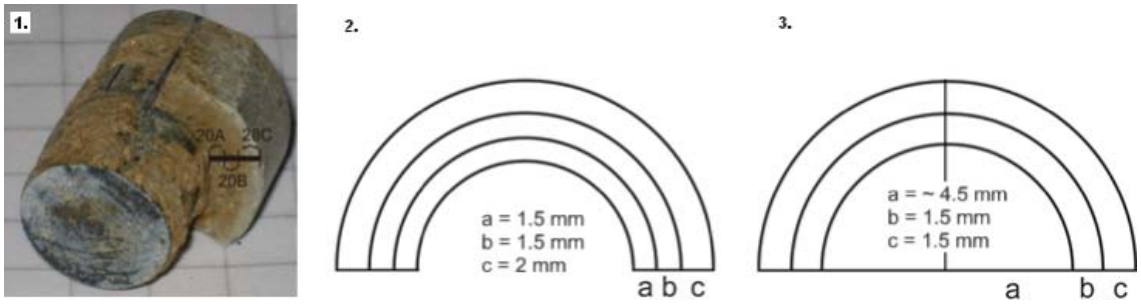

Figure 3-6. *(1) and (2)The thickness of the analysed layers from the cast iron surface towards Cu-vessel in samples 19 and 20. (3) The thickness of the analysed layers towards the Cu-vessel in sample 6.*

3.8 Physical properties

3.8.1 Water content

Water content of VTT samples (Figure 3-3) was measured gravimetrically after drying the sample at 105ºC for 24 h, directly after dismantling and also after swelling pressure and hydraulic conductivity measurements.

3.8.2 Grain density

Grain density was measured from samples 8 and 17 (Figure 3-3) after finishing swelling pressure and hydraulic conductivity measurements. Grain density measurements were performed in 1 M NaCl using volumetric flasks and analytical balance after Karnland et al. (2006). The result was used to calculate the dry density of the compacted samples.

3.8.3 Swelling pressure and hydraulic conductivity

Approximately 10 mm thick bottom profiles of Fe-bentonite and reference samples (samples 17 and 8, Figure 3-3) taken directly as they were after dismantling inside a glovebox, were fitted into 24 mm diameter fixed-volume steel swelling pressure cells equipped with 10 µm pore size filters on top and bottom. Test cells (with samples fitted in) were kept in the glovebox until transporting them to Clay Technology for swelling pressure and hydraulic conductivity measurements. Before the transport, the inlet and the outlet holes of test cells were sealed by connecting them with Teflon tubing to avoid drying and oxygenation of samples during transport.

Swelling pressure and hydraulic conductivity measurements were performed using an oedometer test set-up with deaerated water, nitrogen flushing, and closed circulation system in order to avoid oxygenation of the samples. The pressure transducer that was used for measuring the swelling pressure was calibrated and placed in test cell on the top of the moving piston. Deionized water was circulated once a day through top and bottom filters until swelling pressure was stabilized. For the hydraulic conductivity measurements, a GDS pump was connected to the system with valves. The water solution pressure at the bottom side of the samples was set to 1 MPa. The volume of solution that percolated the sample was measured and hydraulic conductivity calculated according to Darcy's law.

After the swelling pressure and hydraulic conductivity measurements from undisturbed bottom profiles were finished, samples were transported to B+Tech, dismantled under N_2-atmosphere, dried, ground gently in an agate mortar, and compressed to an approximate dry density of 1.5 g/cm^3.

Swelling pressure and hydraulic conductivity measurements were repeated after drying, mixing and recompacting the samples to verify the swelling pressure and hydraulic conductivity results from the undisturbed bottom profiles. The water solution pressure at the bottom side of the samples was set to 0.7 MPa. After finishing swelling pressure and hydraulic conductivity measurements, water content and grain density were measured.

4 Results and discussion

4.1 VTT's samples

4.1.1 Chemical composition of the gas

The design of VTT's long-term storage conditions resulted in three distinguishable gas phases; 1) the gas in the large storage vessel, 2) the gas in the PE-vessel with a reference sample, and 3) the gas in the PE-vessel with an iron/bentonite sample. These gases were analysed with regard to their content of H_2, CO_2 and O_2, see Table 4-1.

The results show that the gas concentrations are roughly the same in all three vessels, which demonstrate the well-known fact that that gas molecules can diffuse through the walls of the PE-vessels. Thus, the measured gas concentrations can be regarded as a triplicate sample of one common gas atmosphere in the large storage vessel.

The observed H_2 production was the result of corrosion of two cast iron cylinders; the one in the analysed cast-iron sample and another one in a not yet opened MX-80/cast iron sample, where the initial solution was Milli-Q water. The increased CO_2 content in the gas phase was most probably a result of dissolution of initial carbonates present in the MX-80 bentonite.

4.1.2 Solution chemistry

The external solution consisted of 0.5 M NaCl in all samples at the onset of the experiment. The solution chemistry changed slowly with time as a result of processes, such as ionic exchange and the dissolution of solids and also by mass transfer via the sinters. Table 4-2 summarizes the results from several chemical analyses performed after 0.75, 8.2, and 8.6 years. The values have been corrected with regard to the dilution of the external solution that took place during the gas sampling and filling the volume with water.

The Table 4-2 may erroneously seem to have several missing data. In a few cases data may be missing due to, e.g., measurement problems. However, the main reason for seemingly missing data is that the early study by Aalto et al. (2002) was made at such an early stage that there was no reason to expect measurable amounts of iron and copper in the external solution. Later on, prior to the opening of the 8.2 years old samples, it was decided that iron and copper should be added to the analyses, in order to estimate the extent to which the dissolution of the cast iron and the Cu vessel affected the water chemistry. Finally, prior to opening the 8.6 y old samples, it was decided to analyse also dissolved Si and Al, since these elements could possibly provide information about the dissolution of the montmorillonite component.

Table 4-1. Results from gas analyses. All values are given in vol-%.

Gas	Reference	MX-80/cast iron	Large storage vessel
O_2	< detection limit	< detection limit	< detection limit
CO_2	0.234	0.296	0.24
H_2	1.1	1.1	1.1

Table 4-2. Results from analyses of the external solution in contact with either a reference sample or the corresponding MX-80/cast iron sample after 0.75, 8.2, and 8.6 years. Concentration unit: mg/L. The initial external solution was 0.5 M NaCl solution (or, alternatively, ~11,495 mg/L Na and ~17,726 mg/L Cl). Alk is given in mmol/L. The subscripts Au and Pt refer to the type of electrode used.

	Reference			MX-80/cast iron			Method
	0.75 y* Sample 4	8.2 y Sample 9	8.6 y Sample 12	0.75 y* Sample 6	8.2 y Sample 10	8.6 y Sample 15	
pH	7.9	8.2	8.0	7.9	8.0	8.0	Orion pH-el.
Eh (mV)	61	–	-210_{Pt}	199	–	-488_{Pt}	Pt vs. LF-2
			-301_{Au}			-399_{Au}	Au vs. LF-2
Na	12,000	11,000	12,500	12,000	10,500	12,100	ICP-AES
Mg	100	163	190	100	238	270	ICP-AES
Ca	350	500	520	300	575	580	ICP-AES
Si	–	–	16	–	–	15	ICP-AES
Al	–	–	<0.5	–	–	<1	ICP-AES
K	83	96	86	66	58	60	FAAS
Cu	–	0.043	1.1	–	0.58	1.3	GFAAS
Fe_{tot}	–	4.4***	<0.03	–	<0.04	<0.05	ICP-AES
Fe_{tot}	–	3.89***	0.17**	–	0.07	0.39	Colorimetry
Fe^{2+}	–	0.02	–	–	0.03	0.24	Colorimetry
Fe^{3+}	–	3.87	–	–	0.04	0.15	Colorimetry
Cl^-	20,000	14,875	20,300	19,000	17,000	19,900	IC
SO_4^{2-}	700	1,225	1,200	570	975	1,000	IC
Alk	$6.7 \cdot 10^{-1}$	2.3	3.5	$6.7 \cdot 10^{-1}$	4.2	2.9	Titration

*Values from Aalto et al. (2002). **Only Fe_{tot} was measured. ***Probably false value caused by a malfunctioning sinter that leaked iron into the solution.

A brief look at Table 4-2 shows that:

1) The measured Na^+ and Cl^- concentrations did not change noticeably between the first and the eighth year, which indicates fairly undisturbed background chemistry. The given concentrations correspond roughly to that of 0.5 M NaCl.

2) The concentrations of K^+, Mg^{2+}, Ca^{2+}, and SO_4^{2-} were initially zero, but they have increased and seem, with the exception of K^+, to continue to rise even after 8 years. The Ca- concentration correlates roughly with the SO_4^{2-} concentration (Figure 4-1), which suggests that the main source of these ions is the congruent dissolution of gypsum, one of the components in MX-80.

3) The alkalinity of the solutions increased with time from about 0.7 meq/L after 0.75 y to about 3 meq/L after 8.6 years, probably as the result of calcite dissolution.

4) The redox-measurements carried out after 0.75 years indicated oxidising conditions in the samples. After 8.6 years, however, the conditions were truly reducing, with Eh values being –210 mV or less. The Eh-values were clearly lower in samples containing cast iron than in the corresponding reference samples. (No proper Eh-values could be achieved for the 8.2 years old samples, since they were exposed too long to the glovebox' N_2 atmosphere and became oxidised prior to measurements).

5) The pH values were approximately the same in all external solutions, with values ranging between 7.9 and 8.2.

6) The measured values in the reference samples are about the same as the corresponding ones in the MX-80/cast iron samples (with the exception of the above-mentioned redox-values), which suggests that the presence of cast iron did not have any major effect on the external solution chemistry.

Finally, the redox-conditions in the porewater inside the water-saturated MX-80 samples was studied by moving (under N_2) undisturbed parts of the cylindrical samples into squeezing cells and measuring Eh(Pt) as described earlier. The redox-conditions were clearly reducing; Eh(Pt) was about

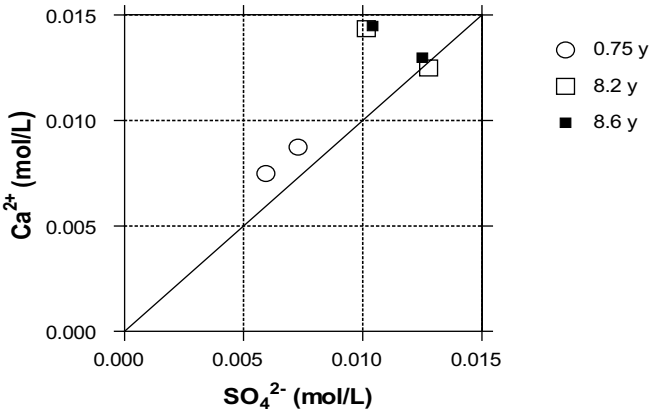

Figure 4-1. *Correlation between measured Ca^{2+} and SO_4^{2-} concentrations. Solid line: possible combined concentrations in case when dissolving gypsum is the only source of Ca^{2+} and SO_4^{2-}.*

–600 mV in the reference sample 12 and about –450 mV in the cast iron/bentonite sample 15. The water content of reference sample 12 was 27.7% (which corresponds to a dry density of 1.56 g/cm^3) as determined by using subsample 6 (see Figure 3-3). The water content of cast-iron/bentonite sample 15 was 20.3% (which corresponds to a dry density of 1.77 g/cm^3) as determined by using subsample 35 (see Figure 3-3). Due to technical problems no data on pH inside the water-saturated MX-80 samples were obtained.

4.1.3 Cation exchange capacity

Table 4-3 and Figure 4-2 show the CEC values as a function of the distance from the MX-80/sinter interface towards the cast iron. The average CEC in the reference samples was found to be 0.96 meq/g. The values were measured in the 8.2 y sample pair consisting of samples 9 and 10. All values in the diagram are slightly higher than normal, i.e. there seem to be a systematic error of about 5–10%. This is, however, not a problem when evaluating whether the presence of cast iron affected the CEC or not. CEC was later measured in the second 8y iron-clay sample pair, consisting of samples 12 and 15. The CEC values for these samples were slightly lower than those shown in Figure 4-2 and closer to what is normally observed; 0.87 meq/L (sample 12) and 0.86 meq/L (sample 15).

In case of the MX-80/cast iron samples, there was a tendency of getting higher CEC values closer to the cast iron surface (Figure 4-2). Although the existence of such a tendency is not conclusively proved by the five data points in the graph, it is supported by statistical methods, by considering similar type of analytical uncertainties for the CEC measurements (+/–5%). For example, the calculated Spearman's rank correlation coefficient is +1 and the two-tailed P value is 0.0167, which indicates a low probability of creating by chance the observed trend in the CEC data.

Table 4-3. CEC in five slices of MX-80 bentonite as a function of distance from the bentonite/sinter interface. The data are plotted in the diagram shown in Figure 4-2. The CEC values are mean values based on two measurements.

Distance (mm)	CEC (meq/g)	
	Cast iron	Background (reference samples)
–1.2	0.959	Value missing
–3.6	0.963	0.958
–6.0	0.971	0.964
–8.4	0.976	0.956
–10.8	0.991	0.954

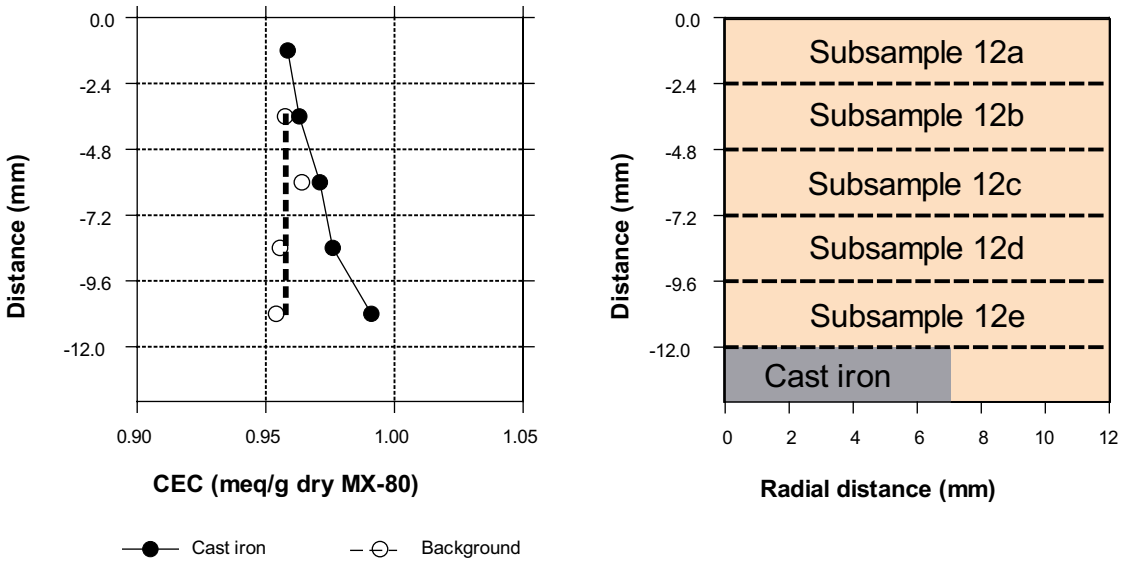

Figure 4-2. *Left: Measured CEC in five slices of MX-80 vs. distance from the MX-80/sinter interface. Right: The relative positions of the sinter, MX-80, and the cast iron are indicated for convenience.*

4.1.4 Mineralogy

XRD

The results of the analyses at the Geological Survey of Finland are presented in Figure 4-3 and Table 4-4. Mineralogical analyses of bulk fractions of bentonite were more or less identical with the 1st (samples 4, 15, and 16, Figure 3-3) and 2nd (samples 24 and 34, Figure 3-3) pair of samples, as well as with outer part and inner part of cast Fe containing sample, and that of cast Fe containing sample and reference sample. All samples contained among others, smectite, quartz, plagioclase, cristobalite, magnetite, pyrite, calcite, and apatite.

However, samples 14 and 37 scraped from cast Fe surface contained aragonite and hematite in addition to minerals identified from bentonite matrix (Figure 4-3). Analyses of clay fractions were also identical, and the clay mineral in all samples was dioactahedral smectite. Nevertheless, some small changes might have occurred in the mineralogy of clays.

Shift in d(001) line positions after ethylene glycol (EG) treatment was smaller in Fe-bearing samples than in reference samples (Table 4-4) suggesting that swelling ability of clay mineral had decreased. However, as position of d(001) line is susceptible to among others, differences in sample humidity, type of exchangeable cations present, and thickness of EG layer, it cannot be solely kept as an evidence of decrease in swelling ability or change in mineralogy.

The content of illite interlayers in illite/smectite was estimated from oriented and EG treated XRD patterns of clay fractions after the Moore and Reynolds (1989) method. The illite content increased slightly from 0 to 2% after Fe-interaction in the first sample pair, but the second sample pair did not show such change (Table 4-4). The change in the first sample pair is also so small that it is within error limit of the method, and thus cannot be kept as an evidence of transformation to illite.

Clay suspensions of Fe-enriched samples (15C, 16C and 34C, Figure 3-3) were initially reddish brown in colour, but after drying in glovebox air converted to light greenish in colour. This indicates that the iron was initially in ferric state and was reduced to ferrous iron during drying in N_2-air. Additionally, the iron seemed to be present in very reactive form. During the XRD analyses, which took approximately one hour, all sample mounts kept their greyish (reference samples) or greenish (Fe-enriched samples) colour suggesting that the oxidation of Fe was slow during the XRD analysis, as long as the mounts were prepared in N_2-atmosphere

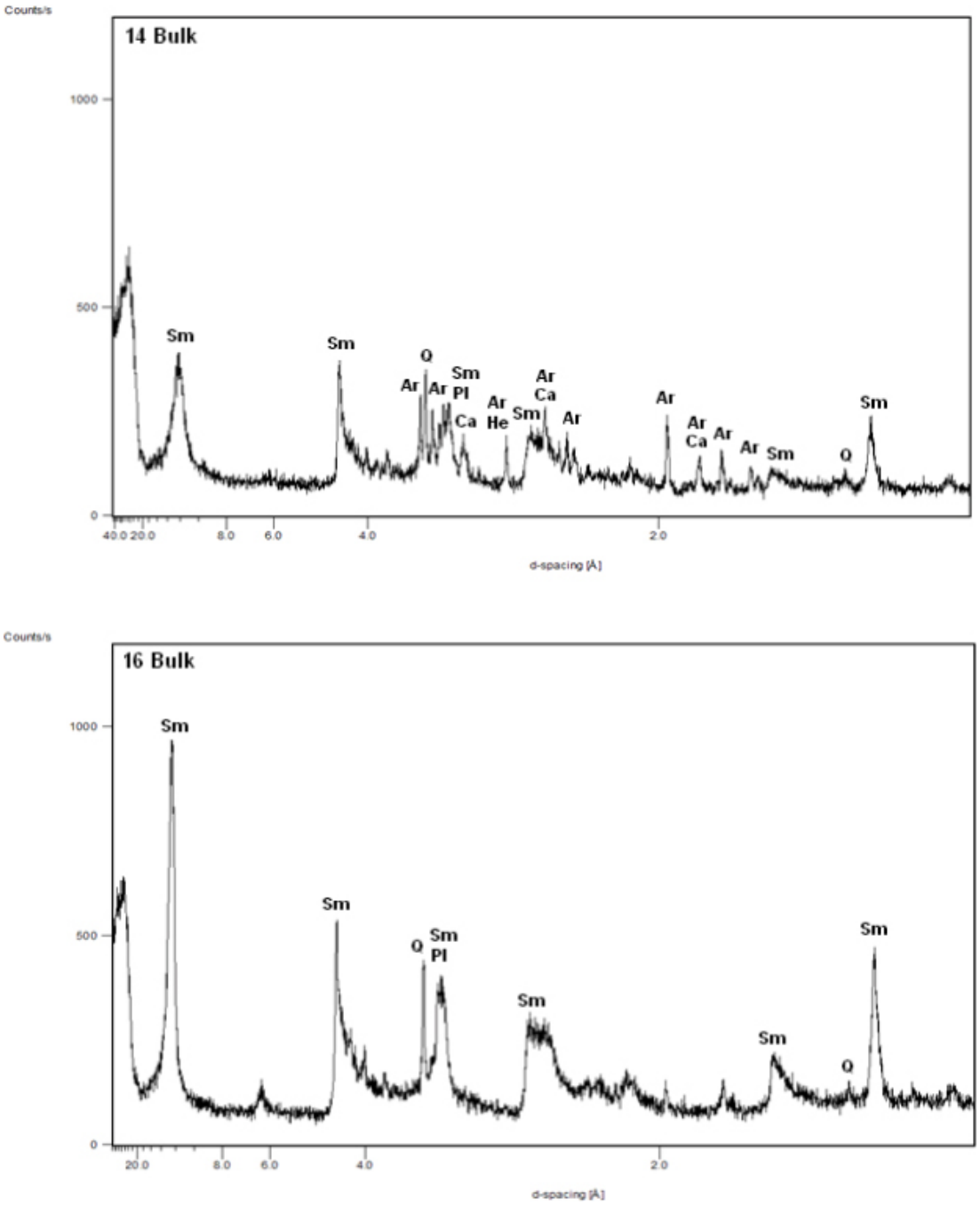

Figure 4-3. *XRD-patterns of sample 14 (cast Fe surface) and 16 (bentonite closest to cast Fe surface) bulk fractions. Peaks of some minerals present in both samples (smectite (Sm), quartz (Q) and placioglase (Pl)) are marked to both XRD patterns. In addition, some aragonite (Ar), calcite (Ca) and hematite (He) peaks in the XRD pattern of sample 14 scraped from cast Fe are marked.*

The results of the analyses at MAX-lab, Lund (S) are presented in Figures 4-4–4-7. XRD data was collected for the reference clay (sample 7, Figure 3-3) and the iron-bentonite clay (sample 20, Figure 3-3) (i) as received, (ii) as an Mg-exchanged clay solvated with ethylene glycol, and (iii) as an iron-bentonite sample dispersed in water. XRD data were collected at +20°C and –50°C. Each sample was spatially probed in order to get information regarding the heterogeneity of the samples.

Table 4-4. Shift in (001) line positions due to EG treatment, and illite content in I/S determined based on Moore and Reynolds (1989) method for oriented, Mg-exchanged clay fractions.

	Swelling – d(001) line shift			Illite content - M&R method	
	Oriented d(001)	+EG d(001)	°Δd d(001)	+EG °Δ2θ	+EG I in I/S
1st sample pair					
Ref. 4C	13.36	16.44	3.18	5.30	0.0
Fe. (outer) 15C	13.37	16.30	2.98	5.33	1.7
Fe. (inner) 16C	13.38	16.12	2.82	5.34	2.1
2nd sample pair					
Ref. 24C	13.89	16.72	2.83	5.26	0.0
Fe. 34C	14.19	16.67	2.48	5.30	0.0

When comparing the two-dimensional diffractograms of the iron-bentonite sample and the reference sample (Figure 4-4) one finds that there are somewhat more diffraction spots from larger grains or crystals in the iron-bentonite samples compared to the reference samples. The reference sample was a two-layer hydrate smectite (001 at 15.6 Å, Figure 4-5) and the iron-bentonite sample was a mixed one-layer-hydrate and two-layer-hydrate smectite (12.6 and 14.7 Å). Small amounts of quartz (Q) and cristobalite (C) are seen at 4.26 and 4.05 Å, respectively. The following new reflections were identified in the iron-bentonite compared to the reference clay: 10.0, 6.48, 5.85, 5.66, 4.17 and 3.77 Å. The 10 Å phase is likely illite or mica. Due to the experimental conditions reflections lower than approximately 3.6 Å could not be detected, which made identification of new phases much more difficult. Various hydrated Mg-carbonates have peaks in the area (nesquehonite at 6.48 Å and hydromagnesite at 5.80 Å) and the Na-Al-carbonate dawsonite has a reflection at 5.67 Å (Brindley and Brown 1980, pp 349–356). Further data at higher angles (lower d-spaces) need to be collected in order to correctly determine the phases.

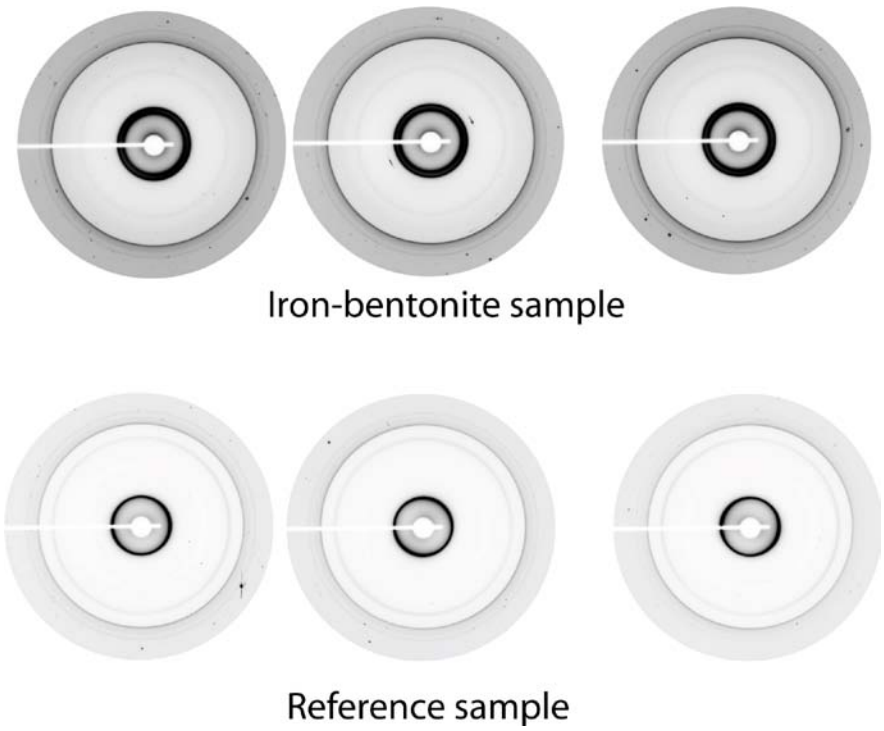

Figure 4-4. *Example of two-dimensional X-ray diffractograms of the iron-bentonite sample and the reference sample as received. Each diffractogram represents data collected at different locations in the capillary.*

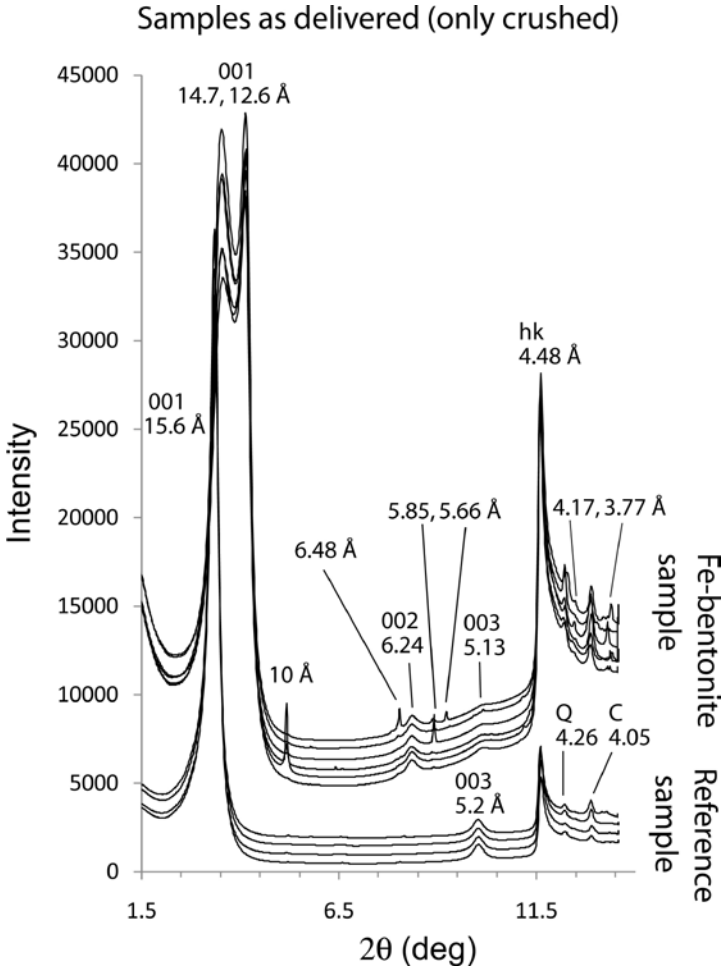

Figure 4-5. *Integrated X-ray diffractograms of an iron-bentonite sample and a reference sample at various sample positions. The analysed samples were crushed but otherwise as delivered. Q = quartz and C = cristobalite.*

When the samples were Mg-exchanged and solvated with ethylene glycol, characteristic basal spacings of 17 Å were identified for the smectite. No significant change can be seen in d-values (Figure 4-6) or in Δ(002/003), which is an indication of illite interstratifications in the smectite (Moore and Reynolds 1997, p 273).

When the iron-bentonite sample was dispersed in deionised water a mixture of three-layer-hydrate and free swelling smectite was identified (Figure 4-7, +20°C). This is expected for a smectite with mixed mono- and divalent interlayer cations. When the sample is cooled down to –50°C the smectite interlayer distance decreases (to 15.6 Å) as the water leaves the clay and forms ice (3.91 Å, Figure 4-7, –50°C). This indicates that the swelling of the iron exposed clay is very similar or identical to any Na/Ca – smectite, and hence unchanged (Svensson 2009).

FTIR

Samples taken from 5 variable distances from cast iron showed slight increase in intensity of 845 cm^{-1} bending indicating either increase octahedral AlMgOH or FeFeOH. Decrease in intensity of 798 cm^{-1} band towards cast iron indicated decrease in ‘free’ silica, which was consistent with the observations in chemical analysis on decrease in total silica content in the close vicinity of cast iron (Figure 4-8). No changes in any band positions were seen.

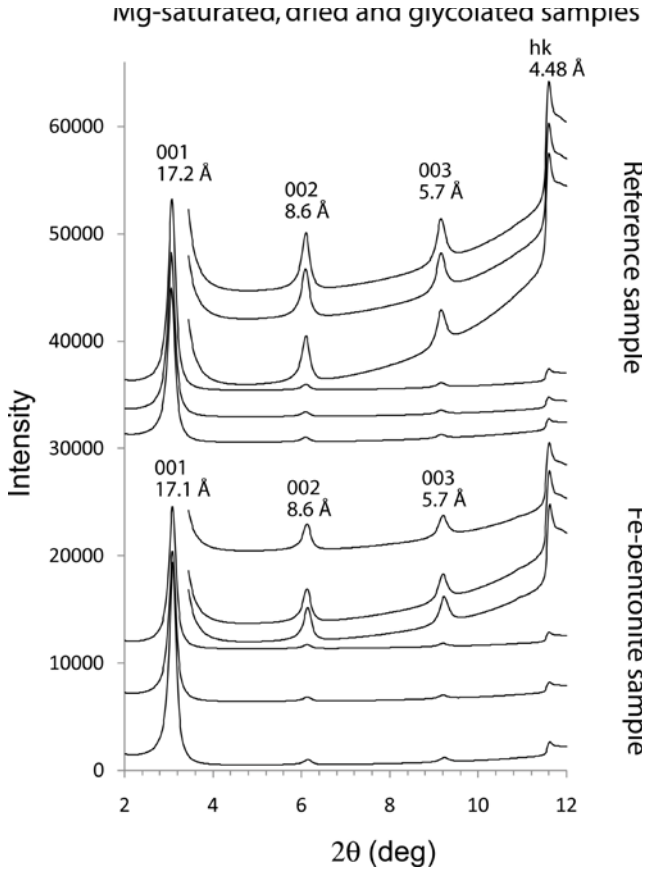

Figure 4-6. *Integrated X-ray diffractograms of Mg-exchanged, dried and ethylene glycol saturated samples (iron-bentonite and reference sample) at various sample positions. The basal reflections 001, 002, 003 and the in-plane reflection hk of montmorillonite are visible at 1x and 10x scaling.*

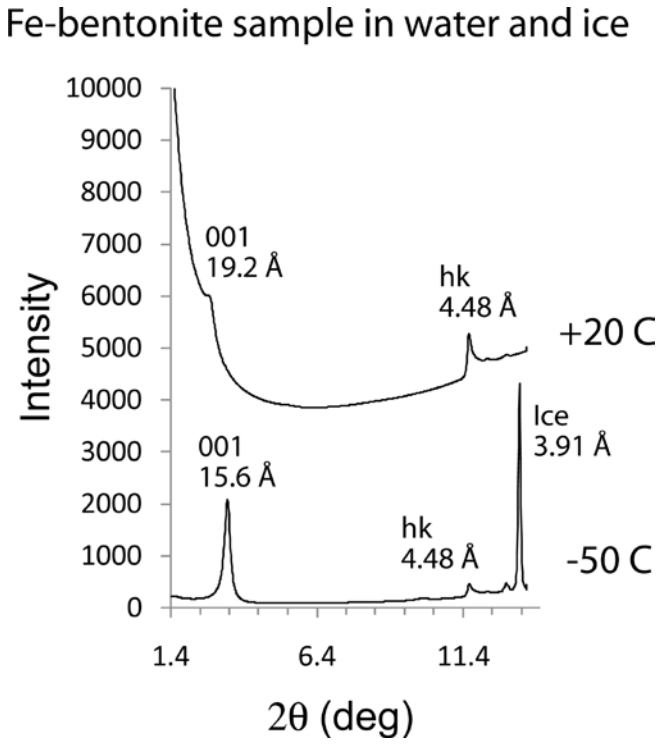

Figure 4-7. *Integrated X-ray diffractograms of iron-bentonite in water and ice at +20°C and –50°C.*

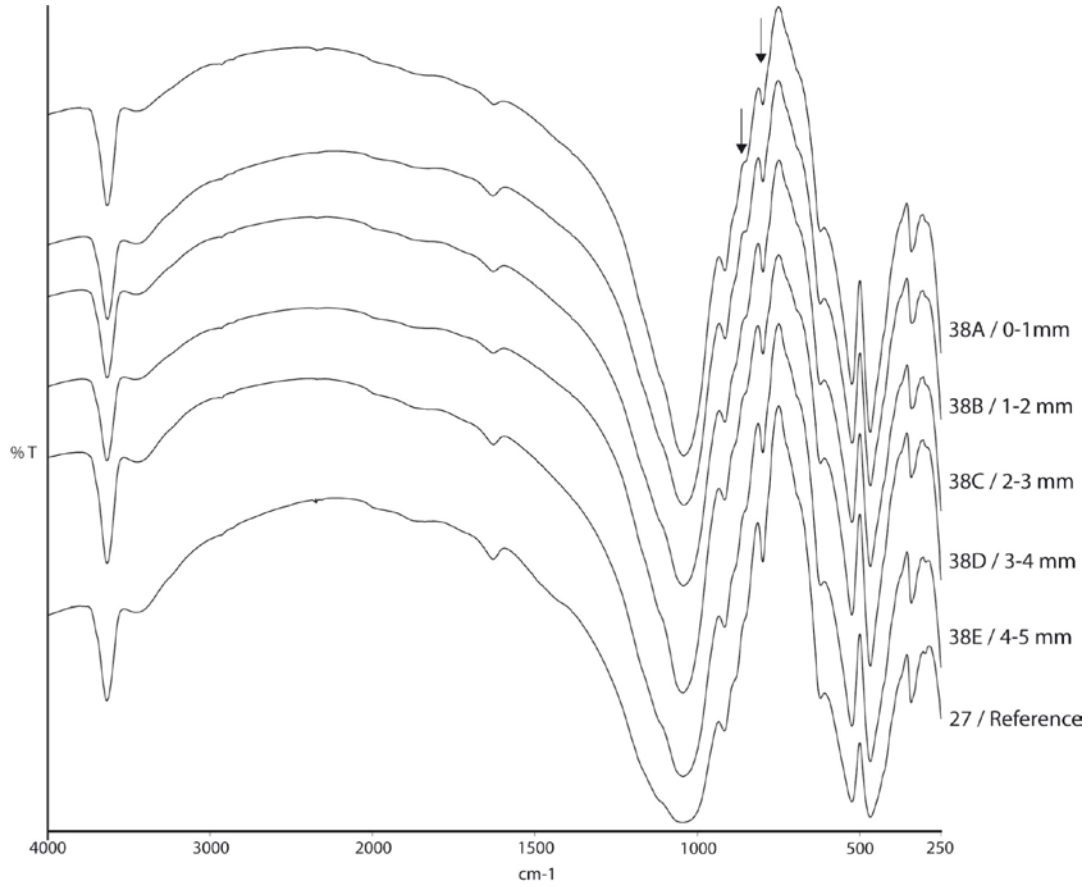

Figure 4-8. *FTIR-patterns of VTT's samples taken from 5 variable distances from iron cast (38a–38e in Figure 3-3) and from reference sample (27 in Figure 3-3). Arrows indicate detected changes and are described sequentially from left to right in the text.*

Mössbauer spectroscopy

The fitted Mössbauer spectra are displayed in the Figures 4-9–4-11. The fittings and part of the discussion are provided by Johan Lindén, Åbo Akademi. The four spectral components, all corresponding to various Fe species are shown. By visual inspection Sample 33a and 37 are rather similar. They also give the best signal, as their Fe contents are highest and they have the most narrow line widths: 0.30 and 0.31 mm/s, respectively. Sample 23 has a considerably larger line width: 0.38 mm/s, perhaps due to less perfect crystallinity caused by oxidation.

In all the spectra, the dominating component is paramagnetic with a very large quadrupole coupling constant $eQV_{zz} \approx 3.0$ mm/s (Component 1 in Table 4-5). This component also has a large isomer shift, which is typical of divalent Fe. The same feature was reported in the study by Carlson et al. (2007). It is typical for Fe containing bentonite materials.

On the inner slope of the first line of Component 1 additional paramagnetic features are seen. These peaks were accounted for using two quadrupole components (Components 2 and 3, in Table 4-5), as a single component was not enough to explain these features. Both components can be attributed to trivalent Fe, based on their isomer-shift values. Only one such component was reported by Carlson et al. (2007). However, they might correspond to almost the same chemical environment, reflecting a less than perfect local crystallinity of the trivalent Fe species. This observation may be true if it is the result of a low-temperature oxidation of the divalent component.

All three spectra exhibit very weak magnetic features, which were fit using an ordinary magnetic sextet (Component 4, in Table 4-5). The magnetic features in samples 23, 33a and 37 were fit with internal field values of 43–46 T. These values could, in principle, be due to either Fe^{2+} or Fe^{3+}. Specific assignment is made difficult by the fact that the magnetic lines are very close to the

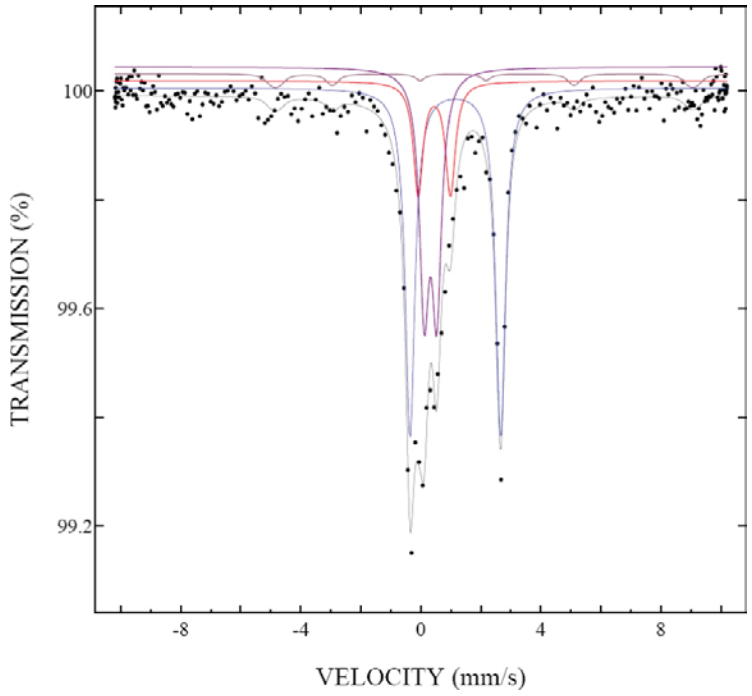

Figure 4-9. *Mössbauer spectrum recorded from sample 23 (reference) at 77 K. The black circles represent measured data and the black line represents a 4-component fit to the data. The blue, red, violet, and brown lines correspond to components 1-4, respectively.*

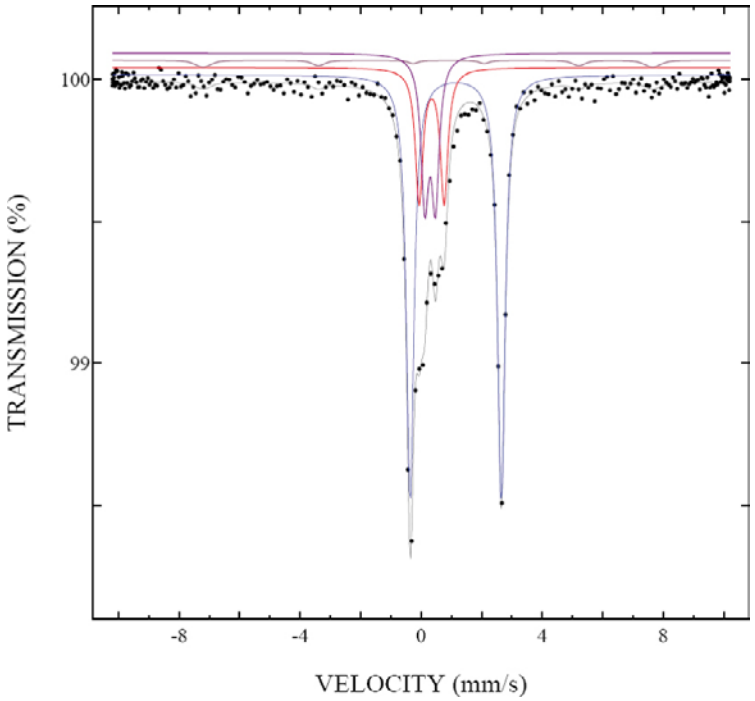

Figure 4-10. *Mössbauer spectrum recorded from sample 33a at 77 K. The black circles represent measured data and the black line represents a 4-component fit to the data. The blue, red, violet, and brown lines correspond to components 1-4, respectively.*

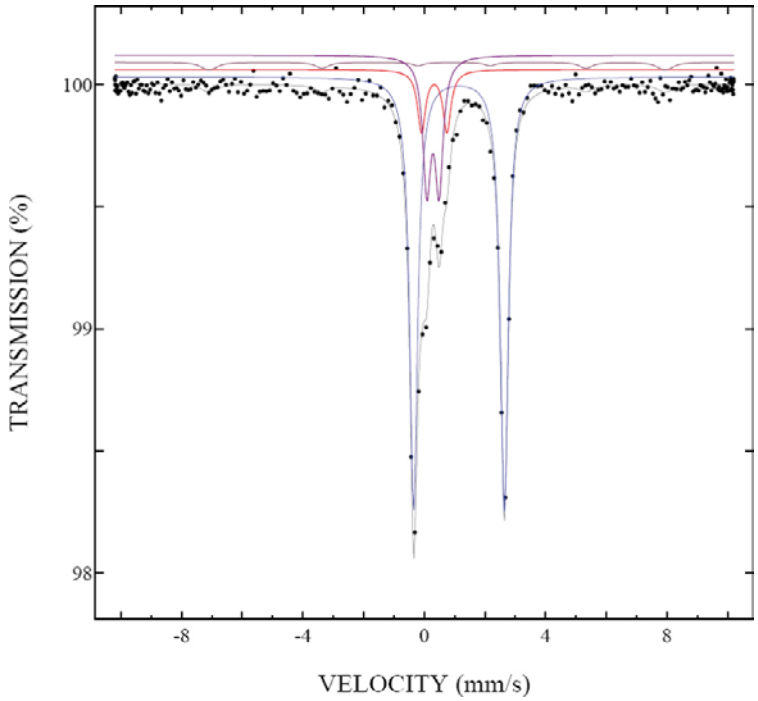

Figure 4-11. *Mössbauer spectrum recorded from sample 37 (corrosion products) at 77 K. The black circles represent measured data and the black line represents a 4-component fit to the data. The blue, red, violet, and brown lines correspond to components 1-4, respectively.*

detection limit, which strongly affects the reliability of the fitted isomer-shift values. Nevertheless, in sample 23 the isomer shift value of Component 4 is extremely high, strongly indicating Fe^{2+}. Also the somewhat lower magnetic field points in the same direction. Thus, Component 4 in sample 23 seems to differ from that in samples 33a and 37, due to the lower field and higher isomer shift. In samples 33a and 37, the isomer shift values of Component 4 would also indicate the divalent state. However, due to the extreme weakness of the lines, assignment of the valence state should not be done. There is also the possibility that there is more than one magnetic component (e.g. in magnetite), causing enhancement of overlapping lines and reduction of non-overlapping lines. This possibility might explain why the 6th line is clearly visible in all spectra but the others are not. In any event, the overall portion of magnetic Fe in the samples cannot be determined unambiguously.

The main result of the analyses, i.e., the ratio of paramagnetic Fe^{2+} to Fe^{3+}, is readily obtained from Table 4-5. Assuming the recoil-free fraction to be the same for all components, the valence ratio is the intensity of Component 1 to that of Components 2 + 3, where the magnetic component has been omitted as its valence assignment is not clear. The corresponding ratios are presented in Table 4-6. Previous results are included in Table 4-6 for comparison.

According to the chemical analysis of the reference sample 29b (section 4.1.5.3), the reference material used in these tests contains 2.52 wt% of iron. Considering that each Mössbauer specimen contained 50 mg of bentonite material, it can be estimated that each specimen contained initially 1.26 mg of iron. The area (A) of the Mössbauer spectrum of each sample is presented in Table 4-7. Using these values, the total amount of iron in each sample is estimated (Table 4-7). Using the fitted intensities of the different spectral components (from Table 4-5), the amount of iron related to these components is estimated and shown in Table 4-7 as well.

Table 4-5. Hyperfine parameters.

	I [%]	Δ [mm/s]	δ [mm/s]	B [T]
Sample 23				
Component 1	47.8	3.014	1.256	
Component 2	15.4	1.07	0.56	
Component 3	31.3	0.42	0.43	
Component 4	5.6	1.0(3)	1.7(3)	43(1)
Sample 33a				
Component 1	59.1	3.013	1.254	
Component 2	18.5	0.82	0.46	
Component 3	19.8	0.35	0.40	
Component 4	2.6	–0.7(2)	0.7(3)	46(1)
Sample 37				
Component 1	67.0	2.986	1.251	
Component 2	9.6	0.84	0.44	
Component 3	20.0	0.40	0.40	
Component 4	3.3	–0.6(2)	0.8(3)	46(1)

Table 4-6. Ratio of Fe^{2+} and Fe^{3+} in the 8 y VTT samples and reference. Previous results from iron-bentonite-study of Carlson et al. (2007) are included for comparison.

Sample	Fe^{2+}/Fe^{3+}
Sample 23. Reference	1.024
Sample 33a. FeBe	1.543
Sample 37. Corrosion products	2.264
MX-80 (Carlson et al. 2007)	0.565
Coupon 30°C (Carlson et al. 2007)	0.605
Coupon 50°C (Carlson et al. 2007)	0.541
Wire 30°C (Carlson et al. 2007)	2.861
Wire 50°C (Carlson et al. 2007)	3.545

Table 4-7. The amounts of iron in the samples causing different spectral components.

Sample	A [%*mm/s]	$m_{Fe\ in\ sample}$ [mg]	$m_{Fe\ in\ comp.1}$ [mg]	$m_{Fe\ in\ comp.2}$ [mg]	$m_{Fe\ in\ comp.3}$ [mg]	$m_{Fe\ in\ comp.2+3}$ [mg]	$m_{Fe\ in\ comp.4}$ [mg]
23. ref.	1.03537	1.260	0.602	0.194	0.394	0.588	0.071
33a. FeBe	1.52470	1.855	1.096	0.343	0.367	0.710	0.048
37. corr.	1.66566	2.027	1.358	0.195	0.405	0.600	0.069

A clear increase in the amount of iron (Fe^{2+}) corresponding to spectral component 1 can be observed. Due to the fact that components 2 and 3 most likely correspond to almost the same chemical environment, their combined mass is used for analysis (see Table 4-7). The combined mass of Fe^{3+} remains essentially constant through all the samples. The amount of iron corresponding to components 2 and 3 varies slightly (perhaps due to the growth of component 1). The increasing amount of Fe^{2+} might affect the local environment around Fe^{3+}. In order to reveal the nature of the paramagnetic Fe^{3+} species, i.e, whether there really are one or two such species, measurements at a lower Doppler velocity should be performed. Room-temperature measurements might suffice if the epoxy mixture is sufficient to prevent the sample from oxidizing. However, as the doublet due to Fe^{2+} is well resolved from the Fe^{3+} species, the overall ratio between paramagnetic Fe^{2+} and Fe^{3+} will not change in further measurements, provided the assumption about the recoil-free fractions hold.

Traces of (3–5% of the total intensity) magnetic Fe was observed. The low amount of magnetically split species suggests that no significant quantities of iron oxides or oxyhydroxides were formed (Carlson et al. 2007).

These Mössbauer results indicate that the amount of Fe^{3+} remains constant and only the amount of Fe^{2+} is increasing. Previously it was stated that the change in the proportion of Fe^{2+} could be due to reduction of the octahedral iron in the montmorillonite and/or the fact that most of the iron leaching into the bentonite was divalent (Carlson et al. 2007). The results of these measurements imply that the latter is more probable. Additionally, the fitted parameters for Fe^{2+} in the samples, which were in contact with iron, differed only slightly from those for the reference. This similarity might indicate that the additional Fe^{2+} in the samples occupies an environment similar to the original Fe^{2+}.

XANES

XANES data were collected for the standard MX-80, reference sample (sample 7, Figure 3-3) and samples from iron-bentonite experiment (cut radially from sample 20, Figure 3-3) as well as additional reference compounds of known composition. The Fe^{II} reference was siderite $FeCO_3$ and the Fe^{III} reference synthetic Fe_2O_3. Kinetic XANES data were also captured as clay scrapings from the iron-tube was exposed to ambient atmosphere and allowed to oxidize.

XANES data for Fe_2O_3 (pure Fe^{III}), Fe_3O_4 (2 x Fe^{III} + 1 x Fe^{II}) and $FeCO_3$ (pure Fe^{II}) can be seen in Figure 4-12. The absorption edge of Fe^{II} dominating compounds is lower in energy compared to Fe^{III} compounds. The difference in edge energy is about 2 eV. In Figure 4-13 bulk MX-80 is compared to the iron standards. MX-80 is clearly dominated by Fe^{III} however there seems to be small amounts of Fe^{II}. In Figure 4-14 the entire absorption edge from –150 to +500 eV of the reference clay sample and the MX-80 bulk can be seen. The MX-80 bulk and the reference are identical in shape and edge position, indicating that the iron redox chemistry of the reference compound (sampled in the central part) is unchanged.

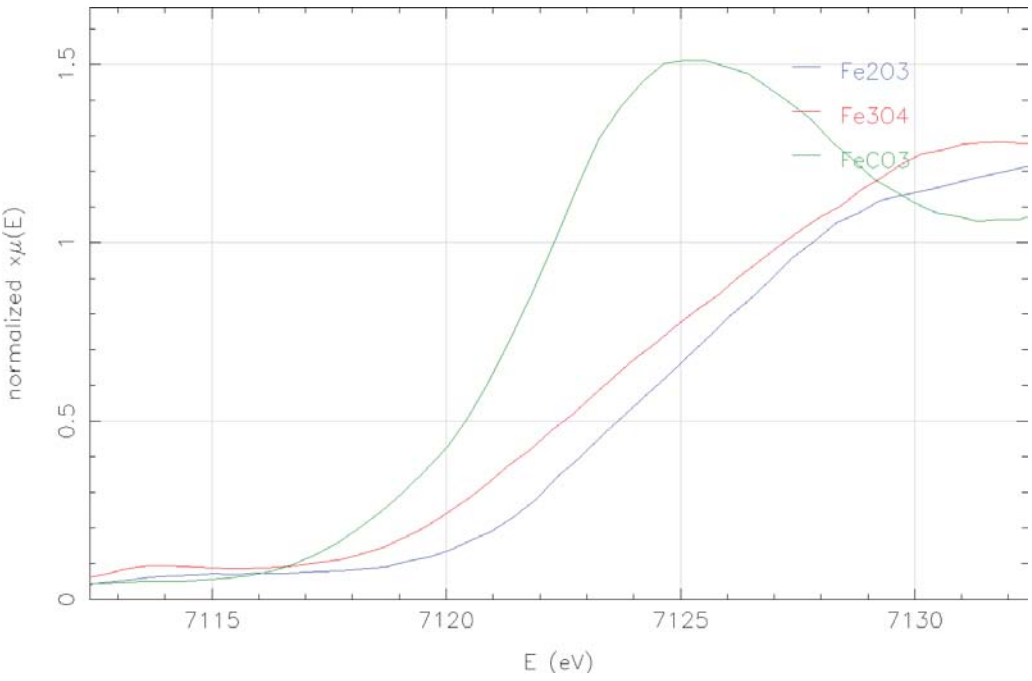

Figure 4-12. *Comparison of absorption edges of Fe_2O_3 (pure Fe^{III}), Fe_3O_4 and $FeCO_3$ (pure Fe^{II}).*

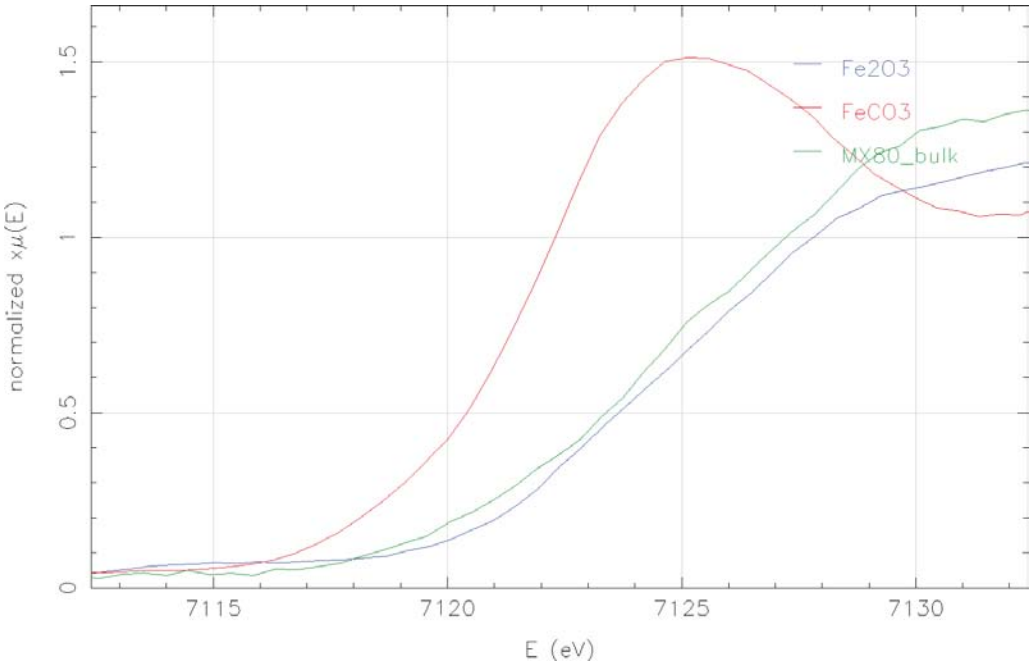

Figure 4-13. *XANES data of MX-80 bulk clay compared to of Fe_2O_3 (pure Fe^{III}) and $FeCO_3$ (pure Fe^{II}).*

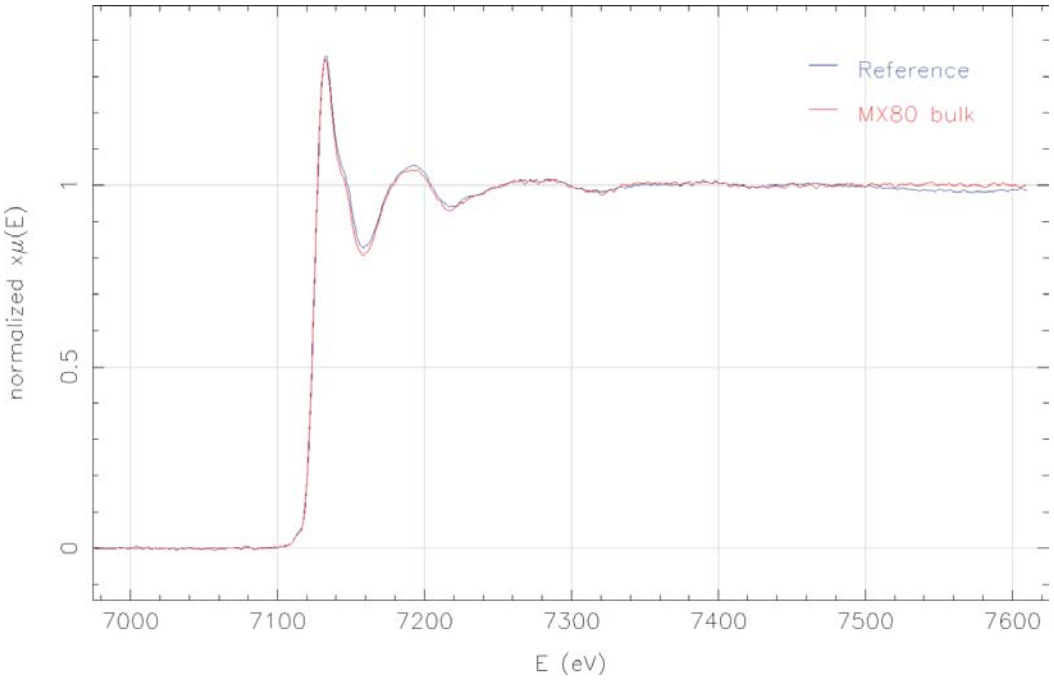

Figure 4-14. *Entire absorption edge (–150 to +500 eV) of reference clay sample and MX-80 bulk.*

Figure 4-15 demonstrates that samples from the iron-bentonite experiment have higher Fe^{II}/Fe^{III} ratio compared to the reference clay (absorption edge at lower energy). The sample highest in Fe^{II} was the scraping directly towards the iron-tube. This sample was later exposed to ambient atmosphere and kinetic XANES data were captured for 38 minutes. During the time period a small but significant oxidation of the iron in the sample was noticed (Figure 4-16).

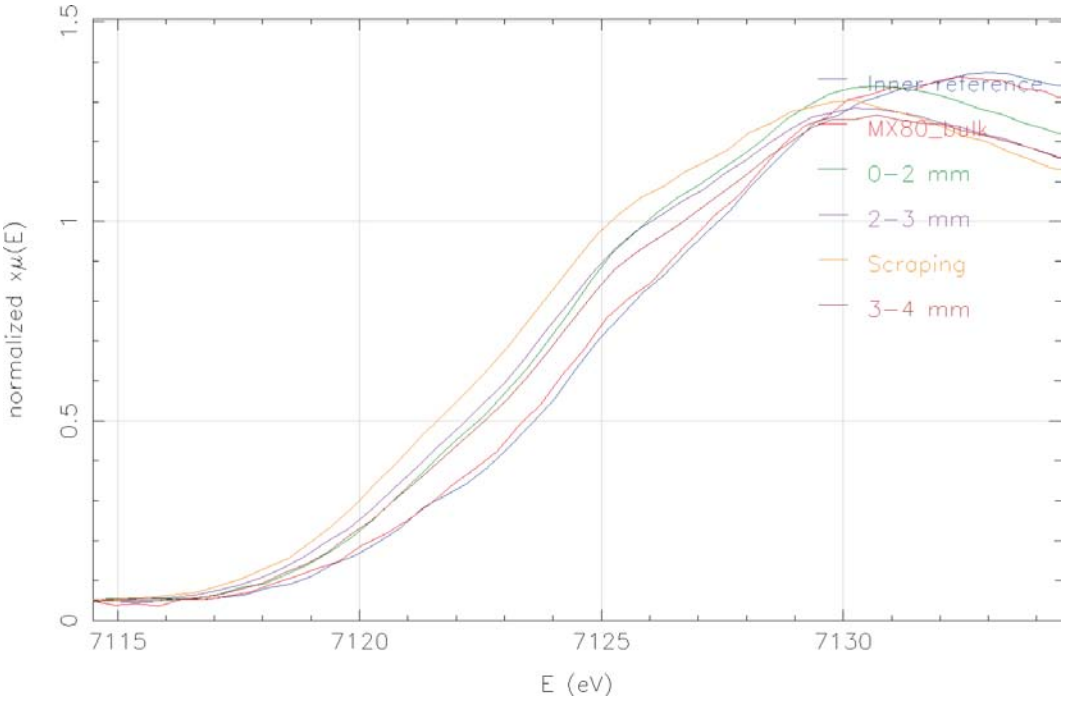

Figure 4-15. *XANES data of radially sampled iron-bentonite sample (to the left), reference sample and MX-80 bulk clay (the two spectra to the right).*

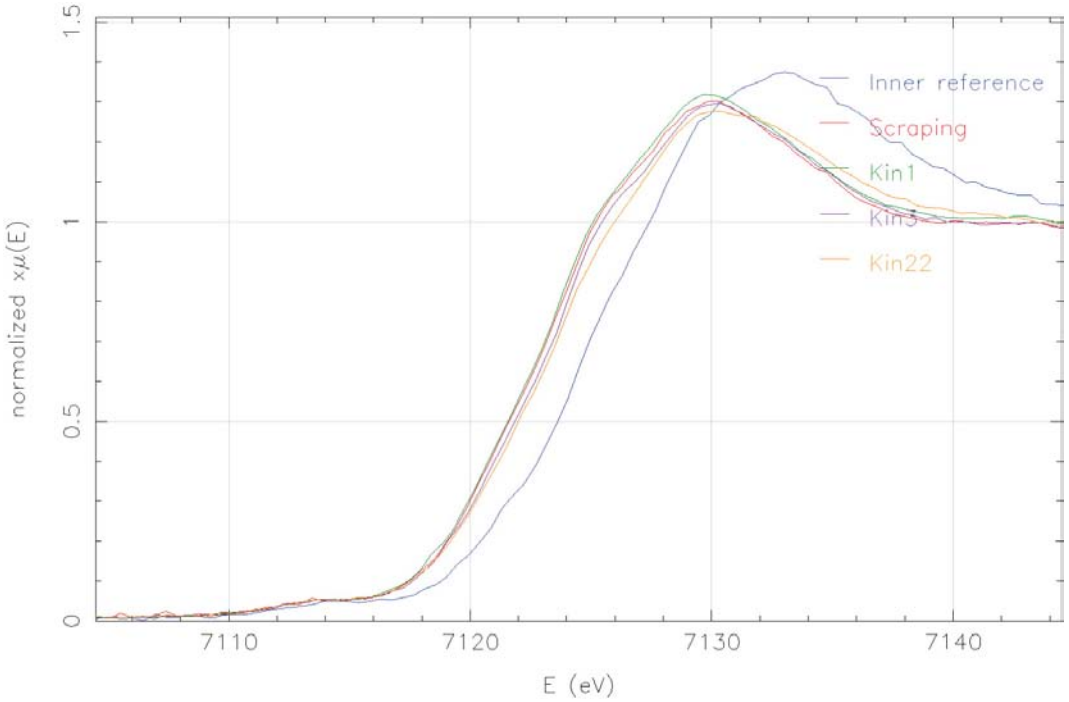

Figure 4-16. *Kinetic collection of XANES data of scraping clay from the iron-tube, compared to the reference sample. Data was collected for 38 minutes (22 spectra).*

Quantification of Fe^{II} using linear-combination of standards ($FeCO_3$ and Fe_2O_3) is shown in Figure 4-17.

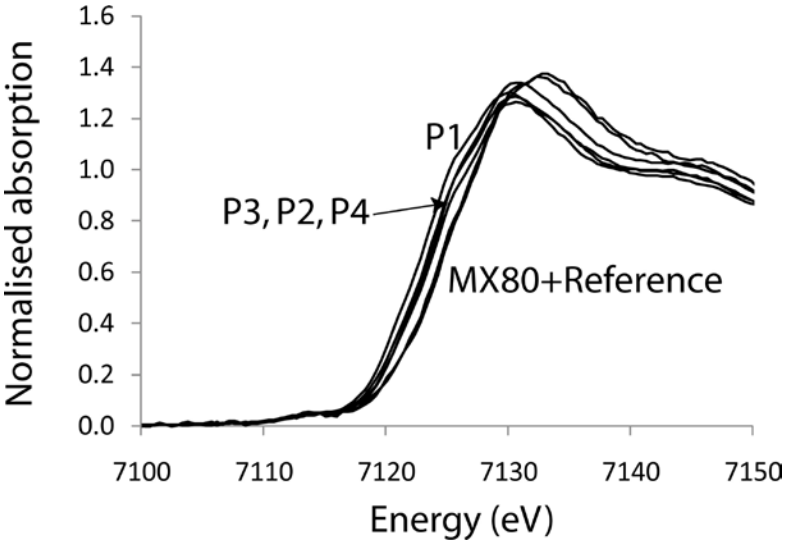

Figure 4-17. *Quantification of Fe^{II} using linear-combination of standards ($FeCO_3$ and Fe_2O_3): P1 = scraping = 35% Fe^{II}, P2 = 0–2 mm = 22%, P3 = 2–3 mm = 26%, P4 = 3–4 mm = 20%.*

4.1.5 Chemical composition of the bentonite

SEM

SEM-EDS analyses taken from the undisturbed top (1st pair) or bottom (2nd pair) profile from steel sinter inwards of the sample (towards cast Fe), and from the undisturbed side profile from Cu vessel inwards of the samples (towards cast Fe) showed a clear increase in Fe content (Figure 4-18). The iron content increased from 5 to 21 wt % in top profile of first sample pair. In other samples (side profiles and bottom profile of 2nd sample) the increase was much more restrained. This difference might have resulted from the loss of some bentonite in profiles stucked to the cast iron. The increase in Fe content was highest within 0.5 mm closest to cast iron (Figures 4-18 and 4-19b).

Except for Fe in pyrite grains that were initially present in bentonite (Figure 4-19e), iron was scattered evenly within the bentonite matrix (Figure 4-19b).

Additionally, a small decrease in Si content in top/bottom profiles was observed. No clear trends in contents of Al, Na, Ca or Mg were found (Figure 4-18).

Ca-carbonate had precipitated in the fractures of bentonite in contact with cast Fe (Figure 4-19c). This supports the XRD observations on aragonite precipitation on the surface of cast iron. Similar observations on carbonate precipitation in bentonite close to carbon-steel wires were made by Milodowski et al. (2009).

In reference sample (sample 22), darker areas that were enriched with Cl were observed (Figure 4-19d). The amount of such Cl-enriched areas was highest close to the sinter interface decreasing gradually sample inwards (Figure 4-20). Similar kind of dark Cl-enriched patches were found also in other sample profiles, but the amount of them was smaller, and their distribution not as clear as in reference sample bottom profile 22.

The bentonite matrix close to the cast iron had not developed as frequent cracking features as further away from cast iron. Such cracking features are drying artefacts formed during the SEM mount preparation (Figure 4-19e). Differences in cracking behaviour seem to indicate a cementation effect due to the presence of metallic Fe.

Cu was observed by EDS analysis in a couple of dense mineral grains, but its presence could not be correlated exclusively to the Cu-vessel contact, and therefore thought to be initially present in the bentonite.

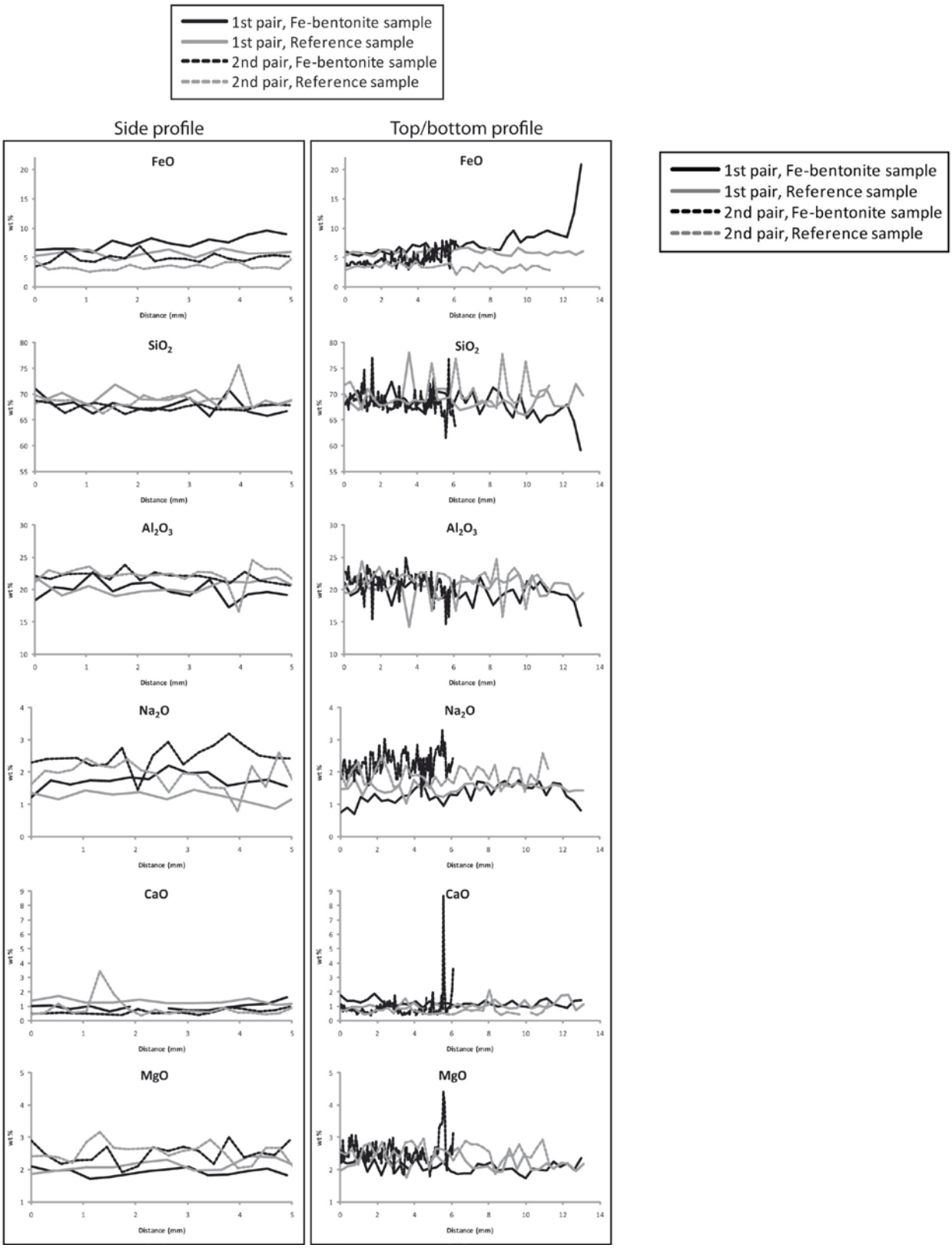

Figure 4-18. *Semiquantitative chemical composition determined with SEM-EDS from Cu-vessel (side profile) or from steel filter (top/bottom profile) inwards of the sample.*

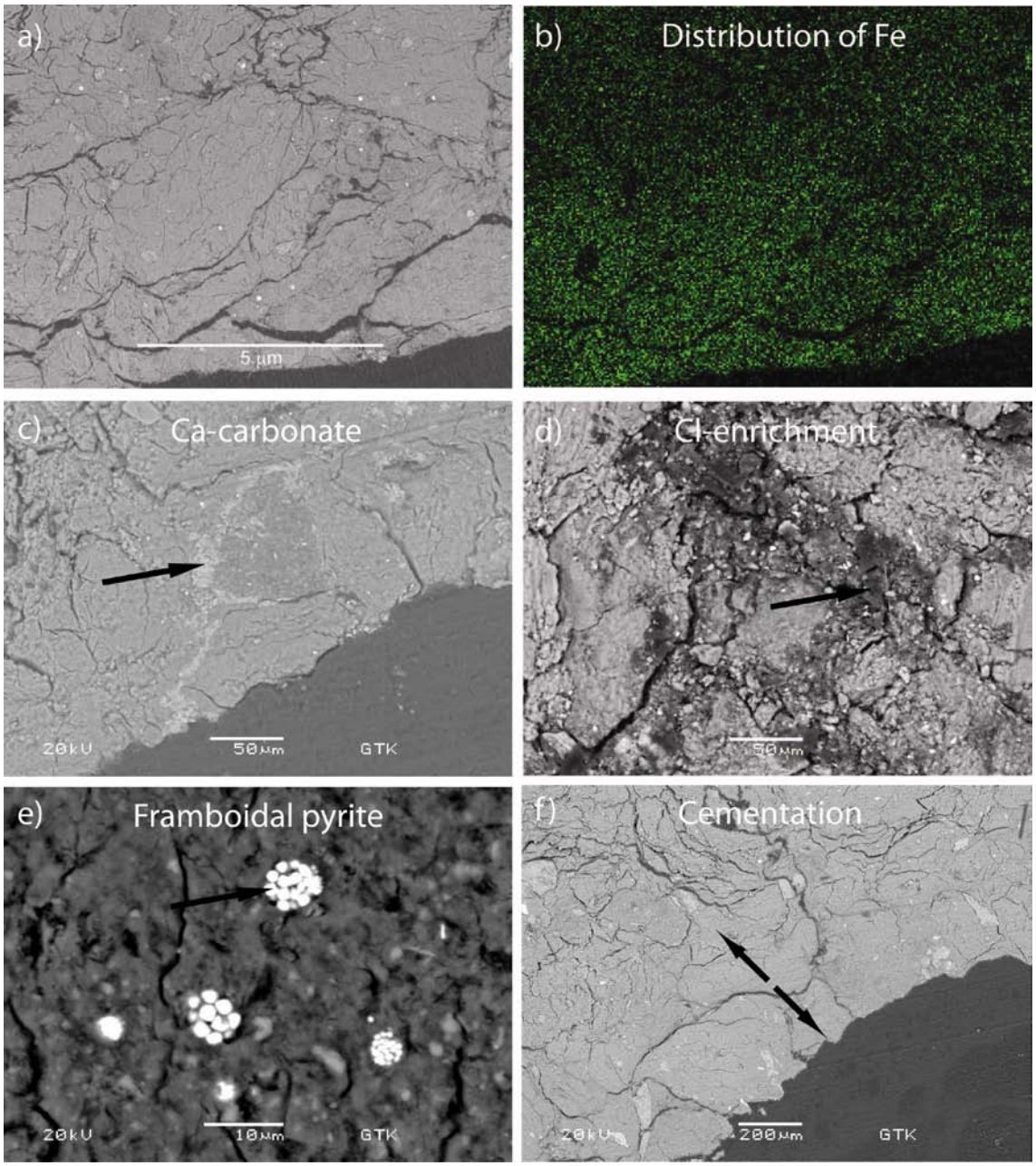

Figure 4-19. *SEM-pictures. a) Bentonite at the cast Fe boundary, which is the dark region at the lower right corner; b) Picture from the same area as in previous picture. Distribution of Fe (in green) in bentonite; c) Ca-carbonate precipitated in fractures close to cast Fe; d) Enrichment of chloride (dark grey areas) in bentonite matrix in reference sample; e) Initially present < 2 µm framboidal pyrite grains; f) Less cracking of bentonite close to the cast Fe, caused possibly by cementation effect.*

Exchangeable cations

Exchangeable cation extractions made on a sample containing cast iron, showed elevated concentrations of exchangeable Fe close to the cast iron. Figure 4-21 shows how the Fe concentration increases with distance between the steel sinter and the cast iron. Also other elements showed small trends: Mg decrease, and K increase towards cast Fe (Figure 4-21, Table 4-8). However, these trends were similar both for Fe-bentonite and reference samples. The decrease in exchangeable Mg towards cast Fe was the same order of magnitude as increase in exchangeable Fe, which could indicate replacement of Mg by Fe in cation exchange sites. However, an origin of Fe from the dissolution of poorly crystalline Fe phases, e.g. $Fe(OH)_2$ or green rust during the extraction procedure cannot be excluded.

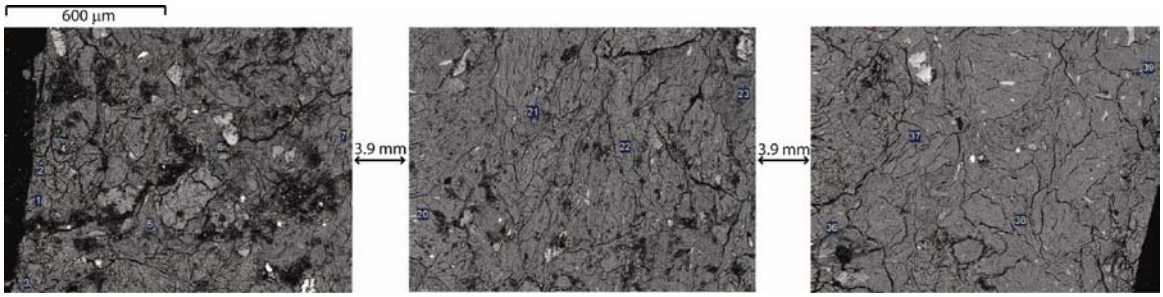

Figure 4-20. *SEM-pictures from reference sample profile 22 showing gradually decreasing trend in Cl-enriched darker patches from the sinter interface (in left) towards inwards of the sample (in right).*

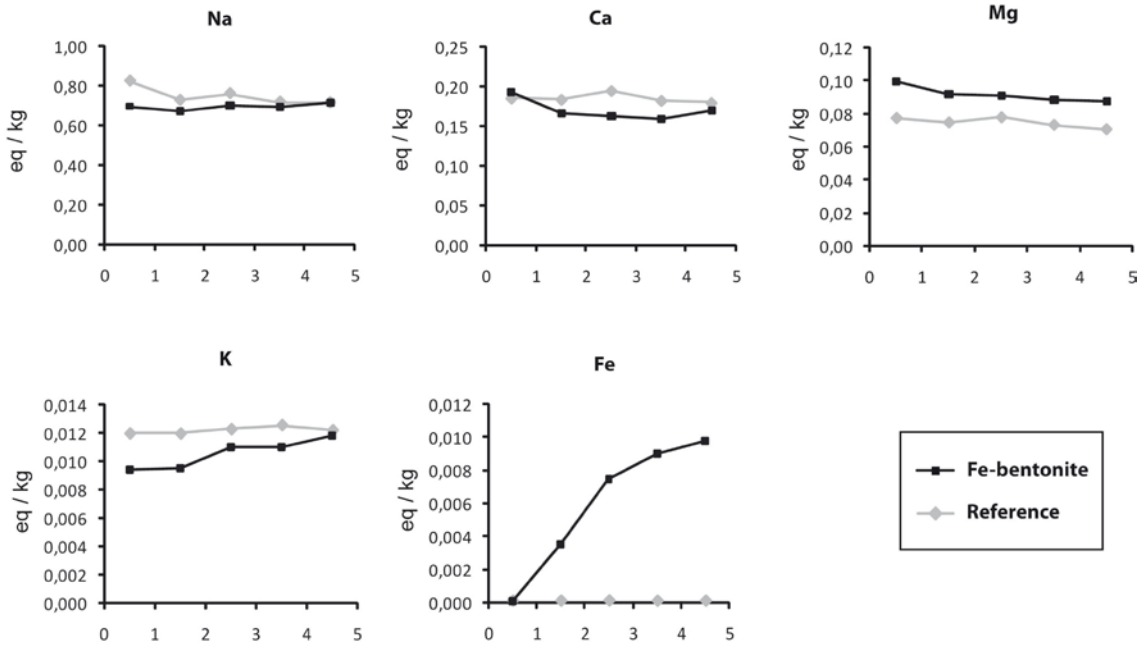

Figure 4-21. *Concentrations of extractable cations as a function of distance from steel sinter (0) towards cast iron.*

Table 4-8. Saturation (%) of exchangeable cation sites with cations, and sum of exchangeable cations expressed as charge equivalents per dry (105oC) kg of material.

Sample		Ca %	Fe %	K %	Mg %	Na %	Σ Exc.Cat. eq/kg
Reference	3a	16.87	0.01	1.09	7.06	74.97	1.10
	3b	18.42	0.01	1.20	7.51	72.86	1.00
	3c	18.65	0.01	1.17	7.46	72.70	1.05
	3d	18.50	0.01	1.27	7.45	72.77	0.99
	3e	18.39	0.01	1.25	7.25	73.11	0.98
Fe-bentonite	13a	19.27	0.01	0.94	9.97	69.82	1.00
	13b	17.60	0.38	1.00	9.71	71.30	0.95
	13c	16.63	0.77	1.13	9.33	72.14	0.98
	13d	16.47	0.94	1.14	9.14	72.31	0.97
	13e	16.96	0.99	1.19	8.81	72.06	1.00

The sum of exchangeable cations correlates with measured CEC values (Table 4-3). The amount of exchangeable cations in ammonium chloride extraction can be slightly higher than the actual value due to dissolution of remnants of porewater and possible easily dissolvable mineral phases. However, the use of ethanol instead of water as solvent should prevent dissolution of water soluble gypsum and calcite.

ICP-AES

The chemical composition of samples 6a–c, 19a–c, 20a–c and reference 29b (Figure 3-3) are shown as weight percentages in Table 4-9. These results verify the results from SEM-EDS analysis. The amount of iron increases towards the cast iron. From the iron profile of samples 19 and 20, the amount of corroded iron entering the clay and the corrosion rate is estimated (section 4.1.7). Also, the amount of Ca is increased near cast iron, which supports the fact that precipitated Ca-carbonates were found in fractures of bentonite in contact with cast iron and aragonite was observed with XRD.

The copper profile for the Fe-bentonite samples clearly indicates an increase close to the Cu vessel, with 0.09 wt% (samples 19c and 20c), 0.08% (sample 29b) and 0.12% (sample 6c), whereas the Cu levels of the other samples (6a–b, 19a–b, 20a–b) are below the quantification limits. This is consistent with the low Cu levels reported for MX-80 of 2–5 ppm Cu (e.g. Karnland et al. 2009).

From the measured Cu concentration in sample 20c the total amount of copper entering the clay can be estimated, assuming a uniform Cu concentration of 0.09 wt% in a 2.0 mm thick clay layer facing the Cu vessel. This gives a value of 9.46 mg or 1.06 mm^3 of Cu. With the surface area of the Cu vessel contacting the clay of 33.90 cm^2 (3,390 mm^2), a penetration depth of 3.12×10^{-4} mm is obtained. With a corrosion time of 8.2 yr, this leads to an average corrosion rate of 0.038 μm/a. The corresponding calculated corrosion rates for the samples 6c, 19c and 29b are 0.036 μm/a, 0.034 μm/a and 0.03 μm/a. Thus, the average corrosion rate based on the four samples is about 0.035 μm/a. Please note that this calculation omits possible precipitated corrosion products at the metal surface. From visual inspection (shiny surface) however, the amount thereof is presumably small.

TEM-EDS

Platy and foliated montmorillonite particles/aggregates with an average diameter of approximately 1 mm were observed with transmission electron microscope (Figure 4-22). The edges of the aggregates were diffuse and irregular. Electron diffraction patterns ofall studied montmorillonite particles consisted of a set of continuous rings. These ring patterns indicate that the layers of the particle are randomly placed one upon the other (turbostratic disorder of stacking). The results of d-value calculations for diffraction patterns of montmorillonite particles were 4.35–4.55 Å (strong), 2.52–2.54 Å (strong), ~1.67 Å (weak), ~1.46 Å (moderate) and ~1.28 Å (weak) (Figure 4-22). These d-values corresponded to the values measured by Carlson L et al. (2006).

Table 4-9. Chemical composition of reference and iron samples (See Figure 3-6) (Samples 6 and 19 were measured at a different time than rest of the samples; hence they have different limits of quantification (amount of Cu)).

Sample	Al (wt. %)	Ca (wt. %)	Fe (wt. %)	K (wt. %)	Mg (wt. %)	Na (wt. %)	Si (wt. %)	Ti (wt. %)	Cu (wt. %)
6a	10.5	0.832	2.80	0.521	1.46	1.75	28.3	0.095	<0.04
6b	10.4	0.796	2.80	0.413	1.44	1.75	28.6	0.093	<0.04
6c	10.1	0.732	2.72	0.445	1.39	1.79	27.8	0.093	0.12
19a	10.1	0.735	3.80	0.414	1.42	1.99	28.4	0.092	<0.04
19b	10.3	0.589	3.58	0.405	1.41	1.87	27.8	0.093	<0.04
19c	10.3	0.484	3.25	0.459	1.40	1.80	27.9	0.094	0.09
20a	8.98	0.86	3.49	0.52	1.25	1.78	26.3	0.085	<0.01
20b	9.12	0.58	3.20	0.42	1.21	1.85	26.7	0.088	<0.01
20c	9.22	0.45	2.92	0.37	1.18	1.85	27.0	0.088	0.09
Ref. 29b	9.22	0.76	2.52	0.43	1.25	1.75	27.0	0.088	0.08

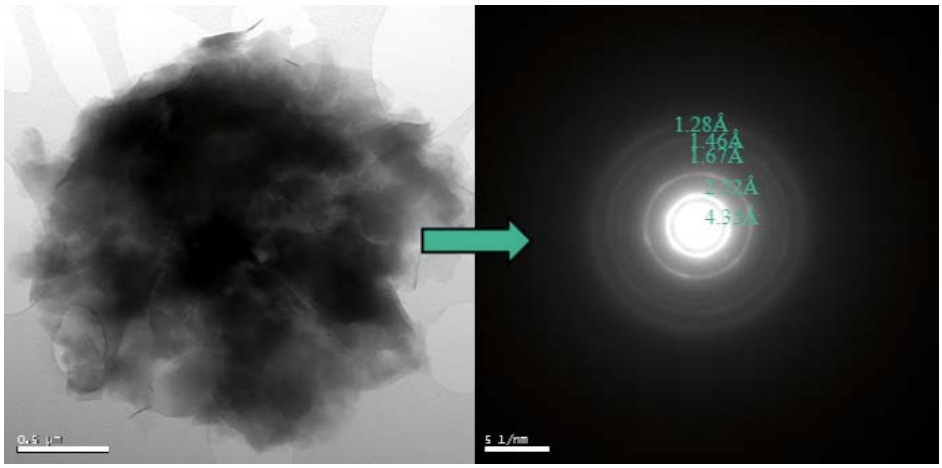

Figure 4-22. *A TEM-photo of montmorillonite particle (left) and corresponding electron diffraction pattern (right).*

Semiquantitative EDS linescan analyses were performed for 10 montmorillonite particles in sample 39a (Figure 3-3). The variation between linescans of the different particles in the same sample was considerable. One reason to these large deviations might be due to the fact, that surroundings of the examined particles contribute to the measurements, which might lead to overestimations in the amounts of some elements (e.g. Si, Al, Fe) (Carlson 2004).

The variation in iron contents in different particles of the same sample can be seen in Figure 4-23, where the linescans of four different particles are shown. These measurements indicate the presence of additional iron in some particles (e.g. in the form of an oxide coating or adsorbed Fe^{2+}). The TEM-photo of a particle, which contains a lot of iron and a photo of a particle, which contains a small amount of iron are shown in Figures 4-24 and 4-25, respectively.

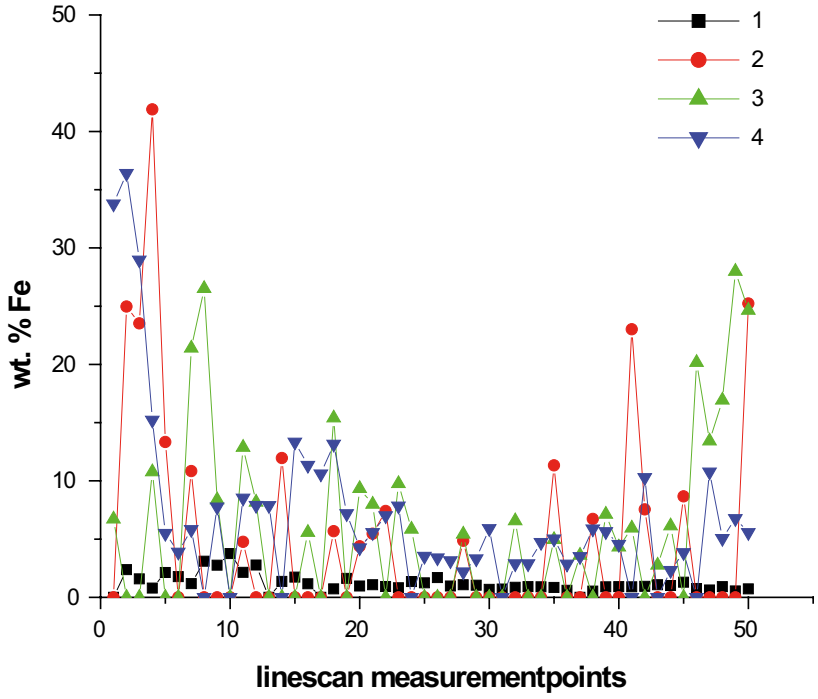

Figure 4-23. *Variation in the amount of iron in different particles/aggregates in sample 39a. A TEM-EDS-linescan was performed on 10 particles in the sample. On each linescan 50 points on a length of 200–600 nm was analysed for 1 s. Although 10 particles was analysed, for the sake of clarity the iron profiles of only four particles are shown here. Profiles, which are not shown, resemble the profile 1 in this figure.*

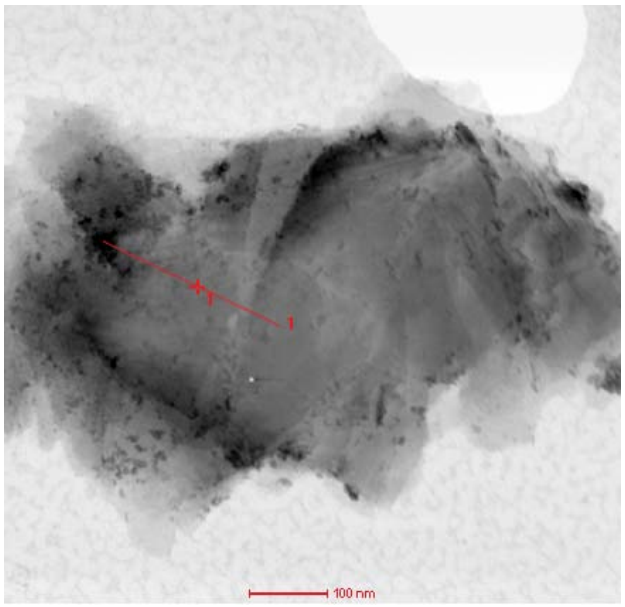

Figure 4-24. *A montmorillonite particle containing a large amount of iron (sample 39a). The place of linescan is indicated with a red line, where number 1 at the end of the red line indicates the end of the scan. The black substance has larger iron content, than the lighter parts. This is seen in the beginning of the linescan 4 in Figure 4-23.*

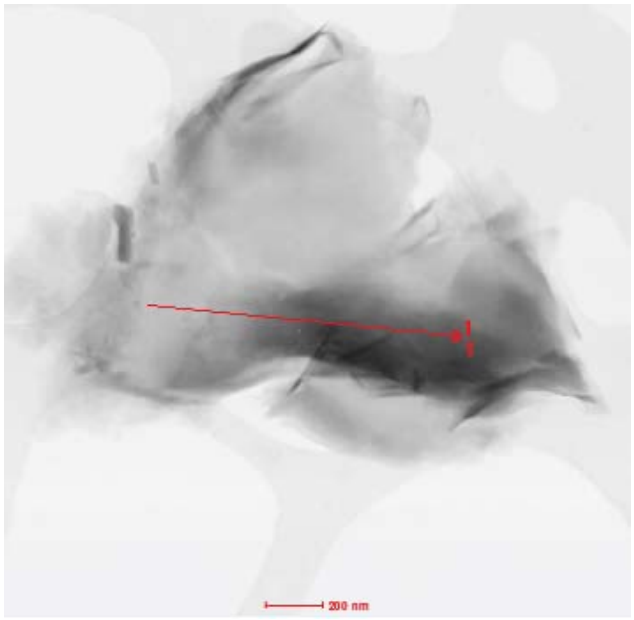

Figure 4-25. *A montmorillonite particle containing a small amount of iron (sample 39a). The place of linescan is indicated with a red line (linescan 1 in Figure 4-23).*

4.1.6 Physical properties

The gravimetric water content (mass of water per unit mass of dry sample, expressed in %) after dismantling was determined for both reference and cast/iron samples by standard method (heating at 105–110°C for 24 h). The result is shown in Table 4-10. As mentioned in Section 2.1, the initial dry densities of the MX-80/cast iron and the reference sample were prepared with different targeted dry densities of 1.69 and 1.51 g/cm^3, respectively. This difference, clearly seen in the table, is thus merely a consequence of the sample preparation.

Table 4-10. Gravimetric water contents and dry densities for MX-80/cast iron samples and their corresponding reference samples. Dry densities, ρdry, and saturated densities, ρsat, were calculated assuming a grain density of 2.75 g/cm3 for MX-80.

Sample	Water content (%)	ρ_{sat} (g/cm^3)	ρ_{dry} (g/cm^3)
First sample pair (8.2 y)			
MX-80/cast iron (sample 10, subsample 19)	15.7	2.2	1.9
Reference (sample 9, subsample 6)	24.3	2.1	1.6
Second sample pair (8.6 y)			
MX-80/cast iron (sample 15, subsample 35)	20.3	2.1	1.8
Reference (sample 12, subsample 25)	36.9	1.9	1.4

The swelling pressure of undisturbed bottom profile (see Figure 4-26 and method description in section 3.8) taken from reference MX-80 sample was 7.5 MPa (Table 4-10), which agrees well with the swelling pressure of 7.6 MPa of Wyoming MX-80 in Karnland et al. (2006), a sample compressed to a similar dry density as reference sample MX-80 in this study (1.51 g/cm^3). The swelling pressure of undisturbed bottom profile from Fe-bentonite sample was 5.2 MPa, which is lower than that of the reference sample and significantly lower than published values for MX-80 compacted to similar dry densities (1.69 g/cm^3), which are usually >10 MPa.

The results for swelling pressure of the Fe-bentonite sample was, however, similar as the Fe-bentonite sample W50ºC reported in Carlson L et al. (2006, 2007), a sample compressed to a similar dry density as Fe-bentonite sample of this study.

Hydraulic conductivity measurements were started after swelling pressure had been stabilized. The hydraulic conductivity of reference sample was similar than that of the Fe-bentonite sample (Table 4-11). The conductivity values are very low and equivalent with values for MX-80 compacted to similar dry densities.

After drying the undisturbed bottom profiles, the bentonite in Fe-bentonite sample had developed large cracks adjacent to the cast Fe (Figure 4-26) and was very easy to grind. This behaviour supports the observations during dismantling as well as SEM findings on different cracking behaviour of bentonite adjacent to cast Fe and further away from cast Fe (Figure 4-19c).

Swelling pressures and grain densities of recompacted samples were similar for reference and Fe-bentonite samples (Table 4-11). Hydraulic conductivity was slightly higher for Fe-bentonite sample than for reference sample, which is consistent with observations of Carlson et al. (2007) on increased hydraulic conductivity but no change in swelling pressure due to Fe-bentonite interaction. Hydraulic conductivities measured from recompacted samples were slightly higher than what was measured initially from undisturbed bottom profiles, but this is most probably related to the lower dry densities. Additionally, lower bottom pressure used might have had an effect. The values for swelling pressures and hydraulic conductivities were similar as reported earlier (Karnland et al. 2006, Carlson et al. 2007).

Table 4-11. Dry densities, swelling pressures, hydraulic conductivities and grain densities measured form undisturbed bottom profiles and recompacted samples.

	Undisturbed bottom profile			Mixed and recompacted sample			
	Dry D g/cm^3	SW MPa	HC m/s	Dry D g/cm^3	SW MPa	HC m/s	Grain D g/cm^3
Ref.	1.51	7.5	$2.0*10^{-14}$	1.42	4.5	$6.8*10^{-14}$	2.764
FeBe	1.69	5.2	$2.2*10^{-14}$	1.39	4.7	$8.3*10^{-14}$	2.765

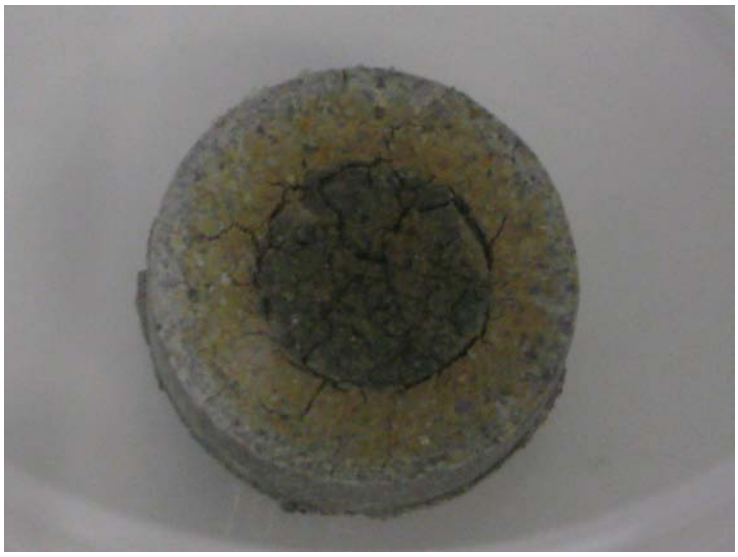

Figure 4-26. *Bottom bentonite profile of Fe-bentonite sample after the 1st swelling pressure and hydraulic conductivity measurements and drying in N_2-atmosphere.*

4.1.7 Geochemical modelling

Scope:

The objective of the modelling exercise was to simulate the chemical composition of the external solution by applying simple equilibrium-type bentonite model (Wersin et al. 2004) and the PHREEQC V2 code. The underlying concept is that diffusive equilibration between the external 0.5 M NaCl solution and the bentonite porewater occurred within the experimental time of eight years. Furthermore, for the Fe-bentonite samples a simple zero-order corrosion model, based on an estimated corrosion rate derived from Fe profiles, was included.

The details of the modelling procedures are outlined in Appendix 2. In short: The bentonite model considers cation exchange at interlayer sites and surface complexation reactions at edge sites. For the latter process, the electrostatic contribution at the charged surface was calculated with the diffuse layer model proposed by Dzombak and Morel (1990). Furthermore, dissolution of accessory minerals (halite, gypsum, calcite, quartz, siderite) according to their inventories was accounted for. No clay mineral dissolution/precipitation reactions were considered.

Modelling procedure:

The modelling exercise involved the following steps:

1) Plausibility checks of water data and estimation of corrosion rate: The water analyses of the external solutions were evaluated by mass balance consideration saturation indices of accessory minerals. An important finding of this test was (i) very similar water compositions for reference and Fe-bentonite samples, except for Eh, (ii) oversaturation with calcite (SI ≈ +0.8) and slight undersaturation with siderite (SI ≈ –0.4). These saturation indices were subsequently included in the model.
2) Modelling of reference samples: The equilibrium bentonite model was run and compared with observed data.
3) Modelling of Fe-bentonite: The same model as for the reference samples was applied, but adding the estimated zero-order corrosion rate. Various test runs with different neo-formed corrosion products were carried out, bearing in mind that spectroscopic data indicated that the Fe reacted clay occurred predominantly in the divalent state.

Results:

The calculated water and exchange composition for the reference samples is presented in Table 4-12 where also the measured data after 8.2 and 8.6 years is given. This comparison shows a good match of the observed data. It highlights that cation exchange (displacement of Ca^{2+} and Mg^{2+} by Na^{+} from the exchanger), dissolution of gypsum and calcite are the principal reactions affecting the chemistry of the external solution. The modelling results also suggest that anaerobic conditions were met in the tests and no oxidation reactions, such as pyrite oxidation occurred.

The corrosion rate for sample 19 and 20 was calculated to be 2.09 and 1.33 µm/a and thus the average corrosion rate was estimated to be 1.7 µm/a. This rate was implemented in the simulation of the Fe-bentonite external solution. Various iron oxide green rust phases (magnetite, goethite, $Fe(OH)_2$, and mixed Fe(II)/Fe(III) hydroxide phases) were tested as precipitating corrosion products. For all cases, equilibrium with siderite (SI = –0.4), as probable accessory mineral, was assumed. The results showed (Table 4-13) that observed data could be well matched when a mixed Fe(II)/Fe(III) hydroxide with a Fe(II)/Fe(III) ratio of 2 was assumed as corrosion product, whereas the assumption of pure Fe(II) hydroxide or of iron oxides with lower Fe(II)/Fe(III) ratio (e.g. magnetite) resulted in too high pH and too high dissolved Fe concentrations.

Table 4-12. Comparison between measured data for reference samples and modelled data.

	Ref sample 8.2 years	Ref sample 8.6 years	Model
pe	–3.56	–3.56	–3.71
pH	8.2	8.0	7.97
Alkalinity	2.3	3.5	2.54
Ionic strength	501	614	520
Na, mM	478.5	543.7	456.6
Ca, mM	12.5	13.0	18.4
Mg, mM	6.7	7.8	4.1
K,mM	2.5	2.2	1.6
Fe^{2+}, mM	3.58E–04	3.04E–03*	4.53E–03
Fe^{3+}, mM	6.93E–02	–	3.8E–12
Cl, mM	419.8	573.0	484.1
HCO_3^-, mM	1.67	2.65	1.95
SO_4^{2-}, mM	12.8	12.5	8.28
NaX (% eq. fraction)	72.8		88.3
CaX_2 (")	18.5		8.7
KX (")	1.3		1.1
MgX_2 (")	7.4		1.9
FeX_2 (")	0.01		0.007

Table 4-13. Comparison between measured data for Fe-bentonite samples and modelled data

	Fe sample 8.2 years	Fe sample 8.6 years	Fe model green rust eq.
pe	–8.27	–8.27	–8.93
pH	8.0	8.0	7.95
Alkalinity mmol/L	4.2	2.9	3.7
Ionic strength M	527	605	520
Na, mM	456.7	526.3	469.3
Ca, mM	14.4	14.5	12.9
Mg, mM	9.8	11.1	4.2
K,mM	1.5	1.5	1.5
Fe^{2+}, mM	5.4E–04	4.3E–03	3.2E–03
Fe^{3+}, mM	7.2E–04	2.7E–03	1.4E–14
Cl, mM	479.8	561.7	484.3
HCO_3^-, mM	3.20	2.17	2.9
SO_4^{2-}, mM	10.1	10.4	8.4
NaX (% eq. fraction)	72.1		90.9
CaX_2 (")	16.6		6.1
KX (")	1.1		1.1
MgX_2 (")	9.3		1.9
FeX_2 (")	0.77		0.005

4.2 JAEA's samples

4.2.1 Solution chemistry

The solutions in the JAEA samples were separated either by centrifugation (samples 62 and 63) or by squeezing (samples 65 and 68). The solutions were thereafter analysed in the same manner as those in the VTT samples. The results are shown in Table 4-14.

Briefly, all the solutions in the JAEA samples exhibited high pH values (from 11.1 to 12.7) and clearly reducing conditions. Sodium was the dominating cation, while chloride and sulphate ions were the dominating anions.

The Eh and pH values measured at VTT agree well with those obtained at JAEA. Thus, the Eh values reported in Appendix 1 for the samples 62 and 63 were –583 and –639 mV, according to the JAEA-study. The corresponding Eh-values in the VTT-study were about –445 mV and roughly –584/–614 mV, respectively. In case of the pH measurements, the agreement between the two studies was even better; the pH values in samples 62 and 63 were reported to be 12.7 and 13.0 in the JAEA study, while the corresponding values in this VTT study were 12.7 and 12.8, respectively. The agreement between the Eh and pH data is satisfactory from practical points of view.

4.2.2 CEC

The CEC values of the JAEA samples were determined for the original sample and in three subsamples as described in section 3.5.2. Table 4-15 shows the results. The heavy fraction, which contained the iron that had been added during the initial preparation of the samples, exhibits a clearly higher CEC than the corresponding 'as delivered' sample, which suggests that the iron particles contribute the measured CEC.

The light fraction consisted essentially of Kunipia F bentonite and possibly also a minor fraction of iron particles. The effect of purifying this fraction in order to remove iron, is seen by comparing the rows with data for the 'light fraction' with the data for the 'purified light fraction'. In doing so, one finds that the purification leads to higher CEC values in three cases (samples 63, 65, and 68), while one sample (sample 62) exhibits a slightly decreased CEC. A comparison between the measurements performed at VTT on "as delivered" samples and those made at JAEA on bentonite/iron samples indicates a relatively poor correlation between the data. However, the small number of CEC values in Table 4-13 does not allow of any further analyses of the results.

Table 4-14. Results from analyses of the solutions in the JAEA samples after delivery to VTT from JAEA. All concentrations are given in mg/L. Alkalinity is given in mmol/L.

	62	63	65	68	Method
pH	12.7	12.8	12.6	11.1	Orion pH-el.
Eh (mV)	-446_{Pt}	-584_{Pt}	-565_{Pt}	-250_{Pt}	Pt vs. LF-2
	-443_{Au}	-614_{Au}	-611_{Au}	-250_{Au}	Au vs. LF-2
EC (mS/cm)	0.14	0.11	–	13.1	Yokogawa SC82
Na	10,700	19,300	6,200	3,900	ICP-AES
Mg	<0.05	<0.05	<0.1	<0.5	ICP-AES
Ca	0.94	0.81	1.5	16	ICP-AES
Si	6.0	3.7	14	14	ICP-AES
Al	<0.5	<0.5	<1	<5	ICP-AES
K	84	84	92	150	FAAS
Fe_{tot}	0.14	0.35	0.13	<0.2	ICP-AES
Fe_{tot}	0.11	0.35	0.12	0.02	Colorimetry
Fe^{2+}	0.05	0.10	0.04	0.01	Colorimetry
Fe^{3+}	0.06	0.25	0.08	0.01	Colorimetry
Cl^-	12,200	24,300	160	210	IC
SO_4^{2-}	460	480	240	8,000	IC
Alk	80	135	245	4	Titration

Table 4-15. Results from VTT's analyses showing measured CEC (meq/g) in a) untreated JAEA samples, b) light fractions obtained by centrifugation, c) heavy fraction obtained by centrifugation, and d) a purified light fraction. The last row in the table shows corresponding values measured at JAEA (see Appendix 1 for details).

Sample/subsample	JAEA sample numbers				
	61	62	63	65	68
As delivered	0.836	0.712	0.458	1.986	0.714
Light fraction	–	0.988	0.652	0.590	0.847
Purified light fraction	–	0.936	1.758	0.725	0.968
Heavy fraction	–	1.411	0.669	>2.422	>3.433
Results by JAEA	0.648	0.261	–	0.373	0.591

4.2.3 Mineralogy

XRD

Mineralogical analyses of the bulk fractions of JAEA samples showed the presence of iron powder in all samples (Figure 4-27). From the Fe powder reaction products, sample 61 contained magnetite, and sample 68, pyrite. Green rust could not be observed in any of the samples. Despite the fact that samples were washed with pure ethanol before drying, samples 62 and 63 contained halite. The position of d(060) line of clay minerals was at d-value of 1.492–1.493 Å in all JAEA samples, which suggests to the presence of dioctahedral clay minerals) instead of trioctahedral clay minerals.

Based on comparison of N_2-atmosphere-dried (Figure 4-28) and ethylene glycol treated sample patterns, the clay fraction consisted of smectite in samples 61 and 68. d(001) line of samples 61 and 68 at approximate d-value of 14 Å moved to 16 Å. Sample 65 contained some smectite, showing up as a small bump in the N_2-atmosphere-dried sample at 14 Å, which moved to 16 Å after glycol treatment. In samples 62 and 63 smectite was no more present or they contained only very small amounts of smectite, which did not show up in XRD analysis, since peaks did not react to the glycol treatment. The position of peaks in clay fraction in samples 62, 63 and 65 suggested that they consisted presumably of kaolinite and/or chlorite.

All sample mounts kept their initial greenish colour during the XRD analyses.

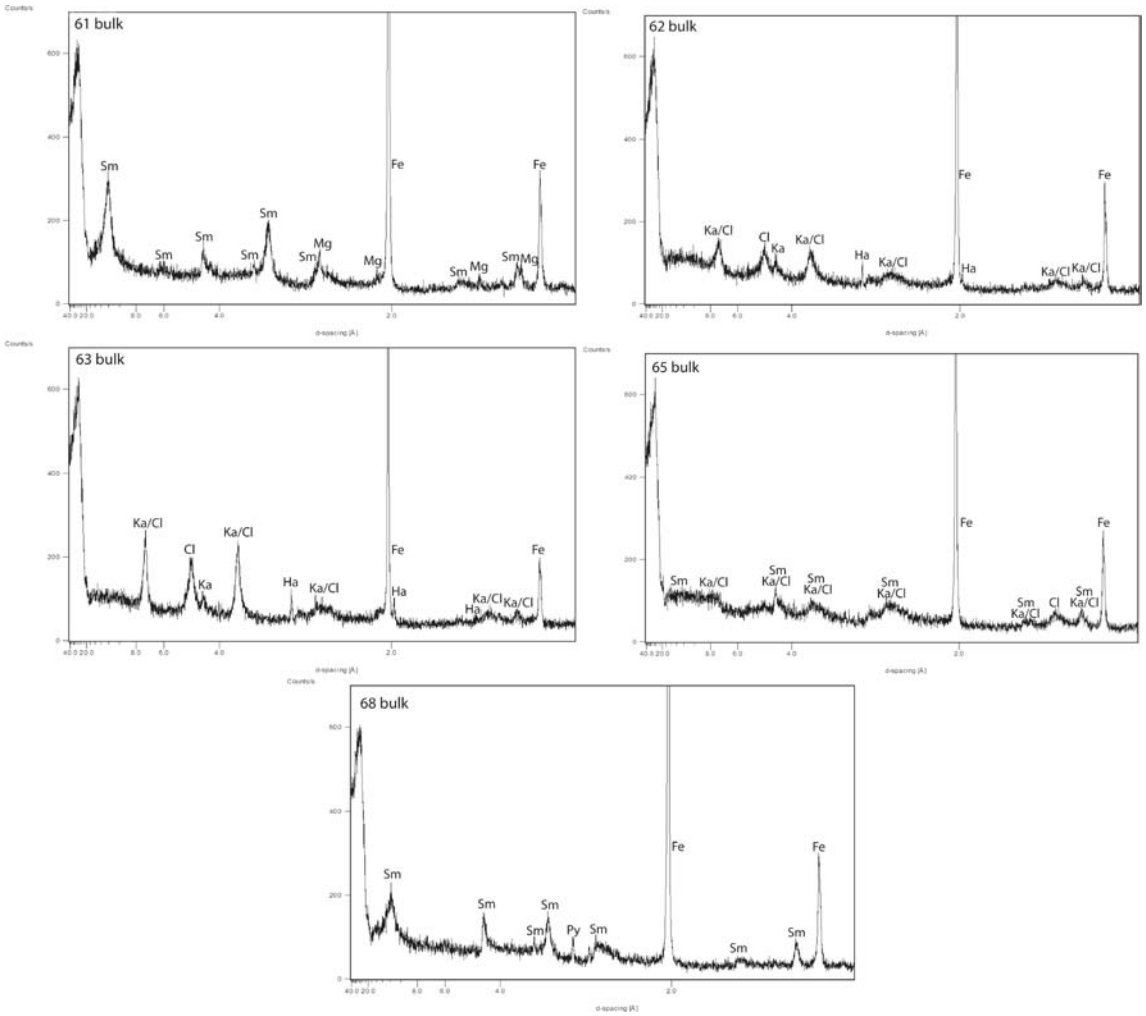

Figure 4-27. *XRD-patterns of 10 y old JAEA samples randomly oriented bulk fractions. Minerals identified are marked: Sm = smectite, Fe = iron powder, Ka = kaolin, Cl = chlorite, Mg = magnetite, Py = pyrite, Ha = halite.*

FTIR

FTIR pellets were all initially greenish in colour, but after drying in 150ºC for 20 h turned to reddish brown indicating oxidation of iron during drying in oxidative conditions. FTIR patterns (intensity and band positions) of wet/anoxidized and dry/oxidized samples were more or less similar except for water hydration bands at approximately 3,400 cm^{-1} and 1,630 cm^{-1}. However, in samples 61 and 68 wet/ anoxidized samples the transmissivity at 800–625 cm^{-1} region was lower than in dry/ oxidized sample.

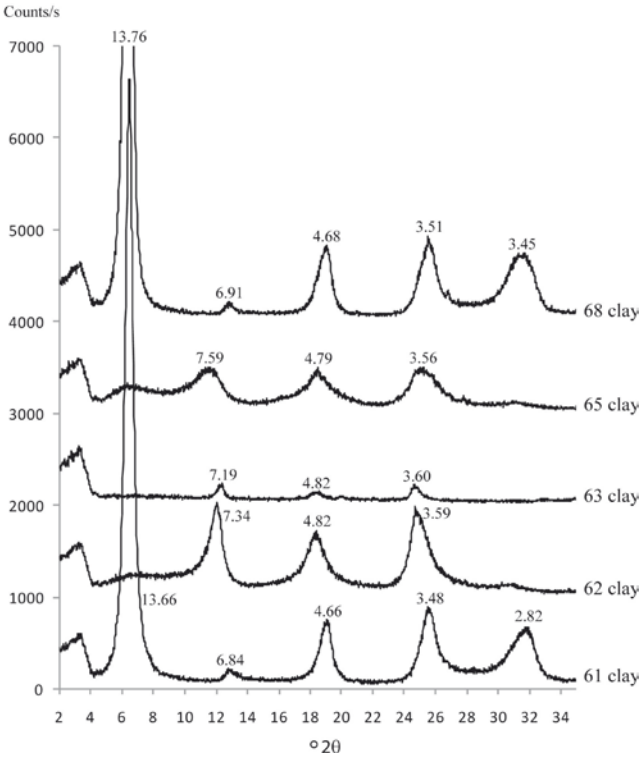

Figure 4-28. *XRD patterns of oriented N_2-atmosphere-dried clay fractions of 10 y old JAEA samples. Positions of main peaks as d-values (Å) are marked.*

Based on FTIR-patterns (Figure 4-29), none of the JAEA samples showed indication of presence of kaolin group minerals or chlorite. Samples 62, 63 and 65, which were proven in XRD-analysis to be fully or partly transformed to non-swelling 7 Å minerals, showed some changes in their FTIR-patterns: a) decrease in 3,634 cm^{-1} OH-stretching band position (to 3,620 cm^{-1}), b) decrease in intensity of 1,630 cm^{-1} hydration water band, c) increase in intensity of 1,089 cm^{-1} Si-O band, d) decrease in intensity of 915 cm^{-1} AlAlOH deformation band, e) disappearance of small $AlFe^{3+}OH$ bending, f) increase in intensity of 845 cm^{-1} $AlMgOH/AlFe^{2+}OH$ stretching, g) decrease in transmissitivity at 800–625 cm^{-1} region, and h) appearance of 580 cm^{-1} bending. Such changes can be assigned to a) change in composition of hydroxyl-bound cations towards Mg or Fe or development of pyrophyllite or mica-type of AlAlOH bondings b) decrease in interlayer-bound water, c) increase in tetrahedral silica, d) decrease in octahedral Al, e) reduction of octahedral Fe^{3+} in $AlFe^{3+}OH$, f) possible increase in octahedral Fe, and g) increase in $MgFe^{3+}OH$, respectively. Thus, FTIR-analyses complemented the interpretation on XRD-analyses that samples 62, 63 and 65 had transformed at least partly to serpentine group mineral, most likely to berthierine $(Fe^{2+},Fe^{3+}Al,Mg)_{2-3}(Si,Al)_2O_5(OH)_4$.

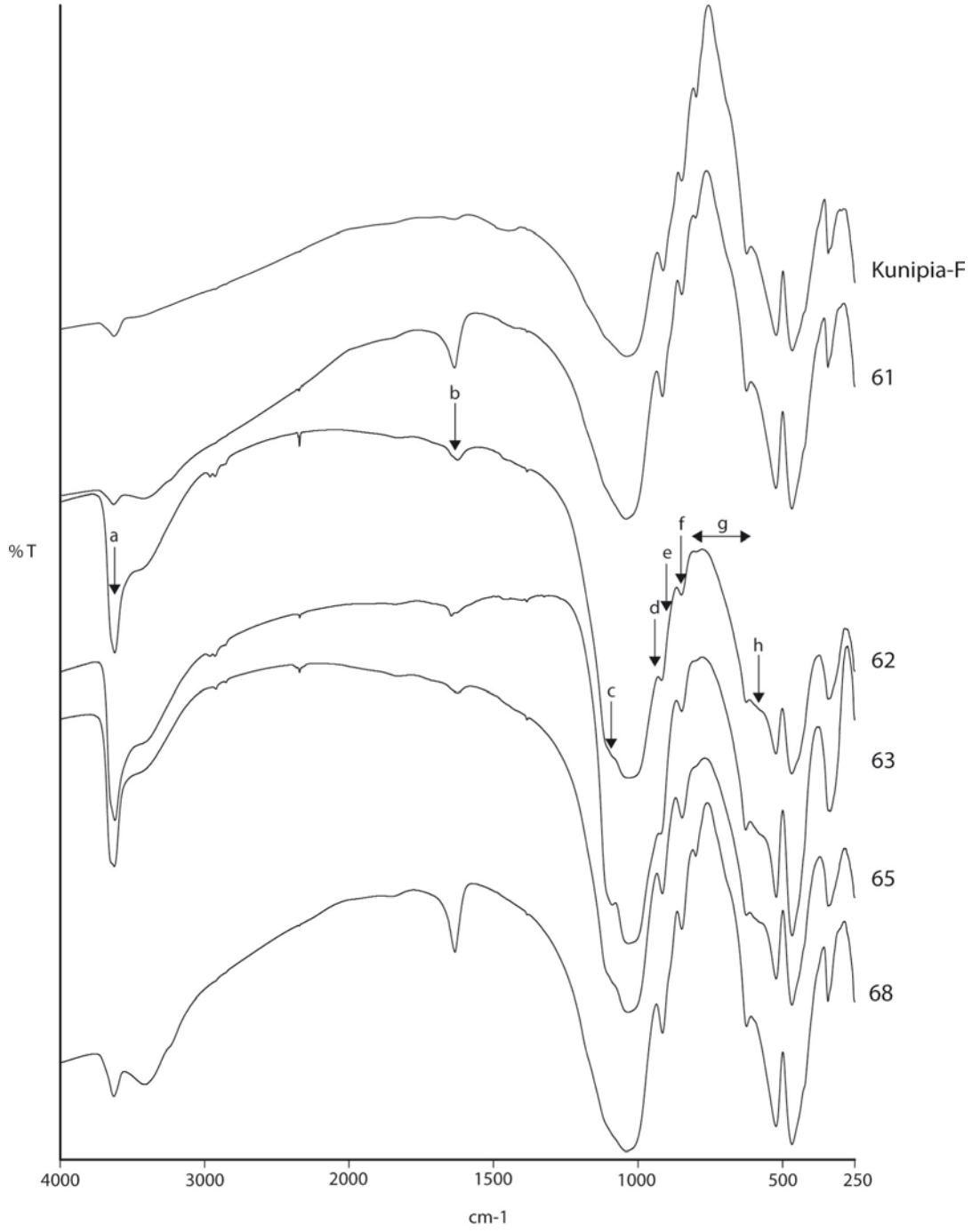

Figure 4-29. *FTIR-patterns of clay fractions of initial Kunipia-F and of JAEA's 10 y old Fe-bentonite samples. Arrows indicate detected changes and are described sequentially from left to right in the text.*

5 Summary

A brown iron diffusion front in bentonite extending to 7–8 mm distance from cast iron was observed in the VTT samples after 8.2–8.6 years. The major changes in the external solutions (initially 0.5 M NaCl) were increasing concentrations of Mg, Ca, and SO_4, and an increasing alkalinity. The pH was still around 8, whereas the redox-conditions after 8.6 years were clearly reducing, both measured in the external solution and in the porewater for the reference sample and the iron-clay test sample. The gas phase contained H_2, which, most probably, was caused by corrosion of the cast iron cylinders, and CO_2, as a result of, e.g., calcite dissolution.

The batch tests at JAEA differed with regard to the initial solution chemistry, which was either distilled water, 0.3 M NaCl, 0.6 M NaCl, 0.1 M $NaHCO_3$, or 0.05 M Na_2SO_4 and also with respect to the much larger amount of iron (surface area of iron) in contact with bentonite as compared to VTT tests. After the 10 years batch tests the water exhibited pH values in the approximate range of 11 to 13, and clearly reducing conditions with Eh values between –260 and –580 mV.

The bentonite in the diffusion based VTT test samples was divided into subsamples, which were studied with XRD, FTIR, SEM, ICP-AES, TEM-EDS, XANES, Mössbauer spectroscopy, and wet-chemical methods. The bentonite in the JAEA batch samples were analysed by XRD and FTIR, and wet-chemical methods.

No indication of major changes in mineralogy of MX-80 bentonite was seen in the diffusion based iron-clay interaction tests. Minor traces of unidentified crystalline compounds were detected that possibly were newly formed. In the close vicinity of the cast iron additional calcite, aragonite and hematite was observed. Tiny changes in XRD peak positions suggest that fraction of illite might have increased and swelling ability of montmorillonite decreased due to the iron interaction process. Based on FTIR, iron seems to have been incorporated, to some extent, in the montmorillonite structure, and silica released. Increase in exchangeable iron in bentonite occurred towards cast iron. One explanation for the increased amount of exchangeable iron is by replacement of magnesium, but the dissolution of poorly crystalline Fe^{2+} phases during extraction cannot be excluded either. The sum of exchangeable cations was consistent with measured CEC's. The highest CEC values for the test samples were found in the section closest to the iron cylinder. The results indicate a decrease in CEC with increasing distance from the cast iron. However, more data are needed in order to determine with reasonable confidence whether CEC increased in the vicinity of the cast iron. Increase in Fe content and decrease in Si content of bentonite towards cast iron was observed in semiquantitative analysis by SEM-EDS and also in chemical composition analysis by ICP-AES.

The corroded iron was predominantly in the divalent form, and its concentration was highest close to the cylinder and decreased strongly with increasing distance from its surface. Mössbauer spectroscopy results indicate that the amount of Fe^{3+} remains constant and only the amount of Fe^{2+} is increasing in the samples, which contained cast iron. This implies that the change in the proportion of Fe^{2+} could be due to the fact that most of the iron leaching into the bentonite was divalent, not due to reduction of octahedral Fe^{3+} in the montmorillonite unit layers. Also the results from the XANES measurements indicate that the iron-bentonite sample had a higher Fe^{II}/Fe^{III} ratio compared to the reference clay. At least a small amount of the Fe^{II} seemed to oxidize upon exposure to oxygen in the ambient atmosphere.

The swelling pressure and the hydraulic conductivity were measured in undisturbed subsamples of the MX-80. The iron-bentonite interaction seemed to slightly decrease the swelling pressure, while the hydraulic conductivity was unchanged. These were re-analysed after mixing and recompaction of samples and in this case no clear differences between reference sample and Fe-reacted sample in swelling pressure and hydraulic conductivity was found. Initially found small decrease in swelling pressure could have been caused by cementation. Observations from dismantling and after drying procedures as well as SEM results suggest that in the close vicinity of cast iron, bentonite had been cemented to some extent.

Much stronger impact on the bentonite was seen in the JAEA batch tests with a higher iron to clay ratio and higher pH. Montmorillonite had transformed to a non-swelling 7 Å clay mineral in samples stored in 0.3–0.6 M chloride solutions (samples 62 and 63) and partly in sample stored in 0.1 M bicarbonate solution (sample 65). These samples were exhibiting the highest pH-values of the test samples. Based on XRD and FTIR determinations 7 Å non-swelling clay phase formed was most likely a serpentine mineral, berthierine. Silica was released during the mineral transformation. The clay phase in samples kept in distilled water (sample 61) and in 0.05 M sulphate solution (sample 68) was montmorillonite, and contained, in addition to montmorillonite, magnetite and pyrite, respectively.

The CEC values of the JAEA samples were determined for the original sample and in three subsamples. The heavy fraction, which contained the iron that had been added during the initial preparation of the samples, exhibited a clearly higher CEC than the corresponding 'as delivered' JAEA sample. This suggests that the iron particles contribute the measured CEC. Iron removal from the light fraction (Kunipia F) resulted in three cases in increased CEC, but in one case in a minor decrease. The small number of data does not allow of any detailed analyses of the measured CEC data.

As a conclusion the montmorillonite component in the MX-80 bentonite after eight years of diffusion base iron-bentonite interaction, is still unchanged. Although some indications of changes were found in the bentonite as a whole (e.g., with regard to CEC), there were no clear evidence of montmorillonite transformation to a non-swelling mineral. On the other hand the more extreme conditions (high Fe/clay ratio, high pH) in the batch tests resulted in the mineral transformation into a non-swelling clay mineral. The two batch test cases with NaCl concentrations 0.3 and 0.6 M vs. 0.5 M in diffusion based tests, respectively were however rather similar, except for the considerably higher pH value and the iron surface exposed to the bentonite in the batch tests. Of these two factors, pH may be regarded to be the one that had most impact on the obtained results. The pH in the batch tests was about 12.7, which is much higher than the pH 8 in the diffusion based test.

Geochemical modelling of the VTT samples using an equilibrium approach indicated that diffusive equilibration between the external solution and the bentonite porewater had occurred. The composition of the water could be adequately simulated and highlighted that dissolution of gypsum and calcite and cation and proton exchange at the clay surfaces were the main reactions affecting the solution chemistry in the reference as well as in the Fe-bentonite samples. The average corrosion rate estimated from Fe profiles in the Fe-reacted samples is about 1.7 μm/a. The modelling data suggest the formation of a green rust phase (Fe(II)/Fe(III) ratio of ~2) from the corrosion process, which is in line with spectroscopic observations.

The corrosion rate of the Cu vessel surface was estimated from the Cu analysis in the clay to be about 0.035 μm/a.

References

SKB's (Svensk Kärnbränslehantering AB) publications can be found at www.skb.se/publications.

Aalto H, Carlsson T, Kumpulainen H, Lehikoinen J, Muurinen A, 2002. Chemical interactions in the near-field of a spent fuel repository – preliminary results from a long-term laboratory experiment. In: McGrail B P, Cragnolino G A (eds). Scientific basis for nuclear waste management XXV: symposium held in Boston, Massachusetts, 26–29 November 2001. Warrendale, PA: Materials Research Society. (Materials Research Society Symposium Proceedings 713), pp 129–133.

Anttila P, Autio J, Berghäll J, Börgesson L, Eriksson M, Hagros A, Halvarsson B, Johansson E, Kotola R, Parkkinen I, Rönnqvist P-E,Sandén T, 2008. KBS-3H design description 2007. Posiva 2008-01, Posiva Oy, Finland.

Appelo C A J, Wersin P, 2007. Multicomponent diffusion modeling in clay systems with application to the diffusion of tritium, iodide and sodium in Opalinus Clay. Environmental Science & Technology, 41, pp 5002–5007.

Bourrié G, Trolard F, Génin J M R, Jaffrezic A, Maître V, Abdelmoula M, 1999. Iron control by equilibria between hydroxy-Green Rusts and solutions in hydromorphic soils. Geochimica et Cosmochimica Acta, 63, pp 3417–3427.

Bradbury M H, Baeyens B, 1997. A mechanistic description of Ni and Zn sorption on Na-montmorillonite. Part II: modelling. Journal of Contaminant Hydrology, 27, pp 223–248.

Bradbury M H, Baeyens B, 2002. Porewater chemistry in compacted re-saturated MX-80 bentonite: physico-chemical characterisation and geochemical modelling. Nagra Technical Report NTB 01-08, National Cooperative for the Disposal of Radioactive Waste, Switzerland.

Brindley G W, Brown G (eds), 1980. Crystal structures of clay minerals and their X-ray identification. London: Mineralogical Society. (Mineralogical Society Monograph 5)

Carlson L, 2004. Bentonite mineralogy. Part 1: Methods of investigation – a literature review. Part 2: Mineralogical research of selected bentonites. Posiva Working Report 2004-02. Posiva Oy, Finland.

Carlson L, Karnland O, Olsson S, Rance A, Smart N, 2006. Experimental studies on the interactions between anaerobically corroding iron and bentonite. Posiva Working Report 2006-60, Posiva Oy, Finland. (Also published as SKB R-08-28, Svensk Kärnbränslehantering AB.)

Carlson L, Karnland O, Oversby V M, Rance A P, Smart N R, Snellman M, Vähänen M, Werme L O, 2007. Experimental studies of the interactions between anaerobically corroding iron and bentonite. Physics and Chemistry of the Earth, Parts A/B/C, 32, pp 334–345.

Carlson S, Clausén M, Gridneva L, Sommarin B, Svensson C, 2006. XAFS experiments at beamline I811, MAX-lab synchrotron source, Sweden. Journal of Synchrotron Radiation, 13, pp 359–364.

Curti E, Wersin P, 2002. Assessment of porewater chemistry in the bentonite backfill for the Swiss SF/HLW repository. Nagra Technical Report NTB 02-09, National Cooperative for the Disposal of Radioactive Waste, Switzerland.

Dzombak D A, Morel F M M, 1990. Surface complexation modeling: hydrous ferric oxide. New York: Wiley.

Gaucher E C, Tournassat C, Pearson F J, Blanc P, Crouzet C, Lerouge C, Altmann S, 2009. A robust model for pore-water chemistry of clayrock. Geochimica et Cosmochimica Acta, 73, pp 6470–6487.

Hellmuth K H, Siitari-Kauppi M, Lindberg A, 1993. Study of porosity and migration pathways in crystalline rock by impregnation with ^{14}C-polymethylmethacrylate. Journal of Contaminant Hydrology, 13, pp 403–418.

Hellmuth K H, Lukkarinen S, Siitari-Kauppi M, 1994. Rock matrix studies with carbon-14-polymethylmethacrylate (PMMA): method development and applications. Isotopenpraxis Isotopes in Environmental and Health Studies, 30, pp 47–60.

Ishidera T, Ueno K, Kurosawa S, Suyama T, 2008. Investigation of montmorillonite alteration and form of iron corrosion products in compacted bentonite in contact with carbon steel for ten years. Physics and Chemistry of the Earth, 33, pp S269–S275.

Ito M, Okamoto M, Shibata M, Sasaki Y, Danbara T, Suzuki K, Watanabe T, 1993. Mineral composition analysis of bentonite. PNC TN8430 93-003, Power Reactor and Nuclear Fuel Development Corporation. (In Japanese with English abstract.)

Kamei G, Oda C, Mitsui S, Shibata M, Shinozaki T, 1999. Fe(II)-Na ion exchange at interlayers of smectite: adsorption-desorption experiments and a natural analogue. Engineering Geology, 54, pp 15–20.

Karnland O, Olsson S, Nilsson U, 2006. Mineralogy and sealing properties of various bentonites and smectite-rich clay materials. SKB TR-06-30, Svensk Kärnbränslehantering AB.

Karnland O, Olsson S, Dueck A, Birgersson M, Nilsson U, Hernan-Håkansson T, 2009. Mineralogy and chemical composition. In: Long term test of buffer material at the Äspö Hard Rock Laboratory, LOT project. Final report on the A2 test parcel. SKB TR-09-29, Svensk Kärnbränslehantering AB, pp 61–112.

Kumpulainen H, Muurinen A, 2001. Raudan reaktiot käytetyn ydinpolttoaineen loppusijoitusolosuhteissa. VTT Research Notes 2122, VTT Kemiantekniikka, Finland. (In Finnish.)

Lantenois S, Plancon A, Jullien M, Muller F, Bauer A, Lanson B, 2003. Iron-smectites interactions in aqueous solution: a quantitative approach. In : Euroclay 2003. 10th Conference of the European Clay Groups Association, Modene, Italy, 22–26 June 2003.

Lear P R, Stucki J W, 1989. Effects of iron oxidation state on the specific surface area of nontronite. Clays and Clay Minerals, 37, pp 547–552.

Lewis D G, 1997. Factors influencing the stability and properties of green rusts. In: Auerswald K, Stanjek H, Bigham J M (eds). Soils and environment: soil processes from mineral to landscape scale. Reiskirchen: Catena-Verlag. (Advances in Geoecology 30), pp 345–372.

Mammen C B, Ursby T, Cerenius Y, Thunnissen M, Als-Nielsen J, Larsen S, Liljas A, 2002. Design of a 5-station macromolecular crystallography beamline at MAX-lab. Acta Physica Polonica A, 101, 595–602.

Mammen C B, Ursby T, Thunnissen M, Als-Nielsen J, 2004. Bent diamond crystals and multi-layer based optics at the new 5-station protein crystallography beamline 'Cassiopeia' at MAX-lab. AIP Conference Proceedings, 705, pp 808–811.

Marcos N, 2003. Bentonite-iron interactions in natural occurrences and in laboratory – the effects of the interaction on the properties of bentonite: a literature survey. Posiva Working Report 2003-55, Posiva Oy, Finland.

Marcos N, 2004. Results of the studies on bentonite samples from Serrata de Nijar, Almería, Spain. Posiva Working Report 2004-24. Posiva Oy, Finland.

Meier L P, Kahr G, 1999. Determination of the cation exchange capacity (CEC) of clay minerals using the complexes of copper(II) ion with triethylenetetramine and tetraethylenepentamine. Clays and Clay Minerals, 47, pp 386–388.

Milodowski A E, Cave M R, Kemp S J, Taylor H, Vickers B P, Green K A, Williams C L, Shaw R A, 2009. Mineralogical investigations of the interaction between iron corrosion products and bentonite from the NF-PRO experiments (Phase 1). SKB TR-09-02, Svensk Kärnbränslehantering AB.

Moore D M, Reynolds R C, 1989. X-ray diffraction and the identification and analysis of clay minerals. Oxford: Oxford University Press.

Moore D M, Reynolds R C, 1997. X-ray diffraction and the identification and analysis of clay minerals. 2nd ed. Oxford: Oxford University Press.

Muurinen A, Carlsson T, 2008. Eh and pH in compacted MX-80 bentonite. Posiva Working Report 2008-48. Posiva Oy, Finland.

Müller-Vonmoos M, Kahr G, 1983. Mineralogische Untersuchungen von Wyoming Bentonit MX-80 und Montigel. Nagra Technicher Bericht NTB 83-12, National Cooperative for the Disposal of Radioactive Waste, Switzerland. (In German.)

Ochs M, Lothenbach B, Shibata M, Yui M, 1999. Bentonite porewater chemistry. JNC TN8400 99-075, Japan Atomic Eneregy Agency.

Otake T, Wesolowski D J, Anovitz L M, Allard L F, Ohmoto H, 2007. Experimental evidence for non-redox transformations between magnetite and hematite under H_2-rich hydrothermal conditions. Earth and Planetary Science Letters, 257, pp 60–70.

SKB, 2001. Forsknings-, utvecklings- och demonstrationsprogram för ett KBS-3 förvar med horisontell deponering. SKB R-01-55, Svensk Kärnbränslehantering AB. (In Swedish.)

Smart N R, Blackwood D J, Werme L, 2001. The anaerobic corrosion of carbon steel and cast iron in artificial groundwaters. SKB TR-01-22, Svensk Kärnbränslehantering AB.

Smart N R, Rance A P, Werme L O, 2004. Anaerobic corrosion of steel in bentonite. In: Oversby V M, Werme L O (eds). Scientific basis for nuclear waste management XXVII: symposium held in Kalmar, Sweden, 15–19 June 2003. Warrendale, PA: Materials Research Society. (Materials Research Society Symposium Proceedings 807), pp 441–446.

Stucki J W, 1997. Redox processes in smectites: soil environmental significance. In: Auerswald K, Stanjek H, Bigham J M (eds). Soils and environment: soil processes from mineral to landscape scale. Reiskirchen: Catena-Verlag. (Advances in Geoecology 30), pp 395–406.

Svensson D, 2009. Experiments with smectite resolved in time and space by synchrotron X-ray diffraction. Lic. thesis. Division of Polymer & Materials Chemistry, Lund University.

Taniguchi N, Kawasaki M, Naito M, 2008. Experimental study on corrosion behavior of carbon steel in buffer material, 2: analysis of corrosion products on coupons immersed for 10 year duration. JAEA-Research 2008-108, Japan Atomic Energy Agency. (In Japanese with English abstract.)

Tributh H, Lagaly G A, 1986. Aufbereitung und Identifizierung von Boden- und Lagerstättentonen. I. Aufbereitung der Proben im Labor. GIT-Fachzeitschrift für das Laboratorium, 30, pp 524–529. (In German.)

Wersin P, Snellman M, 2007. Impact of iron on the performance of clay barriers in waste disposal systems. Report on the status of research and development. Posiva Working Report 2008-07, Posiva Oy, Finland.

Wersin P, Curti E, Appelo C A J, 2004. Modelling bentonite–water interactions at high solid/liquid ratios: swelling and diffuse double layer effects. Applied Clay Science, 26, pp 249–257.

Wersin P, Birgersson M, Olsson S, Karnland O, Snellman M, 2007. Impact of corrosion-derived iron on the bentonite buffer within the KBS-3H disposal concept – the Olkiluoto site as case study. Posiva 2007-11, Posiva Oy, Finland.

Wieland E, Wanner H, Albinsson Y, Wersin P, Karnland O, 1994. A surface chemical model of the bentonite-water interface and its implications for modelling the near field chemistry in a repository for spent fuel. SKB TR 94-26, Svensk Kärnbränslehantering AB.

Xia X, Idemitsu K, Arima T, Inagi Y, Ishidera T, Kurosawa S, Iijima K, Sato H, 2005. Corrosion of carbon steel in compacted bentonite and its effect on neptunium diffusion under reducing condition. Applied Clay Science, 28, pp 89–100.

Appendix 1

Background Information for JAEA's Samples of Long-term Bentonite-iron Interaction Experiments

H. Sasamoto* & M. Yui*

*Japan Atomic Energy Agency (JAEA)

Introduction

Long-term experiments for bentonite-iron interactions were initially conducted to investigate the corrosion behavior of carbon steel under different anions concentrations (i.e., Cl^-, HCO_3^- and SO_4^{2-}). Results of JAEA experiments to investigate the corrosion behavior of carbon steel in compacted bentonite and bentonite itself have already been reported (e.g., Taniguchi et al. 2008, Ishidera et al. 2008).

Residual samples after *batch-type* experiments were not analyzed and supplied to investigate the alteration behavior of the clay mineral (montmorillonite) because recent several studies showed the very high reactivity of the iron-clay system and demonstrated the transformation to iron-rich 7 Å phases like berthierine, cronstedtite or odinite (e.g., Lantenois et al. 2003).

This memorandum presents some background information of JAEA's samples which have been sent to B+Tech in the middle of February 2009.

Starting material and experimental procedure

Iron material

5 micro-meter powder metallic iron was used as a starting iron material. This small grain size was used in order to enhance the reactivity because of its higher surface area (0.33 m^2/g). It is almost 99.5 wt% pure iron powder produced by Mitsuwa Chemical Co. Ltd, Japan (Lot # 53496).

Clay material

An industrially refined Na-type bentonite, Kunipia F, manufactured by Kunimine Industries Co. Ltd was used as a starting clay material. This bentonite contains more than 99% montmorillonite with small amount of quartz and calcite. The chemical formula of the montmorillonite is as follows (Ito et al. 1993);

$(Ca_{0.068}Na_{0.42}K_{0.008})(Si_{3.91}Al_{0.09})(Al_{1.56}Mg_{0.31}Fe^{3+}{}_{0.09}Fe^{2+}{}_{0.01})\ O_{10}(OH)_2$

Additionally, inclusion of trace amount of impurities is estimated for Kunipia-F as follows (Ochs et al. 1999);

KCl 0.005 wt%, NaCl 0.0712 wt% and $CaSO_4$ 0.6935 wt%

Preparation of starting solid-solution system and experimental procedure

Four different types of solutions were prepared; one distilled water and three different synthesized waters. Nitrogen was bubbled throughout the distilled water during 12 hours under nitrogen atmosphere in a glovebox ($O_2 < 0.1$ ppm) to obtain an oxygen-free system. Regarding the synthesized waters, the solutions were prepared using distilled water by adding different chemical agents such as NaCl (0.3 to 1.1 M), $NaHCO_3$ (0.1 to 0.4 M) and $NaSO_4$ (0.05 to 0.2 M). Nitrogen gas was bubbled through the prepared solution for 24 hours in an atmosphere controlled glovebox ($O_2 < 0.1$ ppm). Bentonite was mixed with iron powder with a bentonite/iron mass ration of 1. The mixture (*i.e.*, bentonite plus iron powder) was added to the solution with a liquid/solid mass ratio of 5 (5 mL/g). The starting solid and solution, forming homogeneous slurry mixtures, were put into the vessel. After that, pH and Eh were measured as initial value of the solution. The vessels were stored in the glovebox for 3,823 days (almost 10 and half years) at room temperature. Figure A1-1 shows the flow of experimental procedure.

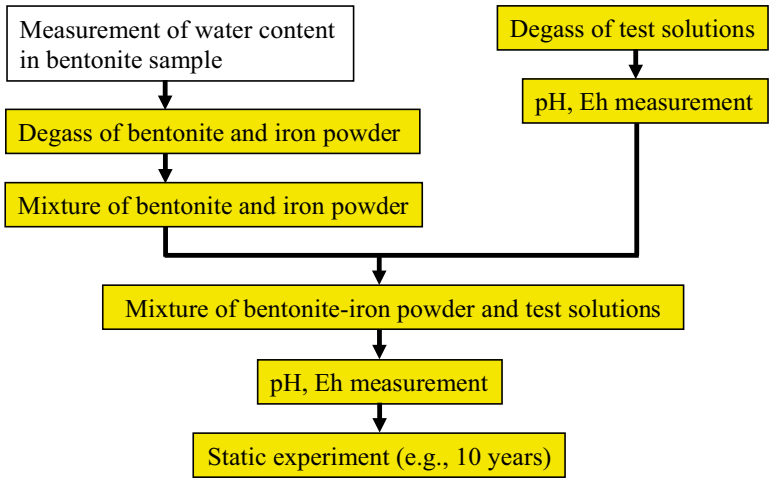

* yellow parts were conducted in controlled-atmosphere globe box.

Figure A1-1. *Schematic flow of experimental procedure.*

The summary of experimental solution, solution volume, mass of iron power and mass of bentonite is shown in Table A1-1. Additionally, the sampling/analysis status (in the middle of April 2009) is also described in Table A1-1. The samples sent to B+Tech are sample #62, 63, 64, 65 and 68 (wet/untreated state), and sample #61 (dry/treated state).

Figure A1-2 shows the flow of measurement and analysis for the samples. After the experiment, the solution pH and Eh were measured and then the sample was centrifuged (12,000 rpm in the Kokusan H-1500F centrifugal machine during 90 min). The separated solution was filtered using membrane filters with 0.45 µm pore size and 10,000 MWCO ultra filters, sequentially. The filtered solution was analyzed using an ICP-AES (Ca, Mg, Al, Si and Fe), Atomic Absorption (Na and K), Ion Chromatography (Cl and SO_4) and an Infrared Photometry (IC) analyzer. For the separated solid, the suspension was dried and the oriented/random samples for X-ray diffraction (XRD) analysis were prepared in the glovebox. XRD analysis was conducted to obtain the qualitative distribution of minerals (XRD analysis was completed only for sample #61, the remaining samples have not been analyzed). The status of other measurement/analysis like CEC, exchangeable cations (Na, K, Ca, Mg), SEM-EDS and TEM-EDS is the same as XRD analysis (*i.e.*, only sample #61 has been completed).

Table A1-1. Summary of experimental set-up and sampling/analysis status.

Sample #	Experimental solution	Solution volume (mL)	Mass of iron powder (g)	Mass of bentonite (g)	Sampling/analysis status
61	Distilled water	250	25	25	Completed
62	Synthesized water #1-1	250	25	25	Analysis: on going
63	Synthesized water #1-2	250	25	25	Analysis: on going
64	Synthesized water #1-3	250	25	25	Analysis: on going
65	Synthesized water #2-1	250	25	25	Analysis: on going
66	Synthesized water #2-2	250	25	25	Not conducted
67	Synthesized water #2-3	250	25	25	Not conducted
68	Synthesized water #3-1	250	25	25	Analysis: on going
69	Synthesized water #3-2	250	25	25	Not conducted
70	Synthesized water #3-3	250	25	25	Not conducted

Note:
synthesized water #1: difference in Cl concentration (#1-1: 0.3 M, #1-2: 0.6 M, #1-3: 1.1 M), *synthesized water#2*: difference in HCO_3 concentration (#2-1: 0.1 M, #2-2: 0.2 M, #2-3: 0.4 M), *synthesized water #3*: difference in SO_4 concentration (#3-1: 0.05 M, #3-2: 0.1 M, #3-3: 0.2 M)

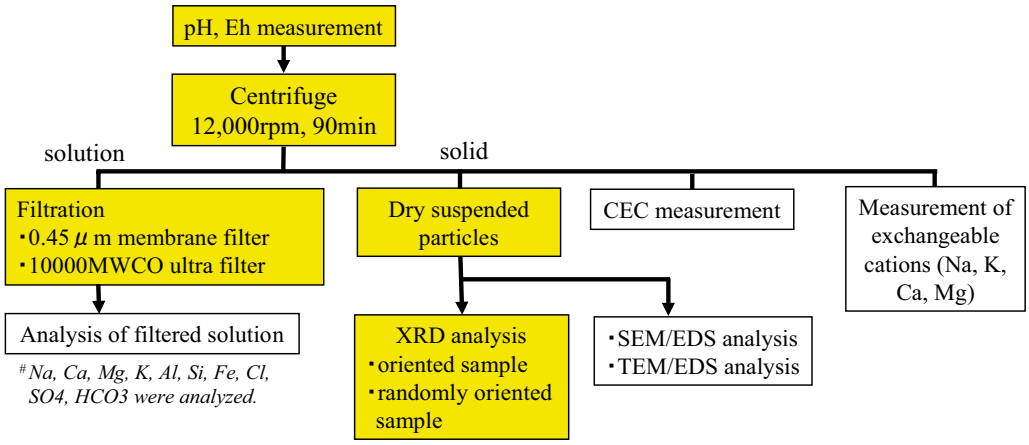

* yellow parts were conducted in controlled-atmosphere globe box.

Figure A1-2. *Schematic flow of measurement and analysis of sample.*

Preliminary results of analysis for sample #61

Opening of sample #61

Sample #61 was opened on the 11th of May 2007. Figure A1-3a shows the photo after opening. The sample color changed to dark-grey. The sample was centrifuged and the two different color parts were observed in the centrifugal vessel (Fig A1-3b). The upper part was greenish and lower part was greyish. Fig A1-3c and d show the dried sample for both the green part and grey part. The lower grey part suggests to be more abundant in iron than the upper part.

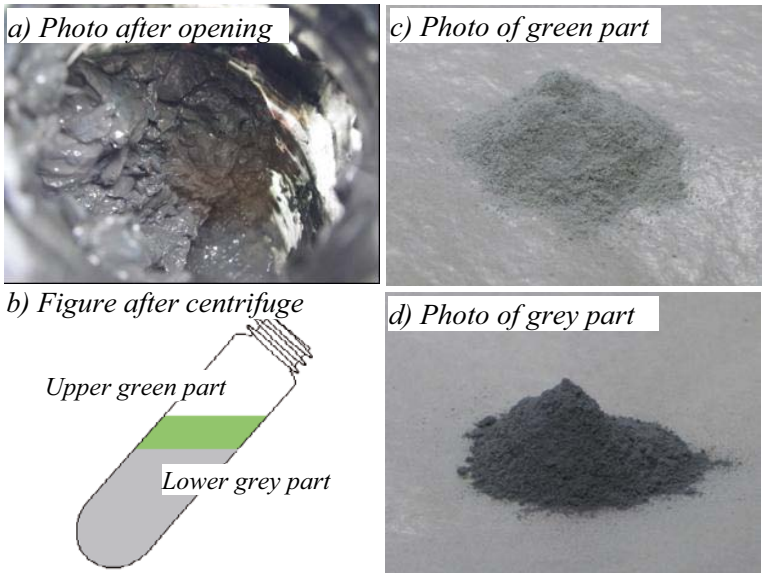

Figure A1-3. *Photos of sample #61 after opening.*

Solution analysis

Table A1-2 shows the solution chemistry before and after experiment. The pH and Eh for initial solution were measured after 10 minutes of mixing distilled water with bentonite (Kunipia F) powder. After the experiment, the solution became more alkaline (pH 11.5) and reducing (Eh –284 mV) compared to the initial solution. Na, Cl and SO_4 increased after the experiment. This increase may be caused by dissolution of soluble impurities like NaCl and Na_2SO_4.

XRD analysis

The XRD data were collected with an RINT-2100 diffractometer (Rigaku Corporation) with Cu-K*a* radiation. Preparation of the oriented sample was carried out in the glovebox and the sample was dried for about 24 hours at room temperature. The prepared sample was set in a special measurement cell in the glovebox to avoid contact with oxygen. Figure A1-4 shows the XRD patters of oriented slides for initial Kunipia F and samples after experiments. From the results no significant changes in XRD patters were observed before and after the experiments.

Table A1-2. Results of pH/Eh measurement and chemical analysis for initial and final solution.

	Initial solution		Final solution	
pH	10.1		11.5	
Eh (mV)	189		-284	
	(mol/L)	(mg/L)	(mol/L)	(mg/L)
Na	D.L	D.L	1.97E-02	453.1
K	D.L	D.L	5.50E-05	2.1
Ca	D.L	D.L	2.11E-05	0.8
Mg	D.L	D.L	D.L	D.L
Fe	D.L	D.L	9.29E-06	0.5
Al	-	-	9.31E-05	2.5
Si	-	-	3.58E-04	10.0
Cl-	D.L	D.L	2.01E-03	71.2
SO_4^{2-}	D.L	D.L	3.60E-03	345.6
HCO_3^-	6.70E-05	4.1	2.89E-04	17.6

D.L: Detection Limit

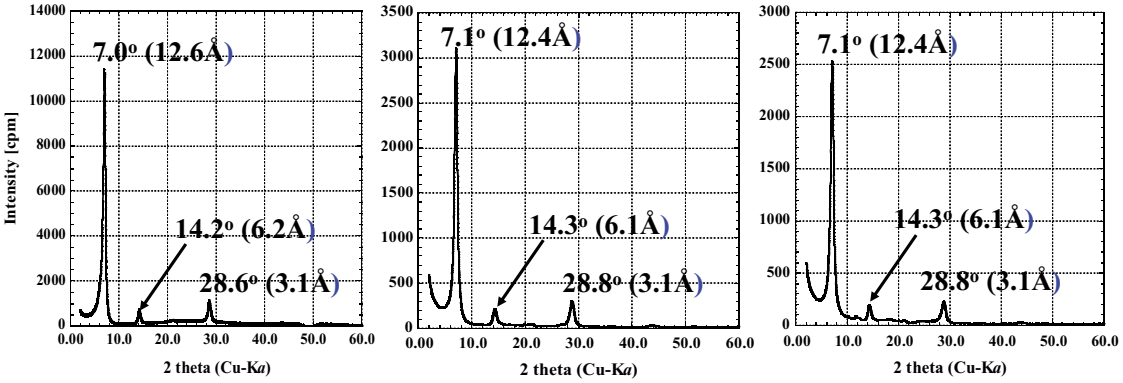

XRD patter of initial Kunipia F

XRD patter of green part

XRD patter of grey part

Figure A1-4. *XRD patterns of oriented slides for initial Kunipia F and samples after experiment.*

SEM observation and EDS analysis

A scanning electron microscope, AKASHI ISI-DS 130 with PHILIPS PV9100 EDS, was used to observe the microscopic morphology of samples after the experiment and to determine the chemical components of the samples. For the preparation of sample for SEM, Au coating on the sample was conducted for preventing charge-buildup. The SEM image and EDS analysis for the samples after experiments (*i.e.*, green part and grey part) are summarized in Figure A1-5. As shown in the figure, the microscopic morphology of the sample surface for both samples was similar and a flake-like structure (typically observed structure for smectite) was observed. Additionally, the results of EDS analysis were also similar except for their iron content. Probably such difference is caused by different amounts of residual iron powder or corrosion products in the sample.

TEM observation

A transmission electron microscope, JEOL JEM-410, was used to determine whether the layer structure typically observed in smectite would be identified or not. Figure A1-6 shows the TEM image of samples before and after experiment. As suggested by the result of XRD, no change was observed in the TEM image.

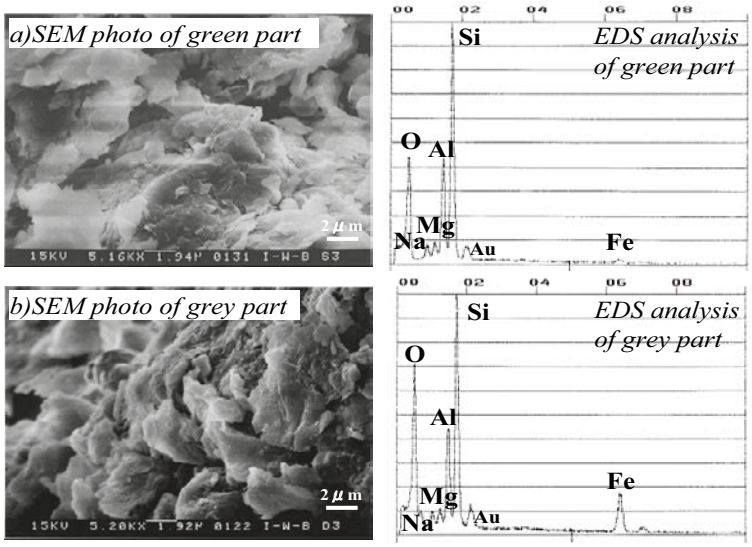

Figure A1-5. *SEM image of samples after experiment.*

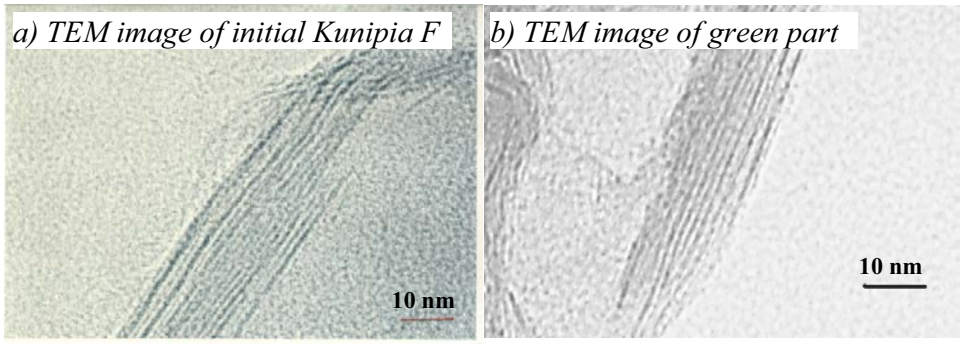

Figure A1-6. *TEM image of samples before and after experiment.*

Summary of preliminary analysis for sample #61

Based on the above results of analysis, the Japanese bentonite (Kunipia F) would not be altered within 10 years contacting with iron powder in the batch experiment using distilled water at room temperature conditions.

Additional results of analysis for sample #62, 63, 64, 65 and 68.

Opening of samples

Sample #62, 63, 64, 65 and 68 were opened on the 2nd of Feb 2009. Figure A1-7 shows the photo after opening except for sample #63. The sample color changed to dark green-black. Regarding to the state of sample, #62 and #64 were liquid-like slurries while #65 and #68 were likely pastes. Such observation may suggest that the amount of residual smectite in #62 and #64 are lower than that in #65 and #68, if we assume that the liquid/solid ratio has remained constant for the experimental duration.

Solution analysis

Table A1-3 shows the results of pH and Eh for solution after the experiments. As shown in the table, the solution was quite alkaline (pH around 13) and reducing (Eh about –600 mV).

XRD analysis

The methods of sample preparation and measurement by XRD are the same as for sample #61 (see section 3.3). Figure A1-8 shows the XRD patterns of randomly oriented slides for the samples #62, 63 and 64 after the experiments. These samples were immersed in the same type of solution (Na-Cl) with different concentrations (*i.e.*, 0.3M for #62, 0.6M for #63 and 1.1M for #64). Comparing with the XRD pattern for the initial sample, the (001) line of smectite reflection decreased in intensity for the samples after the experiment. Concomitantly, the (001) line representative of kaolinite or chlorite appeared at about 7.5Å. The presence of iron powder was identified in all samples and the possibility of the presence of magnetite as corrosion product was also suggested. The peak of halite increased with NaCl concentration in the solution. The position of (006) line of clay minerals was observed at d-values of 1.459–1.498 Å which indicate the presence of dioctahedral clay minerals (*e.g.*, #64).

Table A1-3. Results of pH/Eh measurement.

Sample #	Temp (°C)	pH	Eh (mV, *vs*.SHE)
62	22.9	12.70	-583
63	23.2	12.96	-639
64	23.3	12.80	-637

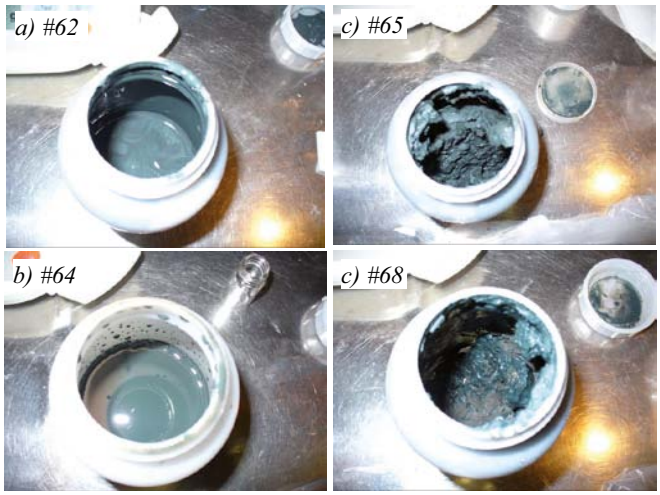

Figure A1-7. *Photos of sample #62, 64, 65 and 68 after opening.*

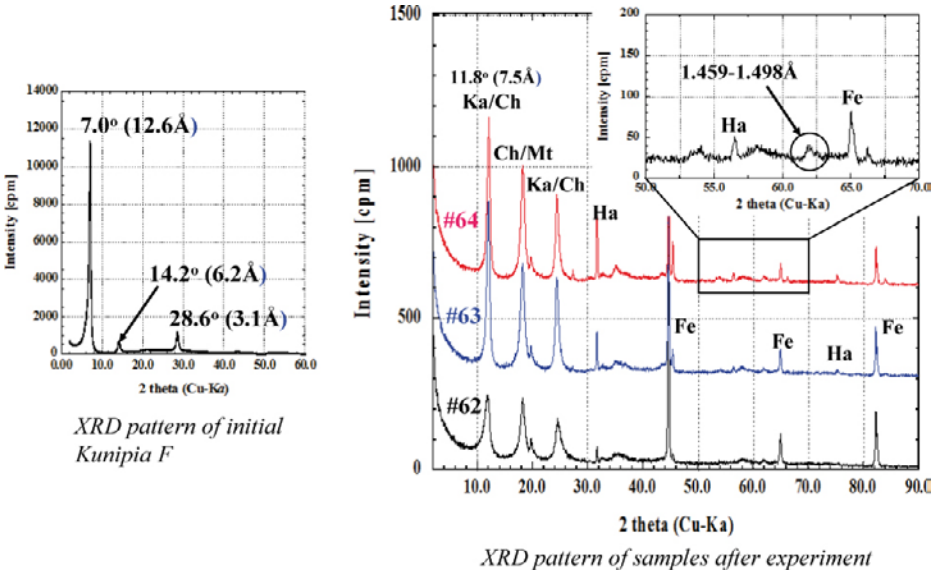

Figure A1-8. *XRD patterns of randomly oriented slides for #62, 63 and 64 after experiment.*

Figure A1-9 and Figure A1-10 show the XRD patterns of randomly oriented slides for the samples #65 and #68, respectively. The immersed solutions were of 0.1M Na-HCO_3 type for #65 and of 0.05M Na-SO_4 type for #68. As the result of comparison, the (001) line of smectite reflection decreased in intensity for samples after the experiment. Additionally, as shown in Figure A1-9, the dominant peaks for #65 were similar to #62, thus the identified minerals were same as for #62. On the other hand, the major peaks for #68 are different with regard to #62 and suggest the presence of halloysite (likely hydrated kaolinite) as reaction product (Figure A1-10).

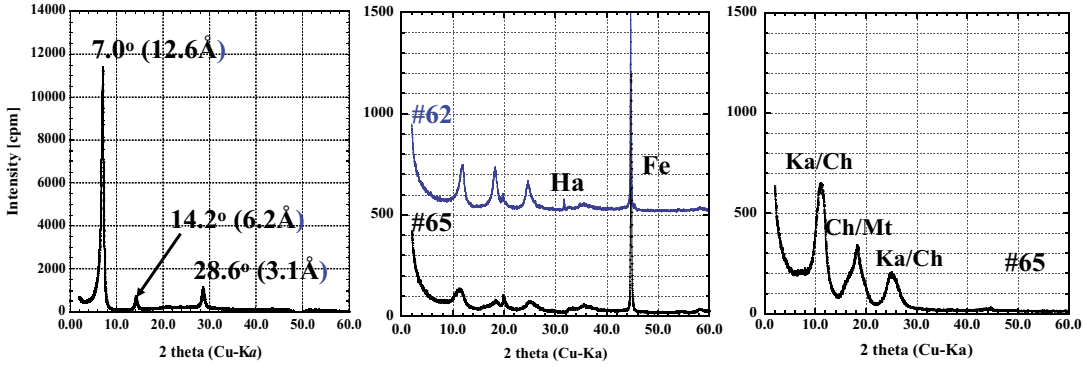

Figure A1-9. *XRD patterns of randomly oriented slides for #65 after experiment.*

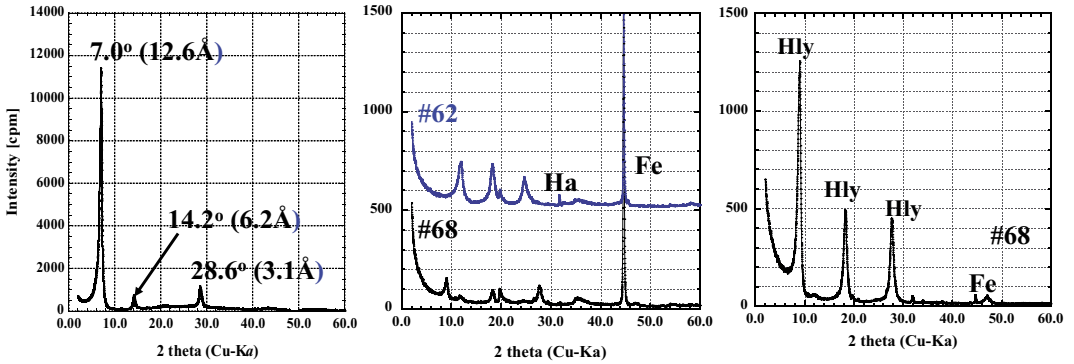

XRD pattern of initial Kunipia F

XRD pattern of samples after experiment (randomly oriented fraction)

XRD pattern of samples after experiment (oriented fraction)

Figure A1-10. *XRD patterns of randomly oriented slides for #68 after the experiment.*

LC, CEC and MB measurements

All samples were mixed with a Fe/clay mass ratio of 1, thus the LC, CEC and MB values of sample before experiment should be basically a half of those of the unreacted clay. Based on this assumption, an ideal CEC value (CEC_{calc}) before the experiment was calculated from the initial CEC value of Kunipia F divided by two. Similarly, the ideal MB value (MB_{calc}) was obtained. Table A1-4 summarizes the results of LC, CEC and MB measurement for sample #61, 62, 65 and 68. As a reference value for the initial sample, the data for Kunipia F are included in the table. Additionally, the results of qualitative evaluation for mineralogical changes by XRD analysis conducted by B+Tech/VTT are added to compare with the results of CEC and MB measurements.

Regarding the CEC values, the extent of reduction decreases in the order of the samples #62>#65>#68>#61 (see Figure A1-11). The CEC values for both #61 and #68 were almost consistent with the CEC_{calc} (considering a general error as 10%), thus the extent of mineralogical change would be small. Such results of measurement are supported by the results of qualitative evaluation by XRD analysis (*i.e.*, no significant change was observed) and MB measurement (*i.e.*, almost consist with MB_{calc}). On the other hand, the decrease of CEC and MB values of #62 and #65 was significant and moderate, respectively. Results of XRD analysis qualitatively support the results of CEC and MB measurements. Therefore, these results of variation can be interpreted by a decrease of smectite in the sample by iron-clay interactions.

Table A1-4. Summary of results of LC, CEC and MB measurement.

Sample No.		61	62	65	68	Kunipia F
Leaching Cations (meq/100g)	Na^+	55.4	75.1	66.8	80.7	114.9
	K^+	1.8	1.0	0.9	1.1	1.1
	Mg^{2+}	2.3	2.5	3.1	1.4	2.6
	Ca^{2+}	11.6	5.7	7.7	9.1	20.3
	Total	71.1	84.3	78.5	92.3	139.2
CEC (meq/100g)		64.8	26.1	37.3	59.1	116.5
CEC_{calc} (meq/100g)		58.3				—
MB (mmol/100g)		—	16	32	76	140
MB_{calc} (mmol/100g)		70				—
XRD Analysis		○	×	△	○	—

Notice: ○ (no change), × (significantly change), △ (partially change)

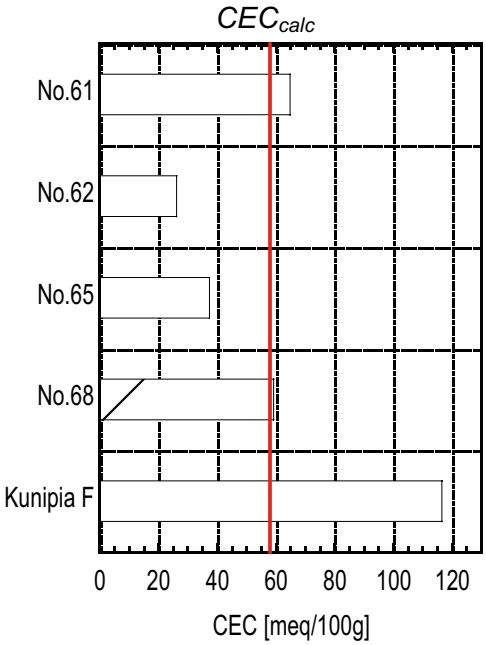

Figure A1-11. *Results of CEC measurement.*

Summary of preliminary analysis for sample#62, 63, 64 and 68

Contrary to the preliminary result of analysis for #61, the (001) line of smectite reflection decreased in all samples. However, the extent of reduction seems to be different among the samples. The degree of reduction of smectite can be evaluated quantitatively by the results of CEC and MB measurements (and XRD analysis by B+Tech/VTT).

Appendix 2

Evaluation and simulation of experimental data from the VTT samples by geochemical modelling

D. Rosch, P. Wersin, Gruner Ltd

1 Introduction

The aim of this report is to evaluate and to simulate the analytical data obtained from the long-term experiment. By means of simple calculations and geochemical modelling the evolution of the external solution was examined in a step-wise manner. Initially, the plausibility and consistency of the experimental results were checked by "back-of-the-envelope" calculations. The main focus then was put on the simulation of the concentrations in the external reservoir by geochemical modelling using PHREEQC. The underlying assumption thereby was that diffusive equilibrium had been attained between the external reservoir and the bentonite porewater after the experimental duration of 8–9 years. These geochemical calculations were carried out first for the data without the iron source. In a second step, the data with the iron source were modelled with the same model assumptions as for the data without the iron source, but including constant iron corrosion kinetics and various assumptions for the precipitating corrosion products.

2 Description of the experiment

In the KBS-3H disposal concept, the bentonite buffer is surrounded by a perforated steel cylinder. The iron will corrode under anaerobic conditions and also interact with bentonite clay. In the long term experiment carried out by VTT and B+Tech, analogous conditions were simulated by contacting a steel source with compacted bentonite, both materials being exposed to a 0.5 molar NaCl solution. Note however, that the iron was placed at the inner side of the bentonite, whereas in the KBS-3H concept the supercontainer shell is located at the outer interface between the buffer and the rock.

The experiment started in late 2000 and lasted 0.75, 8.2 and 8.6 years. The setup consists of a PE vessel with 100 mL 0.5 M NaCl external solution and a gas phase. A copper vessel encloses in the centre an iron cast cylinder surrounded by compacted MX-80 bentonite. On top and on the bottom of the copper cylinder holes and steel sinters ensure that water exchange between the bentonite and the external solution can occur. At emplacement, the bentonite had a moisture content of 7% by weight. Precautions were taken to minimize the amount of oxygen in the system.

In the reference samples, the cast iron cylinder is missing and replaced by bentonite. Overall, 12 samples were prepared and divided in six reference and six Fe-bentonite samples. The samples were stored at room temperature (~25 °C) in a protective steel container, which was kept in a N_2 filled glovebox. At the end of the experiment, different measurements were made on the gas phase, external solution, and bentonite material to obtain information on the interaction of bentonite with the cast iron.

Table A2-1. Parameters of the experimental setup.

Samples	External solution	Dry weight bentonite [g]	Dimensions Bentonite [mm]	Dimensions cast iron [mm]
Reference	100 mL 0.5 M NaCl	30.65	Diameter 24 Height 45	–
Fe-bentonite		27.85		Diameter 14 Height 25

3 Evaluation of basic parameters

Before starting the actual geochemical calculations some plausibility checks were done. These should provide information on the contribution of the salt content in the bentonite to the salinity, the expected sorption capacity and the amount of corroded iron in the experiments. The parameters for the samples analyzed after 8.6 years are given in Table A2-2.

Chloride and main cations:

The expected Cl^- concentration in both the external reservoir and bentonite porewater ("internal" water) was estimated by assuming that part of the "internal" water is bound to the clay edge surface as diffuse double layer (DDL) water using the edge site density given by Wieland et al. (1994). Moreover, it was assumed that the bentonite (with an initial water content of 7 wt %) contained no soluble NaCl impurities. The resulting dilution of the Cl^- concentration for the external water through the initial water content after equilibration is about 0.49 M (Table A2-2). This shows that the dilution effect is small. Furthermore, the maximum capacity for Cl^- in the DDL is very limited (8.7 mmol/L). Also, the effect of soluble NaCl traces in the bentonite (1.35 mmol/kg according to Bradbury and Baeyens 2002) barely affects resulting Cl^- concentrations.

The measured Cl^- concentrations show a rather large variability. Thus, for the reference samples, 0.42 M was measured for the 8.2 year sample, whereas 0.57 M was measured for the 8.6 year sample. The reasons for this spread are unclear.

Table A2-3 shows the amounts of exchangeable cations in the system taking data from Bradbury and Baeyens (2002). This indicates that both CEC and Na concentrations in the exchange complex are in the same range as the NaCl concentration in the external solution.

Table A2-2. Bentonite and solution properties. S/W is the solid-to-water ratio,

	Porosity	Dry density	Saturated density	assumed Lattice density	Dry weight bentonite in experiment	Porewater saturated bentonite	S/W	$[Cl^-]_{t=0}$ external solution	$[Cl^-]_{t=8a}$ external solution
		kg/dm^3	kg/dm^3	kg/dm^3	g	mL	kg/L	mmol/L	mmol/L
Reference	0.47	1.51	2.0	2.75	30.65	9.6	3.08	500.0	488.0
Fe-Bentonite	0.40	1.69	2.1	2.75	27.85	6.6	4.12	500.0	489.0

Table A2-3. Initial ion exchange assemblage for the reference experiment. CEC is from the experiment, the equivalent fractions are from Bradbury and Baeyens (2002), the edge site concentrations from Wieland et al. (1994).

Surface sites	Fraction eq fraction	Sites meq/kg	Sites mmol/30.65g	Sites mmol/L
NaX	0.848	831	25.0	250
CaX_2	0.084	82	1.3	13
MgX_2	0.051	50	0.77	7.7
KX	0.017	17	0.51	5.1
Total CEC	1	980	28.0	280
Edge sites *		28.4	0.87	8.7

* Edge site densities were modified to 10% of CEC in the modelling (see text).

Iron:

The corroded iron is contained primarily in mineral phases and in the exchange complex. The contribution of the dissolved Fe(II) is small, as revealed by the experimental data (1.2E–6 to 7.0E–6 mol/L in the Fe-bentonite). The amount of corroded iron can be estimated from the Fe profile measured by ICP-AES (samples 20a, 20b and 20c; see Table 10). (The semiquantitative analyses estimated from SEM-EDS show a rather high uncertainty and therefore were not used for estimation of corrosion rates). As Fe background, an iron content of 2.52 wt. % was assumed, as measured in reference sample no. 29 b. The measured profile extends over 5 mm from the source, from the centre of the Fe source. All three samples show higher Fe concentrations relative to the reference samples. The total amount of corroded Fe entering the clay is estimated by assuming a uniform distribution of Fe around the metal source and calculating the mass of clay corresponding to each Fe measurement minus the background concentration. This yields a mass of 127 mg or a volume of 0.161 cm^3 of Fe. Taking the surface area of the iron cylinder (14.1 cm^2), a corrosion depth of 0.00115 cm is obtained. With a corrosion time of 8.2 yr, this leads to an average corrosion rate of 1.7 µm/a. Please note that this calculation omits the precipitated corrosion products at the metal surface and thus, the corrosion rate does not represent a conservative estimate.

The ratio of Fe^{2+} to Fe^{3+} was analysed with Mössbauer spectroscopy. For the reference- and the Fe-bentonite sample, the ratio is by 1.024 and 1.543, respectively. For a non treated MX-80 bentonite, Carlson et al. (2007) determined a ratio of 0.565. In general, results suggest that the Fe^{3+} fraction remains constant and that the Fe^{2+} amount is increased in the sample with cast iron. The XANES data also indicate an increase of the Fe(II) component for the samples close to the Fe source. Under the present temperature conditions, the formation of green rust phases (layered Fe(II)/Fe(III)-hydroxides) is possible.

Table A2-4. External solution measurements from the reference- and Fe-bentonite samples after 8.2 and 8.6 years. The saturation indices are calculated with PHREEQC. The pe was only measured for the 8.6 years old samples, for the 8.2 years old samples the same values are used for calculating SI values.

		Ref sample 8.2 years	Ref sample 8.6 years	Fe sample 8.2 years	Fe sample 8.6 years
Solution	pe	–3.56	–3.56	–8.27	–8.27
	pH	8.2	8.0	8.0	8.0
	Alkalinity meq/L	2.3	3.5	4.2	2.9
mmol/L	Na	478.0	544.0	457.0	526.0
	Ca	12.0	13.0	14.0	14.0
	Mg	6.7	7.8	9.8	11.1
	K	2.5	2.2	1.5	1.5
	Fe^{2+}	3.58E–04	3.04E–03*	5.37E–04	4.30E–03
	Fe^{3+}	6.93E–02		7.16E–04	2.69E–03
	Cl	420.0	573.0	480.0	562.0
	HCO_3^-	1.67	2.65	3.20	2.17
	SO_4^{2-}	12.8	12.5	10.1	10.4
Saturation index	Calcite	0.88	0.9	1.02	0.85
	Gypsum	–0.77	–0.82	–0.82	–0.85
	Magnetite	3.31	1.6	11.34	13.4
	Goethite	2.78	2.14	7.37	7.96
	Siderite	–0.4	–0.45	–1.1	–0.37
	$Fe(OH)_3$	–3.12	–3.76	1.48	2.06
	CO_2	–3.31	–2.9	–2.83	–3.0
	O_2	–64.64	–65.44	–84.28	–84.28

* Total Fe

External solution speciation with PHREEQC:

Speciation calculations with PHREEQC were carried out to obtain information on the resulting saturation indices of the external solution. In all the water samples calcite, goethite and magnetite are oversaturated, but slightly undersaturated with regard to siderite. To adjust the model to the experimental conditions the S.I. of calcite was fixed at 0.9. Furthermore, in the reference model the S.I. of siderite was set to –0.4. For the Fe-bentonite model, various cases with different iron corrosion products were tested.

4 Model setup

The computation scheme in PHREEQC was built up in two main steps following the approach presented in Wersin et al. (2004). The first step involves the pre-equilibration of the internal and the external surface sites. This is made with pure water which is in equilibrium with the accessory minerals (calcite, gypsum and quartz, siderite), atmospheric CO_2 pressure and the initial composition of the exchanger- (internal) and surface (external) sites (MX-80 bentonite). The pre-equilibrated solution is used to calculate the internal and external site composition. Cation exchange is calculated by combining Dzombak and Morel's surface complexation model (Dzombak and Morel 1990) and the Donnan approximation of the diffuse double layer (Appelo and Wersin 2007). This yields a more realistic representation of the amount of "bound" water (approximated as DDL water). In the second step, the pre-equilibrated sites are equilibrated with the initial external NaCl solution and the accessory minerals (Table A2-5).

In the Fe-bentonite experiment, the iron corrosion was added through a zero-order kinetic reaction. The estimated corrosion rate from Fe analyses of 1.7 μm/a is taken (see above) which is compatible with literature data (e.g. Smart et al. 2004). The total amount of corroded iron was divided in five equal quantities and added in five equal time steps. The precipitation of different corrosion products (magnetite, $Fe(OH)_2$, green rusts, goethite) was tested in different runs. Dissolution or neoformation of clay phases was assumed not to occur.

In an additional model run, pyrite oxidation was included for the reference experiment. This process is conceivable if at the beginning of the experiment the setup was not O_2 free or if some O_2 infiltrated during the experiment. The possible O_2 content in the bentonite pore space present at the beginning of the experiment reacts with the pyrite. To enable pyrite oxidation the saturation index (S.I.) of pyrite and $Fe(OH)_3$ is set to zero and an adequate amount of O_2 is added.

Thermodynamic database:

The standard PHREEQC database was used, but several iron phases were added: magnetite, $Fe(OH)_2$ (from the ANDRA database Thermochimie) and various green rust phases (from Bourrié et al. 1999).

Table A2-5. Accessory minerals in the MX-80 bentonite in wt%, taken from Müller-Vonmoos and Kahr (1983).

Quartz	Calcite	Gypsum	Pyrite	Siderite
18.1	1.1	0.4	0.5	0.5

5 Comparison between experimental and modelled data

Reference samples:

The inspection of the initial input and final modelled data reveals major changes. From the initial input data to the final modelled data we can see some major changes (Table A2-6). The pH increases from 7.0 to 7.9 and, due to mineral dissolution, the alkalinity rises from 0.0 to 2.5 mmol/L. The sodium concentration is lower in the final solution because of cation exchange reactions: $(Ca, Mg)X_2 + 2Na^+$ à $2NaX + Ca^{2+}/Mg^{2+}$.

Chloride concentration shows no change in concentration (see section above). Calcite and gypsum dissolve, the latter disappears completely. If we include the pyrite oxidation in the model, only minor differences result, such as a slight the pH and pe decrease and a slight alkalinity increase. Test runs indicated that the pH buffering of the clay is somewhat higher than predicted by the model of Wieland et al. (1994). By increasing the amount of edge sites from 3.6% to 10% of CEC a better match of the data with regard to pH and Alk resulted. Therefore, in the modelling data presented below, a modified edge site density of 10% of CEC was considered. It is noteworthy that the model proposed by Bradbury and Baeyens (1997) the edge site density is taken to be 15% of CEC.

The modelled and the experimental data show good agreement except for the Na/Ca ratios at the exchange sites which are predicted to be about a factor of 2.5 higher than was experimentally determined (Table A2-6).

Table A2-6. Comparison of the external solution and the bentonite in the experiment and the model. For the experi-mental solution the saturation indices are calculated with PHREEQC. The pe was only measured for the 8.6 years old samples, for the 8.2 years old samples the same values are used for calculating SI values.

		Ref sample 8.2 years	Ref sample 8.6 years	Ref model	Ref model with pyrite oxidation
Solution	pe	–3.56	–3.56	–3.71	+0.82
	pH	8.2	8.0	7.97	7.94
	Alkalinity mmol/L	2.3	3.5	2.54	2.64
	Ionic strength M	0.501	0.614	0.52	0.53
mmol/L	Na	478.5	543.7	456.6	456.8
	Ca	12.5	13.0	18.4	18.6
	Mg	6.7	7.8	4.1	4.1
	K	2.5	2.2	1.6	1.6
	Fe^{2+}	3.58E–04	3.04E–03*	4.53E–03	4.58E–03
	Fe^{3+}	6.93E–02	–	3.8E–12	1.12E–04
	Cl	419.8	573.0	484.1	484.1
	HCO_3^-	1.67	2.65	1.95	2.03
	SO_4^{2-}	12.8	12.5	8.28	8.69
∆solids	Quartz			–0.01	–0.01
mmol/L	Calcite			–0.25	–0.27
	Gypsum			–0.80	–0.80
	Siderite			–0.0015	+0.014
Saturation index	Calcite	0.88	0.9	0.9	0.9
	Gypsum	–0.77	–0.82	–0.90	–0.75
	Pyrite				
	Magnetite	3.31	1.60	1.67	10.57
	Goethite	2.78	2.14	2.10	6.57
	Siderite	–0.40	–0.45	–0.40	–0.40
	CO_2	–3.31	–2.9	–3.01	–2.97
	O_2	–64.64	–65.44	–66.17	–48.12
Exchanger comp.	Na	72.8		88.3	88.2
% equivalent fraction	Ca	18.5		8.7	8.8
	K	1.3		1.1	1.1
	Mg	7.4		1.9	1.8
	Fe^{2+}	0.01		0.007	0.007

* Total Fe measured

On the other hand, the calculated Ca in solution is slightly higher than measured. This difference can be explained by a slightly higher Ca/Na ratio initial exchanger composition and/or a slightly higher selectivity coefficient for the Na-Ca exchange. In general, the results support the validity of the simple equilibrium modelling approach for simulating solute and exchanger compositions.

Fe-bentonite samples:

For the Fe-bentonite experiment, the same model as for the reference experiment was applied except that in addition a zero-order kinetic corrosion rate of the iron source was included. The estimated corrosion rate of 1.7 μm/a was used for this purpose. For the precipitation of corrosion products accompanying the corrosion reaction, equilibrium conditions were assumed. Various test cases with different corrosion products were run, including magnetite, goethite, $Fe(OH)_2$ and mixed Fe(II)/Fe(III) hydroxides (green rusts), but keeping in mind that, from spectroscopic analysis, the Fe reaction product(s) are enriched in the Fe(II) component.

Table A2-7. Comparison of the external solution and the bentonite in the experiment and the model. For the experimental solution the saturation indices are calculated with PHREEQC. The pe was only measured for the 8.6 years old samples, for the 8.2 years old samples the same values are used for calculating.

		Fe sample 8.2 years	Fe sample 8.6 years	Fe model magnetite eq.	Fe model $Fe(OH)_2$ eq.	Fe model green rust eq.
Solution	pe	–8.27	–8.27	–10.49	–10.43	–8.93
	pH	8.0	8.0	9.49	9.51	7.95
	Alkalinity mmol/L	4.2	2.9	0.50	0.51	3.7
	Ionic strength M	0.527	0.605	0.52	0.52	0.52
mmol/L	Na	456.7	526.3	463.8	464.0	469.3
	Ca	14.4	14.5	14.6	14.7	12.9
	Mg	9.8	11.1	4.0	4.0	4.2
	K	1.5	1.5	1.5	1.5	1.5
	Fe^{2+}	5.4E–04	4.3E–03	4.4E–03	4.4	3.2E–03
	Fe^{3+}	7.2E–04	2.7E–03	7.8E–11	1.0E–10	1.4E–14
	Cl	479.8	561.7	485.1	485.4	484.3
	HCO_3^-	3.20	2.17	0.07	0.07	2.9
	SO_4^{2-}	10.1	10.4	8.4	8.4	8.4
Δsolids	Quartz			–1.6E–02	–1.6E–02	–9.65E–03
mmol/L	Calcite			–6.4E–05	–6.4E–01	–2.22E–01
	Gypsum			–8.0E–01	–8.0E–01	–8.00E–01
	Magnetite			+6.0E–01		
	Siderite				+6.0E–01	–1.42E–01
	$Fe(OH)_2$			+4.3E+00	+4.3E+00	
	$Fe_3(OH)_7$					+1.68E+00
Saturation index	Calcite	1.02	0.85	0.90	0.90	0.9
	Gypsum	–0.82	–0.9	–0.86	–0.86	–0.91
	Magnetite	11.34	13.4	0.0	0.23	–9.27
	Goethite	7.37	8.0	–0.21	–0.11	–3.26
	Siderite	–1.1	–0.4	–0.4	–0.4	–0.4
	$Fe(OH)_3$	1.48	2.1	–6.11	–6.01	–9.15
	$Fe(OH)_2$			–0.04	0.0	–3.22
	$Fe_3(OH)_7$			9.40	9.58	0
	CO_2	–2.83	–3.00	–5.96	–6.00	–2.78
	O_2	–84.28	–84.28	–87.19	–86.97	–86.67
Exchanger assemb. % eq.	Na	72.1		90.1	90.0	90.9
	Ca	16.6		7.0	7.0	6.1
	K	1.1		1.1	1.1	1.1
	Mg	9.3		2.2	2.2	1.9
	Fe^{2+}	0.77		7.3E–5	7.2E–5	0.005

Three different calculation cases are presented in Table A2-7. For all cases, equilibrium with a siderite phase (SI –0.4) was taken, assuming that this phase was present in the original material, as indicated from the modelling analysis of the reference samples (see above). In the first case, magnetite was assumed to form as corrosion product. The resulting simulation shows rather good agreement with the observed data in terms of Fe concentrations, but too high pH and too low alkalinity and Eh values are predicted. Very similar results were obtained for the second case where $Fe(OH)_2$ is assumed to precipitate as corrosion product. On the other hand, the assumption of the mixed 2Fe(II)Fe(III)) $(OH)_7$ green rust phase leads to a good fit, both regard to Fe concentrations and pH, Alk and Eh.

Various runs with different iron corrosion products were performed to test the sensitivity of the assumptions. If siderite equilibrium was omitted, better fits with regard to pH and Alk were obtained for magnetite or goethite as assumed corrosion products. However, the resulting Fe concentrations were much higher and Eh values lower than measured data.

In conclusion, the measured data for Fe samples could be well reproduced with the same equilibrium model as applied for the reference samples and adding zero-order corrosion rate of 1.7 μm/a. According to the modelling outcome, a green rust phase with a Fe(II)/Fe(III) ratio of » 2 gives the best fit of the data. Such a phase is in line with spectroscopic data which indicate the predominance of a Fe(II) phase in the clay at the contact with the metal source.

6 Conclusions

- The experimental data show a rather large spread for Na and Cl between the 8.2 and 8.6 year samples, which is a priori difficult to explain. A further feature is the significant and consistently noted oversaturation with regard to calcite. This oversaturation needed to be included in the model.
- The bentonite model including cation exchange and surface complexation reactions and dissolution of accessory minerals (Wieland et al. 1994, Curti and Wersin 2002), adapted to account for the DDL model concept for compacted clay (Appelo and Wersin 2007) properly simulates solute and exchanger concentrations in the long-term experiments. The results display a slight difference with regard to the Na/Ca ratio of the exchange complex, which may be due to a different initial exchanger composition or to a different exchange constant than used in the model.
- The experimental data of the reference samples can be explained without pyrite oxidation by molecular oxygen. This is in line with experimental effort to minimize the ingress of O_2. The measured Fe concentrations in the reference samples indicate slight undersaturation with regard to siderite, a feature also noted for clay stems such as Opalinus Clay or the Callovo-Oxfordian (Gaucher et al. 2009).
- The results reveal the strong pH buffering capacity of the clay counteracting the increase in pH from the corrosion reaction.
- The estimated corrosion rate from SEM analysis of Fe of 1.7 μm/a agrees with reported corrosion data for long-term anaerobic corrosion, but it should be noted that this value does not include (the unknown amount of) corrosion products formed at the metal surface. The corrosion process could be best simulated assuming the precipitation of a green rust phase with a Fe(II)/Fe(III) ratio of 2.